

# Spatiotemporal Instabilities in Discontinuous Shear Thickening Fluids

Submitted by  
**Peter Angerman**



Submitted to Swansea University in fulfillment of the requirements  
for the degree of  
Doctor of Philosophy

Swansea University  
October 2024

Copyright: the author, Peter Angerman, 2025

Distributed under the terms of a Creative Commons Attribution 4.0 License (CC BY 4.0)

## Abstract

The aim of this work is to study instabilities and the formation of corollary patterns in order to gain a deeper understanding of the underlying physical phenomena and the conditions that lead to the chaotic behaviour of discontinuous shear thickening (DST) fluids. This work consists of two major sections, computational and experimental. In the computational sections, we focus on the problem of rheochaos and aim to develop a minimal microstructural model required to reproduce aperiodic oscillatory behaviour in simple shear. We begin by presenting the first microstructural implementation of DST in Smoothed Particle Hydrodynamics (SPH). We demonstrate that locality in microstructure evolution combined with the characteristic rheology of DST materials yields an inherent spatial instability. We introduce a non-local component in microstructure evolution to obtain formation of frictional structures with a well-defined length scale. Analysis of competition between local and non-local components allowed us to identify spatial configuration as a key feature required to obtain aperiodic solutions. By tuning the parameter space to closely resemble realistic DST materials, we are able to reproduce rheochaotic oscillations closely resembling those reported in the literature, driven by transient cycles of emergence and dissipation in localised frictional structures. Application to realistic flow geometries reveals excellent performance, with our model being able to capture the problem of flow curve construction, the effects of confinement and inertia, and instabilities in Poiseuille flow. Our experimental work focuses on free surface flows. We report a new 'ridge' flow instability in the inclined plane arrangement and identify the significant negative values of  $N_2$  as the driving mechanism. By employing a combination of trough and inclined plane measurements, we demonstrate that the inclined plane is a plausible tool for measurement of  $N_2$  in regimes where conventional methods are not readily applicable.

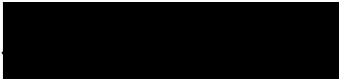


# Acknowledgements

I would like to thank Bjornar Sandnes for his role as my main supervisor, Marco Ellero for his supervision of my computational work, and Dan Curtis for his supervision of my work related to rheometry. In addition, I would like to thank Ryohei Seto for frequent discussions, comments, and feedback.

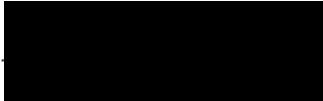
## Declarations

This work has not previously been accepted in substance for any degree and is not being concurrently submitted in candidature for any degree.

Signed..........


Date.....28/09/2024.....

This thesis is the result of my own investigations, except where otherwise stated. Other sources are acknowledged by footnotes giving explicit references. A bibliography is appended.

Signed..........

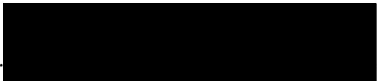
Date.....28/09/2024.....

I hereby give consent for my thesis, if accepted, to be available for electronic sharing

Signed..........

Date.....28/09/2024.....

The University's ethical procedures have been followed and, where appropriate, that ethical approval has been granted.

Signed..........

Date.....28/09/2024.....

# List of Papers

P. Angerman, S.S. Prasanna Kumar, R. Seto, B. Sandnes, and M. Ellero.

Microstructural Smoothed Particle Hydrodynamic Model and Simulations of Discontinuous Shear-Thickening Fluids.

*Physics of Fluids* 1 March 2024; 36 (3): 033103.

Reproduced in Chapter 2.

P. Angerman, B. Sandnes, R. Seto, and M. Ellero.

Numerical Simulations of Spatiotemporal Instabilities in Discontinuous Shear Thickening Fluids.

In Preperation.

Reproduced in Part in Chapter 3.

Z. Xiong, P. Angerman, M. Ellero, B. Sandnes, and R. Seto.

Ridge instability in dense suspensions caused by the second normal stress difference.

*Physics of Fluids* 1 February 2024; 36 (2): 024111.

Reproduced in Part in Chapter 6.

# Contents

Title Page	i
Abstract	i
Acknowledgements	i
Declaration	ii
List of Papers	iii
<b>1 Introduction</b>	<b>2</b>
1.1 Motivation . . . . .	2
1.1.1 Discontinuous Shear Thickening Fluids . . . . .	2
1.1.2 Pattern formation, Non-linear Dynamics and Chaos	3
1.2 Fluid Dynamics . . . . .	4
1.2.1 Continuum Hypothesis . . . . .	4
1.2.2 Equations of Motion . . . . .	5
1.2.3 Rheology of Suspensions . . . . .	7
1.2.4 Discontinuous Shear Thickening . . . . .	12

1.2.5	Microstructure . . . . .	15
1.2.6	Dilatancy . . . . .	16
1.2.7	Kapitza Instability . . . . .	16
1.3	Experimental and Computational Methods . . . . .	17
1.3.1	Rheology . . . . .	17
1.3.2	Smoothed Particle Hydrodynamics . . . . .	18
1.3.3	Nonlinear Dynamics . . . . .	22
1.4	Conclusion . . . . .	27

## 2 Microstructural Smoothed Particle Hydrodynamics Model and Simulations of Discontinuous Shear-Thickening Fluids 29

2.1	Introduction . . . . .	29
2.2	Governing Equations . . . . .	33
2.3	SPH–DST model . . . . .	36
2.3.1	SPH equations of motions . . . . .	36
2.3.2	SPH–DST microstructure model . . . . .	36
2.3.3	Solid wall boundary modeling . . . . .	38
2.3.4	Time integrators . . . . .	39
2.3.5	Particle Shifting Technique . . . . .	40
2.4	Numerical Simulations . . . . .	41
2.4.1	Stress-Imposed Shear Flow . . . . .	41
2.4.2	Channel Flow . . . . .	49
2.5	Conclusions . . . . .	54

<b>3</b>	<b>Numerical Simulations of Spatiotemporal Instabilities in Discontinuous Shear Thickening Fluids</b>	<b>56</b>
3.1	Introduction . . . . .	56
3.2	Method . . . . .	59
3.2.1	DST - continuum scalar model . . . . .	59
3.2.2	Numerical Implementation . . . . .	60
3.2.3	Dimensional Analysis . . . . .	61
3.3	Numerical results . . . . .	62
3.3.1	Dominant Non-Locality . . . . .	62
3.3.2	Vanishing Non-locality . . . . .	65
3.3.3	Moderate Non-Locality . . . . .	68
3.3.4	Viscosity Ratio . . . . .	71
3.3.5	Fluid Inertia . . . . .	76
3.4	Conclusion . . . . .	78
<b>4</b>	<b>Instabilities in Complex Flows</b>	<b>80</b>
4.1	Motivation . . . . .	80
4.2	Simple Shear . . . . .	80
4.3	Poiseuille Flow . . . . .	89
4.4	Conclusion . . . . .	93
<b>5</b>	<b>Material Characterisation</b>	<b>95</b>
5.1	Ageing . . . . .	95
5.1.1	Sedimentation . . . . .	96
5.1.2	Pore Intrusion . . . . .	97

5.1.3	Evaporation . . . . .	98
5.1.4	Swelling . . . . .	98
5.1.5	Ageing in Glycerol . . . . .	98
5.2	Rheology . . . . .	101
5.2.1	Slip . . . . .	101
5.2.2	Inertia: Experimental Design . . . . .	102
5.2.3	Flow Curves, Oscillations and Inertia . . . . .	103
5.3	Conclusion . . . . .	107
<b>6</b>	<b>Instabilities in Free Surface Flows</b>	<b>109</b>
6.1	Introduction . . . . .	109
6.2	Experimental Setup: Tilting Table . . . . .	110
6.3	Tilting Table Experiment . . . . .	111
6.4	Free Surface Pattern Formation . . . . .	113
6.5	Ridge Instabilities: Theory . . . . .	120
6.6	Experimental Setup: Trough . . . . .	124
6.7	Image Analysis . . . . .	129
6.8	$N_2$ Calculation . . . . .	132
6.9	Ridges and $N_2$ . . . . .	133
6.10	Conclusion . . . . .	139
<b>7</b>	<b>Conclusion</b>	<b>142</b>
7.1	SPH, Flow Curves, and Rheochaos . . . . .	142
7.2	Free Surface Flows . . . . .	144

<b>A</b>	<b>Numerical Simulations of Spatiotemporal Instabilities and Pattern Formation: Further Results</b>	<b>147</b>
A.1	Fluid Inertia . . . . .	147
<b>B</b>	<b>Stress Splitting Diagram</b>	<b>157</b>



# Chapter 1

## Introduction

### 1.1 Motivation

#### 1.1.1 Discontinuous Shear Thickening Fluids

The subject of this study is a class of extremely shear thickening materials called discontinuous shear thickening fluids. The most commonly encountered example of this material is corn starch mixed with water, and the most popular application of DST materials currently lies in fun activities for children, outreach programmes, and popular science entertainment media. Indeed, handling these fluids is enjoyable for all ages, perhaps because their apparent behaviour implicitly challenges our conventional understanding of how a liquid should behave. Although we all interface with non-Newtonian fluids on a daily basis, none of them produce a dramatic effect as DST fluids. Seeing a liquid with the consistency of milk turn into a brittle solid and then back into liquid in your palm for the first time is a surreal experience.

Beyond the outlined applications, DST fluids are a subject of intense research with potential applications in the design of impact-resistant batteries [1; 2], tunable property applications in robotics [3] and 3D printing [3], understanding tissue morphogenesis in embryo development [4], and the development of highly adaptable body armour [5]. However, currently, this common kitchen powder resists even the

most basic rheological characterisation [6]. In fact, DST fluids are perhaps the most well known for their complex instability patterns, such as the roll waves reported by Balmforth et al. [7] or the rheochaos found in simple shear by Hermes et al. [8].

### 1.1.2 Pattern formation, Non-linear Dynamics and Chaos

Non-linear, chaotic systems and the patterns they produce are ever present in our lives (one author even simply lists "life" as the final frontier of non-linear dynamics [9]). Examples include immunogenic tumour formation [10], wave patterns in the Zhabotinsky-Zaikin reaction [11] (see Fig.1.1), the way fireflies communicate [12; 13; 14], respiratory process of bacteria [15], cell division [16], the dynamics of epidemics [17], our sleep patterns [18], chaotic flows in drops [19], aperiodic patterns in autocatalytic reactions [20], insect population outbreaks and their relationship to the environment [21], and cardiac arrhythmia [22]. In short, the examples are simply endless. The other side of the coin is that nonlinear systems are often very difficult or impossible to solve. Yet, to some extent, the difficulty is a matter of perspective. Strogatz [9] gives an example of this in context of Poincare's contribution to the three-body problem, and the realisation that the pertinent question is not a quantitative one (the exact position of all three bodies at all times) but a qualitative one (will the bodies eventually collide? fly apart?). An appropriate analogy is that of weather forecasts and climate predictions; predicting weather in the near future at a specific time at a specific location is very difficult [23], but predicting global trends in climate decades into the future is possible. Furthermore, there is a degree of order, even in chaotic systems. Feigenbaum [24] demonstrated that all maps with specific properties transition from stability to chaos identically and was able to measure two fundamental constants associated with these transitions. Nonlinear instabilities, whether periodic or chaotic, contain a wealth of information about the underlying mechanisms. The goal of this work is to use the presence of instabilities to gain insight into the underlying causes and how they relate to the physics of dense discontinuous shear thickening suspensions. Recently, some authors proposed either fairly elaborate models [26] or models that aim to capture microstructural dynamics

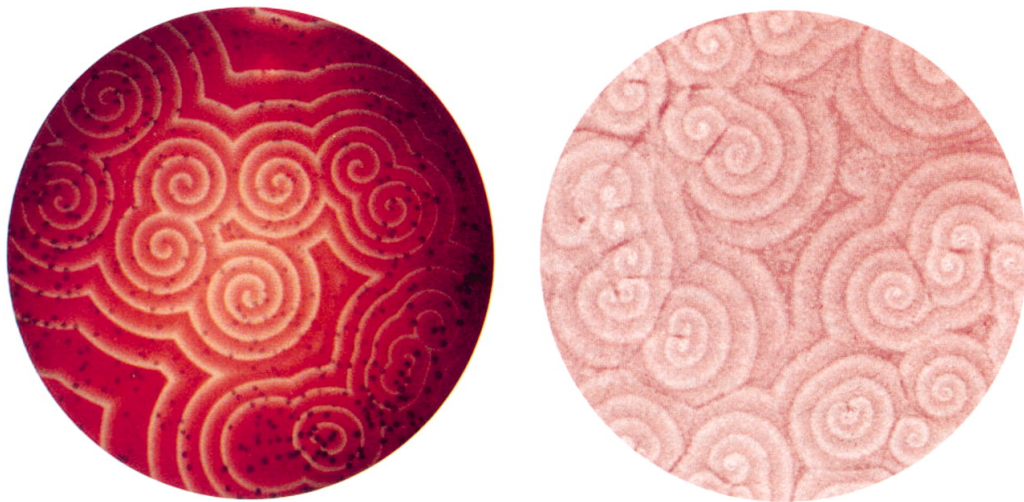


Figure 1.1: Examples of pattern formation in nonlinear systems: Zhabotinsky-Zaikin reaction (left) and slime mold growth (right). Image source: Epstein [25]

from a bottom up coarse graining approach [27] that appear to capture much of the DST behaviours. But the approach in this work is different. We instead ask the question of what is the minimal model is required to reproduce the rich dynamics and pattern formation in DST materials? What model features are essential to capture the nonlinear dynamics as observed in the real systems?

## 1.2 Fluid Dynamics

### 1.2.1 Continuum Hypothesis

Fluids are made up of individual molecules, which experience repulsive and attractive forces. However, on the vast majority of experimental scales, we experience fluids as continuous materials rather than individually moving molecules or particles. A simple way to illustrate the principle of continuum is to imagine a fluid consisting of individual particles, where the fluid density is measured by a mass (or number of particles) within an adjustable measuring volume. If the measurement volume is sufficiently small, the measurement will be highly influenced by the particular

number of included particles, so that the inclusion or exclusion of a single molecule gives rise to a large fluctuation in the measured density. If the measuring volume is now increased, eventually it will encompass a sufficiently large number of fluid particles such that any variations in the measured density are negligible. In the latter example, we can clearly talk about the fluid as a continuum, where physical quantities can be accurately described as occupying a certain small volume of fluid matter, with uniform distribution over the local volume [28].

In short, we assume that the continuum hypothesis holds true for all fluids in this work, so that we need not consider the motion and the forces acting on individual particles. The small complication arises because we aim to study dense suspensions of solid particles within a suspending liquid. It is clear that the continuum hypothesis applies to the solvent liquid, yet the particular interactions between the solid particles have an enormous effect on the properties of the fluid. Furthermore, the solid particles are much larger than the fluid molecules discussed previously, with a particle diameter on the order of  $10\text{ }\mu\text{m}$ . Still, being only interested in the continuum properties of the suspension flows, we will later require a bridge between the behaviour of the suspensions at the solid particle scale (micro-scale) and the resulting properties of the material on the flow scale (macro-scale).

### 1.2.2 Equations of Motion

Before we present the relevant equations, we have a choice between Eulerian and Lagrangian frames of reference. In Eulerian specification, flow fields and material properties are defined at a given position and time, where the position is independent of particular elements of the fluid. A simple way to visualise this is to consider the flow of a gas in a column equipped with stationary probes. The properties of the flowing gas (temperature, velocity, etc.) are measured at the set stationary points over time. In the Lagrangian specification, flow fields and material properties are measured over particular elements of fluid that carry the properties. In the example of the column, this would correspond to tracking specific parcels of the gas and measuring the evolution of the flow properties along the path of the specified

element of the fluid. Generally, introductory works on fluid dynamics tend to prefer the Eulerian specification due to its relative ease of use. However, since we intend to use a strictly Lagrangian computational technique in this work, we will adopt the Lagrangian specification for the rest of this work. For later convenience we define the operator  $D/Dt$  acting on a flow field with position  $\mathbf{x}$  at a time  $t$ :

$$\frac{D}{Dt} = \frac{\partial}{\partial t} + \mathbf{v} \cdot \nabla, \quad (1.1)$$

where  $\mathbf{v}$  is the velocity of the fluid. This allows us to express evolution properties, such as acceleration or transport of a scalar quantity, in a Lagrangian frame by accounting for the convection.

We begin by considering the conservation of mass [29]. Suppose that we have a differential volume  $dV$ , which at any point in time contains a  $\int \rho dV$  mass of fluid, where  $\rho(\mathbf{x}, t)$  is the fluid density. The amount of mass that flows across the surface of the volume ( $dA$ ) per unit time is  $\int \rho \mathbf{v} \cdot \mathbf{n} dA$ . Since the total mass is conserved we can write that the rate of accumulation is equal to the flux of mass

$$\frac{d}{dt} \int \rho dV = - \int \rho \mathbf{v} \cdot \mathbf{n} dA, \quad (1.2)$$

which after transformation from surface to volume integral, can be written in the Eulerian frame as

$$\frac{\partial \rho}{\partial t} + \nabla \cdot (\rho \mathbf{v}) = 0 \quad (1.3)$$

By expanding the divergence term we obtain

$$\frac{\partial \rho}{\partial t} + \mathbf{v} \cdot \nabla \rho + \rho \nabla \cdot \mathbf{v} = 0, \quad (1.4)$$

which can be rewritten in the Lagrangian frame by substituting the definition of the material derivative (1.1)

$$\frac{D\rho}{Dt} + \rho \nabla \cdot \mathbf{v} = 0. \quad (1.5)$$

If we assume that the fluid is incompressible (the density does not change with pressure),  $D\rho/Dt = 0$ , we simplify the conservation of mass to

$$\nabla \cdot \mathbf{v} = 0. \quad (1.6)$$

Next, we turn to conservation of momentum, which relates the rate of change in momentum of a fluid volume to the forces acting on the fluid within the volume. This can be expressed through the Cauchy momentum equation [30]

$$\frac{D\mathbf{v}}{Dt} = \frac{1}{\rho} \nabla \cdot \boldsymbol{\sigma} + \mathbf{a}, \quad (1.7)$$

where the acceleration (LHS) of a fluid parcel depends on the resultant forces acting on the particles. The force balance (RHS) consists of two terms: the first represents the surface forces acting on the fluid parcel, which involves the stress tensor  $\boldsymbol{\sigma}$ , and the second represents the acceleration due to the volumetric forces. The volumetric forces are much simpler, since they almost always consist simply of gravity acting on the fluid volume  $\mathbf{a} = \mathbf{g}$ . The surface forces require the definition of a stress tensor where each element represents the stress acting on each plane of the volume in all directions (resulting in 9 elements for a 3D system). For the purpose of this work, it will be sufficient to write

$$\boldsymbol{\sigma} = -p\mathbf{I} + \eta (\nabla \mathbf{v} + \nabla \mathbf{v}^T). \quad (1.8)$$

The first term on the right hand side represents the isotropic pressure ( $p$ ) acting on the fluid, normal to the planes of the volume element (hence the use of the identity tensor  $\mathbf{I}$ ). The second term represents the deviatoric stress induced by the relative motion of the fluid parcels. This motion results in shear between the fluid elements, which involves the internal fluid 'friction' (viscosity  $\eta$ ). From this point, with defined fluid viscosity and density, equations (1.6)-(1.8) can be solved to obtain fluid flow fields for a given geometry and boundary conditions.

### 1.2.3 Rheology of Suspensions

We begin by looking at typical properties of non-Brownian suspensions [31; 32] (i.e particles are large enough to be unaffected by thermal fluctuations), in absence of discontinuous shear thickening effects. To capture the steady state rheology of such

materials, we can talk about three main viscometric functions [33]

$$\eta(\dot{\gamma}, \phi) = \sigma_{xy} / \dot{\gamma}, \quad (1.9)$$

$$N_1(\dot{\gamma}, \phi) = \sigma_{yy} - \sigma_{xx}, \quad (1.10)$$

$$N_2(\dot{\gamma}, \phi) = \sigma_{yy} - \sigma_{zz}. \quad (1.11)$$

The first function is the constitutive equation that relates the rate of fluid deformation ( $\dot{\gamma}$ ) to the shear stress experienced by the fluid ( $\sigma_{xy}$ ), through the viscosity of the fluid ( $\eta$ ). Shear viscosity can be thought of as an internal fluid 'friction', or a measure of momentum flux induced by the gradients in the fluid velocity [28]. In practice, viscosity tells us how difficult it is to deform a fluid or how easily a fluid flows, a low-viscosity fluid such as water readily deforms upon contact, while a very high-viscosity fluid might exhibit more resistance to deformation. The other two viscometric functions are the first and second normal stress differences, representing the additional tension or compression along the streamlines or vortex lines depending on the combination and the sign of  $N_1$  and  $N_2$  [34]. These functions are responsible for commonly observed fluid instabilities, such as the presence of  $N_1$  inducing the famous 'rod-climbing' Weissenberg effect [35] or the presence of  $N_2$  producing deflections in free surface flows [36].

Suspensions can be thought of as having three distinct regimes based on the volume concentration ( $\phi$ ) of solid particles : dilute, semi-dilute and dense. In the dilute regime, the first expression based on a freely rotating single particle suspended in a shear flow came from Einstein [37] and posed a linear dependence (Fig. 1.2) on the volume fraction

$$\eta(\phi) = \eta_s \left( 1 + \frac{5}{2} \phi \right) \quad (1.12)$$

where  $\eta$  is the suspension viscosity, and  $\eta_s$  is the viscosity of the suspending fluid. The expression predicts an increase in viscosity as a result of the presence of solid particles. In the dilute regime, this effect can be explained by the deformation of the flow field near the particle. Since the solid particle is rigid (does not deform), it will resist the straining elements of the shear flow, resulting in the distortion of the flow in its proximity [32], inducing an increase in the dissipation of momentum

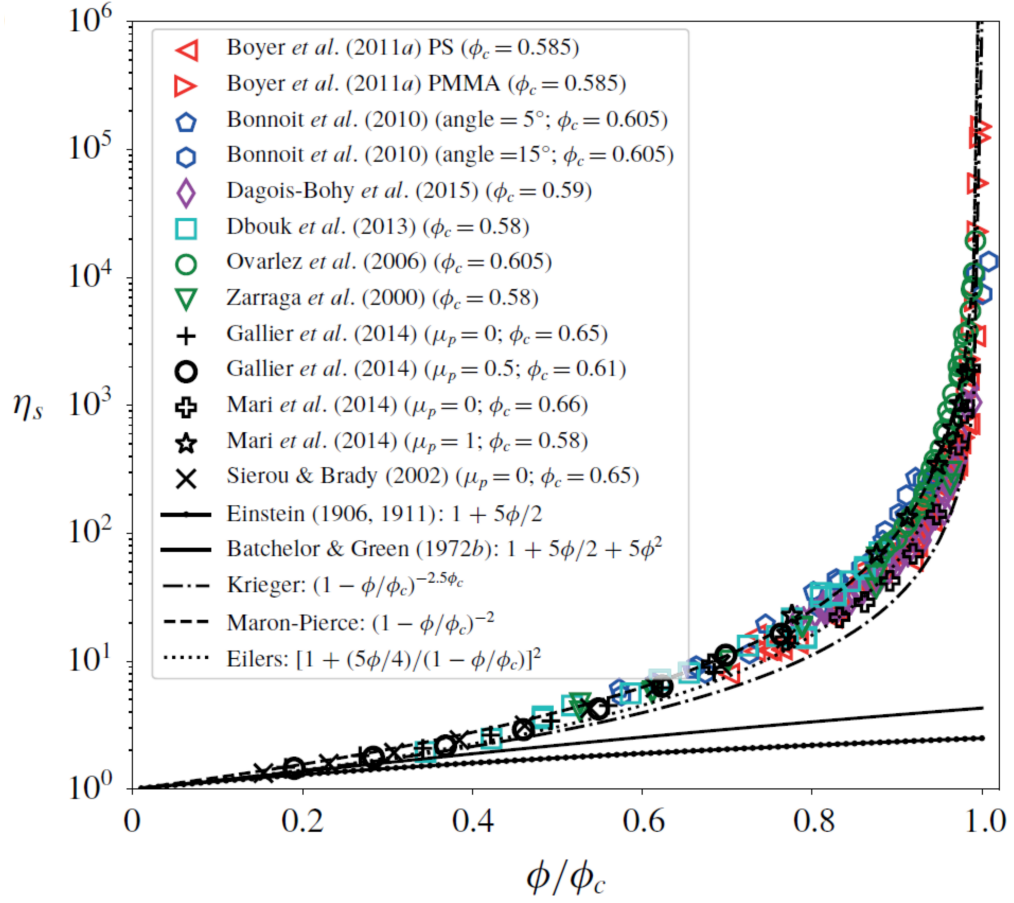


Figure 1.2: Relative viscosity of various suspensions (both simulations and experiments) plotted against normalised volume fraction ( $\phi_c$  is the divergence volume fraction). Image source: Guazzelli and Pouliquen [32]

and thus an increase in shear viscosity. In the semi-dilute regime, the prediction of Einstein [37] underestimates viscosity (Fig.1.2), and a new expression was proposed by Batchelor and Green [38, 39]

$$\eta(\phi) = \eta_s \left( 1 + \frac{5}{2}\phi + 6.95\phi^2 \right), \quad (1.13)$$

which accounts for long-range hydrodynamic interactions between particles due to the deformed flow fields. The expression of Einstein [37] works well up to the volume



fraction of  $\phi = 0.05$  and the expression of Batchelor and Green [38] up to  $\phi = 0.15$ , but both fail to predict the sharp increase in viscosity for dense suspensions. In the dense regime, we no longer need to consider long-range hydrodynamic forces, as frictional contacts between particles begin to dominate dissipative effects [40]. Here, the solutions become difficult to obtain. Instead, we opt to use the phenomenological equation of Maron and Pierce [41]

$$\eta(\phi) = \eta_s \left(1 - \frac{\phi}{\phi_J}\right)^{-2}, \quad (1.14)$$

which matches the trend in viscosity across the full range of volume fraction. Here,  $\phi_J$  is the divergence volume fraction which depends on the friction coefficient of the particles, and is approximately equal to the random close packing  $\phi_{\text{RCP}} = 0.64$  [42] for frictionless spheres.

The first and second normal stress differences in suspension have distinct inception mechanisms, with  $N_1$  mainly a result of hydrodynamic interactions, while  $N_2$  originates from direct contacts [43]. In general, suspensions have a small and negative value (although some works report a positive sign) of  $N_1$  and a large negative value of  $N_2$  [44] (see Fig.1.3). Both functions increase in magnitude with increasing volume fractions, with empirical fits [45]

$$N_1 = -0.8\phi^3\sigma_{xy} \quad (1.15)$$

$$N_2 = -4.4\phi^3\sigma_{xy} \quad (1.16)$$

We can also define normal stress difference coefficients  $\alpha_1$  and  $\alpha_2$ , defined as the ratio of the respective normal stress difference to the shear stress

$$\alpha_1 = N_1/\sigma_{xy} \quad (1.17)$$

$$\alpha_2 = N_2/\sigma_{xy} \quad (1.18)$$

In the absence of additional stress scales or relaxation time (for example, due to interparticle forces), both second coefficient functions, and the viscosity function are observed to be rate independent and only determined by the volume fraction which allows us to write  $\eta(\phi)$ ,  $\alpha_1(\phi)$ , and  $\alpha_2(\phi)$ .

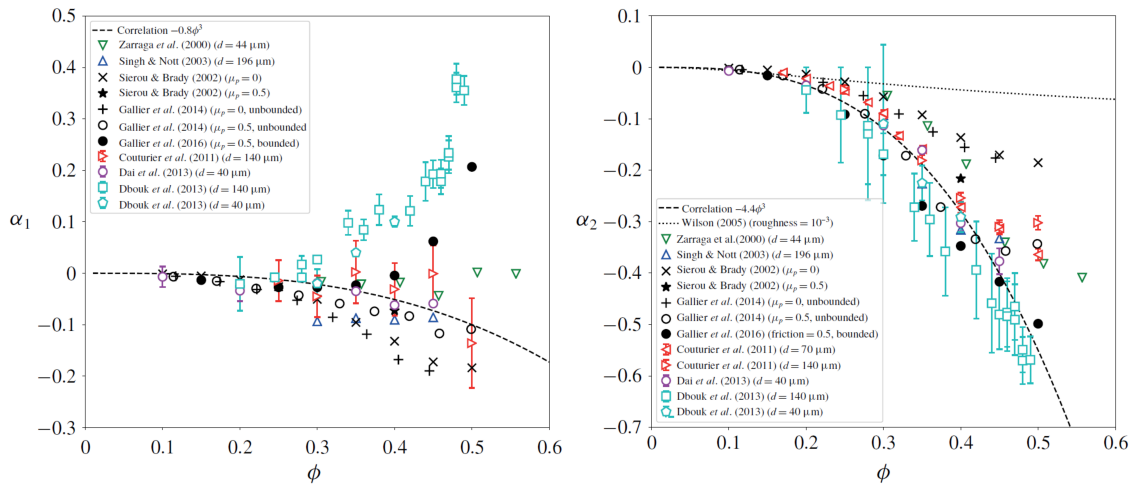


Figure 1.3: Normal stress difference coefficients  $\alpha_1$  (left) and  $\alpha_2$  (right) as a function of volume fraction in experiments and simulations of suspensions. Image source: Guazzelli and Pouliquen [32]

### 1.2.4 Discontinuous Shear Thickening

Some suspensions show a much different response in viscosity during shear. In these materials, applications of shear (or stress) result in a nearly instantaneous and dramatic increase in viscosity once a critical value is reached. Sometimes, the discontinuous jump is preceded or followed by shear thinning effects [46], although these effects are not important for the present discussion. Often, the jump in viscosity spans multiple orders of magnitude, leading to an apparent transition from a liquid state to a solid-like state. The magnitude of the viscosity increase results in a unique feature of DST, where the flow curves have negative shear rate gradients with respect to the shear stress (commonly known as the faster-is-slower effect, also observed in pedestrian dynamics [47]). This class of non-Brownian suspensions is commonly known as Discontinuous Shear Thickening (DST) fluids [48; 49].

The origins of this dramatic rate dependence in viscosity have been the subject of recent interest in the suspension community, with explanations including dilatancy [49] and hydroclusters [50] being proposed. Currently, most authors adopt the reasoning of the Wyart-Cates (WC) [51] model (the name is commonly used in the literature, but the principles behind the model are not exclusive to the work of Wyart and Cates [51]; other authors around the same period of time proposed a similar mechanism [52]). The model proposed that particles in DST suspensions have repulsive interparticle forces, either due to polymer brushes or electrostatic forces, which introduce a new characteristic stress scale in the system,  $\sigma^*$ . When the particles are subjected to stress below this stress scale, the repulsive force holds the particles apart, limiting direct contact and enforcing a low-friction state (often referred to as a frictionless state). Here, the particles interact through long-range hydrodynamic forces or short-range lubrication forces, resulting in relatively low suspension viscosity. Conversely, when a stress sufficient to overcome the repulsive forces is applied, the particles can be driven into direct contacts, which causes the frictional contact forces to dominate leading to relatively high viscosity. Thus, in the WC conception, the rate dependence in DST fluid arises due to the frictionless to frictional transition, driven by overcoming of inherent inter-particle repulsive forces.

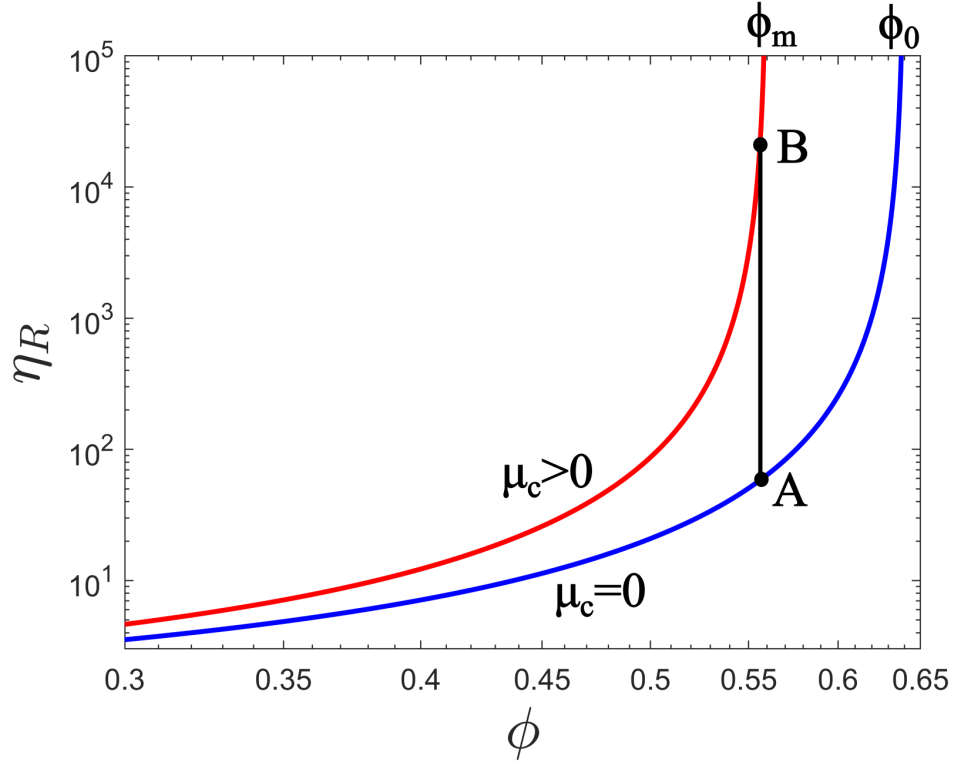


Figure 1.4: Diagram of the Wyart-Cates model. Red and blue lines indicate frictional and frictionless curves diverging at  $\phi_m = 0.56$  and  $\phi_0 = 0.64$ , respectively. Point A represents a suspension with a given volume fraction in absence of any applied stress and thus in the frictionless state ( $f = 0$ ). Upon application of stress, the suspension begins the vertical journey toward point B ( $f = 1$ ) on the frictional curve. As a result the relative viscosity ( $\eta_R$ ) increases by multiple orders of magnitude. Visualising the WC model this way also makes it readily apparent that the jump in viscosity has to increase with increasing volume fraction.

The model (see Fig.1.4) begins by defining a state parameter,  $f$ , which denotes the fraction of particles in frictional contacts at a given local position. The model proposes that  $f$  is some positive monotonic function of shear stress. The exact form of the function is not particularly important, but Wyart and Cates [51] give an

example of

$$f(\sigma_{xy}) = \exp\left(-\left[\frac{\sigma^*}{\sigma_{xy}}\right]\right). \quad (1.19)$$

The divergence volume fraction is then calculated as the interpolation between its frictionless value ( $\phi_0$ ) and the frictional value ( $\phi_m$ )

$$\phi_J(f) = \phi_m f + \phi_0 (1 - f), \quad (1.20)$$

and the viscosity of the suspension is calculated through the Maron-Pierce relation

$$\eta(\phi, f) = \eta_s \left(1 - \frac{\phi}{\phi_J(f)}\right)^{-2}. \quad (1.21)$$

The stress (and thus rate if we write  $\sigma_{xy} = \eta\dot{\gamma}$ ) dependency enters the calculation of suspension viscosity by modifying the divergence volume fraction based on the amount of friction experienced by the suspension, which is determined by the applied stress. Note that the expression for stress is not necessarily a simple one-to-one function; calculation of viscosity requires calculation of stress which in turn requires both viscosity and shear rate to be calculated. It is perhaps not surprising that the WC model produces nonmonotonic multi-valued flow curves. Note that this is a continuum description of the suspensions, which makes the model very convenient for considering large-scale (macro) flow problems. The WC model is a phenomenological description of the mechanism, but it is consistent with recent discrete-particle simulations and  $k$ -core analysis [53] of the microstructure. In their work, Sedes et al. [53], track the formation of frictional networks through the contact number  $Z$  and by using  $k$ -core measure, which tracks clusters of particles where each particle is in the  $k$  number of contacts with other components of the same cluster. One of the key results of their work is that the contact number increases in a one-to-one fashion with stress, a relationship that is reminiscent of the dependence of  $f(\sigma)$  in the Wyart-Cates model. Additionally, the extent of shear thickening (defined as the gradient  $\partial\sigma/\partial\dot{\gamma}$ ) reaches maximum at the onset of  $k = 3$  core formation. Given that there is a close conceptual alignment between the contact number and the fractional of frictional contacts in the Wyart-Cates model, their work demonstrates the consistency between the discrete-particle simulations and the continuum approach of the

Wyart-Cates where DST effects are a result of a transition to a frictional contact state due to the application of increasing stress.

### 1.2.5 Microstructure

. So far, we have discussed the role of contact and friction in DST fluids, but the picture that consists of the frictionless to frictional transition is not complete. When particles enter frictional contacts, they do not do so in a random manner, rather they form a load bearing network through which force can be transmitted over significant distances [54]. The parameter  $f$  in the WC model is an attempt to capture this complex network in a simple continuum parameter. It is widely adopted in the literature because of its ease of use, but it cannot capture some critical features of the underlying structure, such as the fact that the microstructure has a particular orientation [55]. Recently, Gillissen et al. [27, 56] proposed a tensorial description of the continuum structure, but such efforts are still in their infancy.

For the purpose of this work, we will not consider the intricacies of the microstructure orientation or details of the microstructural networks, and instead we will adopt the continuum description consistent with the WC model. A more pertinent question for us is that of microstructural dynamics. More specifically, if the shear thickening is indeed a result of the frictionless to frictional transition, what are the dynamics of such a transition? A typical approach in the literature (which we will follow) is to define a microstructural evolution equation that answers this question [57; 26; 58; 27]. Most evolution equations build on the WC model, and propose that the rate of microstructure evolution is proportional to the difference between the current state and the steady state prescribed by the WC model

$$\frac{df}{dt} = k_f \dot{\gamma} (\hat{f} - f), \quad (1.22)$$

$$\hat{f}(\sigma_{xy}) = \exp\left(-\left[\frac{\sigma^*}{\sigma_{xy}}\right]\right), \quad (1.23)$$

where  $k_f$  is a constant associated with the rate of microstructure evolution. Since the transition requires the particles to come into contact, one can reasonably expect

that such a rate will be proportional to the strain rate, hence the dependence on the shear rate in Eq.(1.22). There are many modifications to the evolution equations; for example Baumgarten and Kamrin [26] includes a "hardening" prefactor ( $H = (\sigma_{xy}/\sigma^*)$ ) and a "softening term" ( $-Sf$ ) which includes features such as network buckling and electrostatic repulsion. Another example is the equation for microstructural evolution of Gillissen et al. [27], which uses the tensorial description to separate the compressive and extensional elements of the strain tensor and the formation and destruction of the base microstructure on the respective components of the shear.

### 1.2.6 Dilatancy

Suspensions can undergo the process of dilatancy. The basic idea is that, when such a fluid is sheared, the motion of particles is restricted by the frictional contacts. Hence, to flow, the particles must take an indirect path that leads to the expansion of the fluid volume (the fluid dilates) [59]. DST fluids often display dilatancy, and this has been proposed as a mechanism of the DST effect, where dilation in the fluid produces geometry-spanning networks of force-transmission chains which act on the confining boundaries. Whether this is the main mechanism behind DST or not, it is present in DST fluids and has been invoked to explain specific behaviours in unstable flows [60].

### 1.2.7 Kapitza Instability

Thin films on Newtonian fluids flowing down an inclined plane have been observed to form surface waves by Kapitza [61]. Benjamin [62] showed that the origin of such waves is inertial and derived following the condition for the onset of instability.

$$Re > Re_k = \frac{5}{6 \tan \theta} \quad (1.24)$$

Where  $Re$  is the depth-averaged Reynolds number,  $Re_k$  is the critical Reynolds number for onset of the Kapitza instability, and  $\theta$  is the angle of inclination. Since then, a multitude of further developments on inertial waves have been proposed, including

accounting for the effects of surface tension [63], 3 dimensional wave patterns [64; 65], and approaches based on energy and momentum integral balances [66].

## 1.3 Experimental and Computational Methods

### 1.3.1 Rheology

Measurements of viscometric functions are most commonly carried out in simple shear, although alternatives such as troughs [36] or rotating rod [34] can be used to measure normal stress differences. Probably the most widely used simple shear setup consists of two parallel plates, with fluid confined by the surfaces. The upper plate is connected to a motor with a rod. In a stress controlled mode, the rheometer applies torque ( $M$ ) on the rod driving the flow of the confined fluid, and measures the angular velocity ( $\Omega$ ) of the plate. From the measured angular velocity, we can calculate translational velocity  $v = \Omega r$ , where  $r$  is the position along the radius of the plate. Since the gap height,  $h$ , is known, we can calculate the shear rate

$$\dot{\gamma} = \frac{r\Omega}{h}. \quad (1.25)$$

The measurement assumes that steady state is reached (the plate is moving at a constant velocity) so we know that the applied torque must be balanced by the shear stress acting on the plate surface, such that shear stress at the rim ( $r = R$ ) is given by

$$\sigma_{xy} = \frac{2M}{\pi R^3}, \quad (1.26)$$

where  $R$  is the plate radius. Both shear rate and the stress can be evaluated at the rim, from which we obtain viscosity  $\eta = \sigma_{xy}/\dot{\gamma}$ . Note that shear rate varies linearly along the radius of the plates, reaching the maximum value at the rim. If we suppose that the fluid is Newtonian, this implies that the shear stress must also have linear scaling with the radial position (since their ratio, viscosity, is constant). This means that both shear rate and shear stress is inhomogeneous in parallel plates along the vorticity direction.



An alternative to parallel plates is cone and plate geometry. Here, the upper plate is replaced with a cone that varies the height of the gap with the radius of the geometry, producing a shear rate independent of the radial position. Unfortunately, such geometry is ill equipped to handle suspensions as a result of issues arising from finite size of solid particles near the centre of the cone. Finally, Couette geometry, consisting of a rotating cylinder in a cup, is another alternative that removes the vorticity stress and shear inhomogeneities and is commonly used, along with parallel plates, in the DST literature. The only practical drawback of the Couette is that it typically requires larger samples. In this work, only parallel plates measurements were used.

### 1.3.2 Smoothed Particle Hydrodynamics

In this work, we will make extensive use of the Smoothed Particle Hydrodynamics (SPH) technique. Fundamentally, SPH is a computational method [67; 68] that can be used to solve the partial differential equations of motion and the accompanying microstructure evolution equation to obtain flow fields for particular problems. It has a rather unique property of being a completely Lagrangian method, meaning that instead of using a grid or a mesh (as is the case in Eulerian methods such as Finite Element (FEM) or Finite Volume (FVM) methods), solutions are obtained at 'particles.' These particles are purely computational constructs that capture an element of fluid and should not be confused with actual solid particles in a suspension. Importantly, the position of these computational nodes is evolved in accordance with the conservation of momentum, with their movement representing the motion of the fluid. This method has a number of advantages and drawbacks. On one hand, it allows for tracking the exact history of a particular fluid element, it seamlessly incorporates free surface flows, and it does not require mesh generation. On the other hand, it has relatively high computational cost, inferior convergence, and challenges with conservation of momentum [69; 70].

The cornerstone of SPH is the kernel function (Fig.1.5)  $W_{ij} = W(\mathbf{x}_i - \mathbf{x}_j)$ , where the subscripts  $i$  and  $j$  refer to a pair of particles. The kernel function is an even,

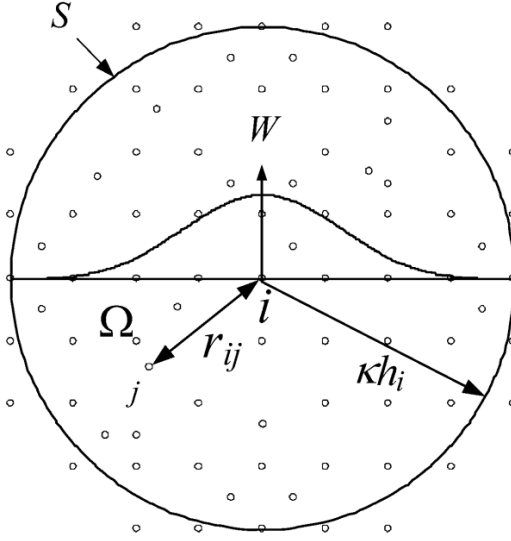


Figure 1.5: Illustration of the kernel function  $W$  in a two dimensional domain  $\Omega$  with boundary  $S$ . Fields in the domain are obtained by summation of overlapping kernel functions. Here  $r_{ij}$  is the distance between two particles, and  $\kappa h_i$  is the cut-off radius for the kernel. Image source: Liu and Liu [71].

monotonic function. An example of a kernel function is the quintic spline

$$W(q) = \begin{cases} a_5 [(3-q)^5 - 6(2-q)^5 + 15(1-q)^5], & \text{if } 0 \leq q \leq 1, \\ a_5 [(3-q)^5 - 6(2-q)^5], & \text{if } 1 < q \leq 2, \\ a_5 [(3-q)^5], & \text{if } 2 \leq q \leq 3, \\ 0, & \text{if } q > 3, \end{cases}$$

where  $q = r/h_{\text{sl}}$  is the distance between the particle pair ( $r$ ) normalised by the smoothing length ( $h_{\text{sl}}$ ), and

$$a_5 = \begin{cases} \frac{1}{120h}, & \text{for dim} = 1, \\ \frac{7}{478\pi h^2}, & \text{for dim} = 2, \\ \frac{1}{120\pi h^3}, & \text{for dim} = 3, \end{cases}$$

Many other forms of the kernel exist, including the Gaussian, cubic spline, and other variations of quintic and other splines [71]. Using the kernel, we can calculate the value of a function at position  $\mathbf{x}$  in a domain  $\Omega$

$$f(\mathbf{x}) \approx \int_{\Omega} (\mathbf{x}') W(\mathbf{x} - \mathbf{x}', h_{\text{sl}}) d\mathbf{x}', \quad (1.27)$$

which can be written in discrete form

$$f(\mathbf{x}_i) = \sum_j^N \frac{m_j}{\rho_j} f(\mathbf{x}_j) W_{ij}. \quad (1.28)$$

Conservation of mass can be ensured either with summation density approach (SDA) or continuity density approach (CDA) [70]. In SDA, density is simply calculated based on the sum of mass carried by proximate particles

$$\rho(\mathbf{x}_i) = \sum_j^N m_j W_{ij}. \quad (1.29)$$

This method provides instantaneous calculation of the density based on the surrounding particles. Alternatively, the density can be calculated by directly solving

the continuity equation (CDA)

$$\left(\frac{d\rho}{dt}\right)_i = \sum_j^N \frac{\rho_i}{\rho_j} m_i (\mathbf{v}_i - \mathbf{v}_j) \cdot \nabla_i W_{ij} \quad (1.30)$$

In the Weakly-Compressible (WC-SPH) formulation of SPH, equation of state is used to relate pressure to density [69]

$$P = \frac{c^2 \rho_0}{\gamma} \left( \left( \frac{\rho}{\rho_0} \right)^\gamma - 1 \right) + P_b, \quad (1.31)$$

where  $c$  is the numerical speed of sound,  $\rho_0$  is the reference density,  $\gamma$  is the polytropic fluid index, and  $P_b$  is the background pressure. Polytropic fluid index implies that the relationship between pressure and density can be expressed in a form of  $P = k\rho^\gamma$ , where  $k$  is a constant. For ideal gases,  $\gamma = 0$ , and for incompressible fluids  $\gamma = \infty$ . In WC-SPH, density is allowed to fluctuate within 1% of the reference value, by tuning the numerical speed of sound  $c \approx 10v_{\max}$ . To avoid negative pressure values, the background pressure is introduced. Typical values of the fluid index for weakly compressible fluids falls around  $\gamma = 7$ .

Gradients of functions, for example velocity  $\mathbf{v}$ , can be estimated

$$\nabla u_i = \sum_j^N \frac{m_j}{\rho_j} (\mathbf{v}_i - \mathbf{v}_j) \otimes \mathbf{L}_i \cdot \nabla_i W_{ij}, \quad (1.32)$$

where

$$\nabla_i W_{ij} = \frac{dW}{dr} \frac{1}{r} (\mathbf{x}_i - \mathbf{x}_j). \quad (1.33)$$

Higher-order derivatives can be obtained in a similar manner. Note that in this definition of the gradient, we include a gradient correction in the form of the tensor  $L$ . This is used to ensure conservation of both linear and angular momentum, which is true for [70]

$$\mathbf{L}_i = \left( \sum_j^N \frac{m_j}{\rho_j} \nabla_i W_{ij} \otimes (\mathbf{x}_j - \mathbf{x}_i) \right)^{-1}. \quad (1.34)$$

From here, the momentum conservation equation can be discretised to give an approximate expression for the acceleration. Discrete forms of continuity and momentum equations are then solved to obtain the desired flow fields. There are many

different formulations here, most commonly that of Morris et al. [72], although alternatives have been proven to have advantages in specific applications, such as free surface flow [73]. Further details on the particular implementation adopted in this work, including formulation of momentum equations, particle shifting technique, boundary conditions, and time stepping will be given in the following chapter.

### 1.3.3 Nonlinear Dynamics

DST fluids are understood to exhibit instabilities in a wide range of flows. In fact, the term 'rheochaos' has been used to describe their behaviour in simple shear. At the same time, the previously laid-out model equations for shear thickening are highly non-linear. Thus, it seems apt to borrow and introduce concepts and nomenclature from the field of study of nonlinear and chaotic dynamics.

Suppose we want to understand the dynamics of a set of equations

$$\dot{\mathbf{x}} = \mathbf{f}(\mathbf{x}). \quad (1.35)$$

Often such non-linear systems are very complex, and even when the solutions are obtained, the particular quantitative detail might be difficult to interpret. Instead, their qualitative properties offer much more insight. A common tool for such analysis is the phase portrait, constructed by plotting the solution to the set of equations in the phase plane  $\Phi_n$ , for a  $n$  dimensional set of equations, where  $\mathbf{x} = (x_1, x_2, \dots, x_n) \in \mathbf{R}^n$ . For example, if we have a two-dimensional system, we can plot our solution in a two-dimensional phase portrait consisting of the axis of  $x_1$  and  $x_2$ . The plot of the solutions in the phase portrait is called a trajectory and represents the transient movement from one state to another. Another distinct feature we can observe in the phase portrait is the presence of fixed points, which represent steady-state solutions  $\mathbf{f}(\mathbf{x}) = \mathbf{0}$ .

Although fixed points represent steady states, they can be further classified into stable and unstable (by 'stable' we generally mean that they are both attracting and Lyapunov stable, and neither for 'unstable') points. A simple way to conceptualise this distinction is to imagine a wheel carefully balanced on a peak of a steep hill, and

the same wheel resting in a valley - both are in steady state, but one will remain the same state with small perturbation, while the other one will rapidly move to another state. The stability of a fixed point can be evaluated by calculating the Jacobian matrix, for example in a two dimensional system

$$J = \begin{pmatrix} \frac{\partial f_1}{\partial x_1} & \frac{\partial f_1}{\partial x_2} \\ \frac{\partial f_2}{\partial x_1} & \frac{\partial f_2}{\partial x_2} \end{pmatrix} \quad (1.36)$$

By evaluating the eigenvalues of the Jacobian at the fixed point, we can understand that point's stability. If the real parts of the eigenvalues are all negative, the point is stable. If at least one real part is positive, the point is unstable. Mixed signs indicate saddle points (stable along a certain axis and unstable along another axis). Consider briefly what stability means for nearby trajectories. If a point is stable, nearby trajectories will approach it, while unstable points will repel the trajectory.

We continue setting the scene by introducing a key concept in stability analysis, which we reproduce from Strogatz [9]

**Definition 1.3.1 (Existence and Uniqueness Theorem)** *"Consider the initial value problem  $\dot{\mathbf{x}} = \mathbf{f}(\mathbf{x})$ ,  $\mathbf{x}(0) = \mathbf{x}_0$ . Suppose that  $\mathbf{f}$  is continuous and that all its partial derivatives  $\partial f_i / \partial x_j$ ,  $i, j = 1, \dots, n$ , are continuous for  $\mathbf{x}$  in some open connected set  $D \subset \mathbf{R}^n$ . Then for  $\mathbf{x}_0 \in D$ , the initial value problem has a solution  $\mathbf{x}(t)$  on some time interval  $(-\tau, \tau)$  about  $t = 0$ , and the solution is unique."*

For our purposes, we simply assume that this is true (see Borrelli and Coleman [74] for proof). In simple terms, this theorem simply states that for a set of equations with continuous smooth gradients, and starting points on the phase portrait, solutions exist and these solutions are unique. The latter statement is the one we focus on next. To say that the solutions are unique means that trajectories in a phase plane can never intersect. Imagine if such an intersection did occur and a new solution was started with the intersection as the initial point. In such a scenario, one set of initial conditions would have two solutions, which violate the uniqueness part of the theorem. Hence, uniqueness imposes another topological constraint on the trajectories - they must now navigate fixed points in accordance with their stability, while avoiding any intersection (Fig.1.7).

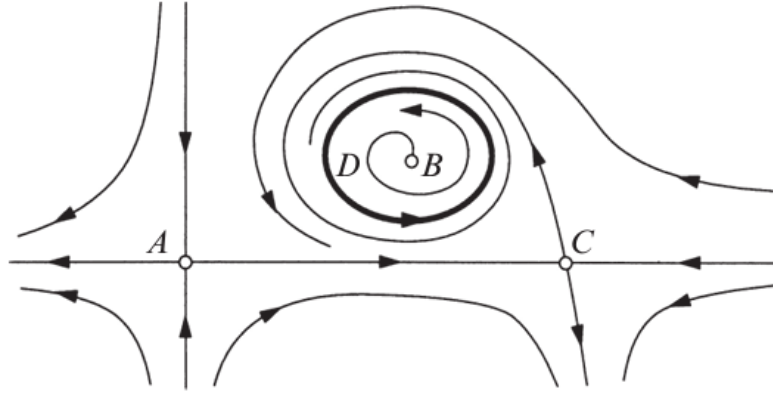


Figure 1.6: An example of common features in phase diagrams. The diagram depicts three unstable fixed points  $A$ ,  $B$ ,  $C$ , and a stable limit cycle  $D$ , which indicates presence of periodic solutions. Image source: Strogatz [9]

From this we can imagine some possible types of dynamics. Suppose that we have a single fixed point in an unconstrained phase space. If the point is unstable, all solutions will spiral outward and 'blow up', and if the point is stable, all solutions will spiral inward into the fixed point (and stay there forever). However, when real DST fluids flow, be it in rheometers or large-scale flows, they do not blow up, so it is more interesting to imagine what would happen if the trajectory was restricted to a certain finite subset of the phase space for  $t \rightarrow \infty$ . If the point is stable, the scenario does not change. On the other hand, if the point is unstable, an interesting conundrum arises: if the trajectory is repelled from the fixed point, but it has to remain in a finite space for infinite time, without ever intersecting itself, where does it go? Can it arrange itself in such a way as to satisfy all the constraints? This question is the exact motivation behind the Poincare-Bendixson theorem [75], which is reproduced again from Strogatz [9].

**Definition 1.3.2 (Poincare-Bendixson Theorem)** "Suppose that

1.  $R$  is a closed, bounded subset of a plane;
2.  $\dot{\mathbf{x}} = \mathbf{f}(\mathbf{x})$  is a continuously differentiable vector field on an open set containing

$R$ ;

3.  $R$  does not contain any fixed points; and
4. *There exists a trajectory  $C$  that is 'confined' in  $R$ , in the sense that it starts in  $R$  and stays in  $R$  for all future time. Then either  $C$  is a closed orbit, or it spirals towards a closed orbit as  $t \rightarrow \infty$ . In either case,  $R$  contains a closed orbit.*

In short, the Poincare-Bendixson theorem answers our question with the conclusion that, under such conditions, the trajectory must form a closed loop, also called a closed orbit or a limit cycle (see Figure 1.7 for a visual explanation). Note that such a closed solution represents an unstable solution, where the signal will forever oscillate in a periodic manner. By simply considering the topological constraints, we can deduce the criterion for instability of DST fluids, provided that we can formulate an appropriate set of dynamical equations which depend on the details of the flow geometry.

The final question is that of 'rheochaos'. So far we have discussed the existence of exactly periodic solutions, where the signal will repeat exactly at regular intervals. Although some signals approaching periodicity have been reported in simple shear, most measurements are strongly aperiodic. We take this opportunity to first define what we mean by chaos. According to Strogatz [9], "*Chaos is aperiodic long-term behavior in a deterministic system that exhibits sensitive dependence on initial conditions.*" We can now once again imagine how such a signal would behave in our previous hypothetical of a bounded subset with no stable points. Since the signal must be aperiodic, it cannot settle into a closed loop, but it must still satisfy the uniqueness part for all time. Thus, we arrive at an apparent contradiction between chaos and the Poincare-Bendixson theorem. The resolution to this tension is that indeed the Poincare-Bendixson theorem is at odds with presence of chaos, and since it is true, it excludes presence of chaos. However, the twist here is that Poincare-Bendixson theorem only applies for two-dimensional phase spaces, and in higher dimension of phase space trapped trajectory can weave in a finite space without ever



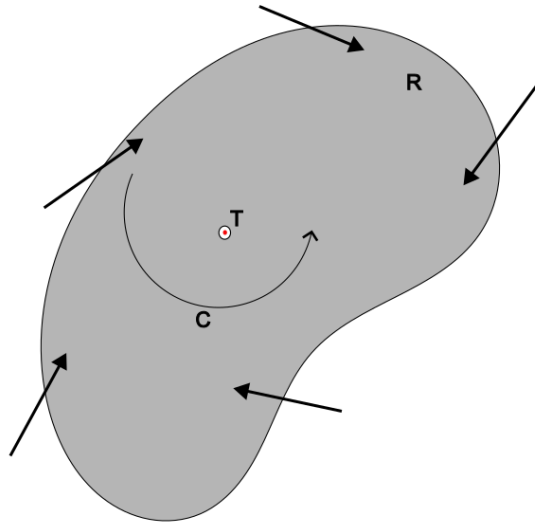


Figure 1.7: An illustration depicting principles of the Poincaré-Bendixson Theorem. A subset  $R$  (shaded) is drawn around a fixed point  $T$  to satisfy 3rd point of the theorem. If a trajectory  $C$  exists in this subset, we can show it is confined (as per the 4th point), if all vectors along the outer and inner boundaries point inwards. This is simple to do around the outer perimeter, as the subset has a finite size (there is no blow up). To show this is true along the inner boundary, the fixed point  $T$  would have to be unstable, so that all the vectors near it point into the trapping region. Thus by careful construction of the trapping region, the existence of limit cycles depends on the stability of the fixed point  $T$ .

intersecting itself for all time. From this we can conclude a critical condition that for chaos to be present, we require at least three dimensions in phase space. This tells us that rheochaotic solutions will originate only from sets of equations with at least three distinct dynamic processes.

Finally, we turn to the practical implementation of DST in terms of stability analysis. We begin with the question of what is the appropriate phase space for DST. Richards et al. [76] carried out analysis in the plane of shear rate and WC model  $f$  parameter, in stress-controlled simple shear flow. This appears to be a natural choice, as  $f$  originates from the dynamics of the evolution of microstructure, and the shear rate originates from the steady state ( $d\dot{\Omega}/dt = 0$ ) based on the balance of the driving torque and the shear stress. In this work, we will present solutions in the space of average shear stress and shear rate, assuming that since  $d\sigma_{xy}/df > 0$  for all values of  $f$ , any stability properties apply equivalently in both planes. Yet, this does not solve the question of chaos. In fact, Richards et al. [76] could only obtain periodic solutions as their phase plane featured only two dimensions. In order to reproduce the phenomena of rheochaos, we will need to find the missing dynamic dimension.

## 1.4 Conclusion

In this chapter we have presented a brief outline of the fundamental physical concepts, relevant experimental and computational methods, and theoretical foundation for understanding non-linear instabilities. The present list is not exhaustive, and is only meant to serve as the baseline for the further chapters. Due to the mixed computational and experimental aspect of this work, we will delve into the fine detail of the techniques used and the relevant literature in the appropriate chapters.

In chapter 2, we present a detailed numerical implementation of DST model in WC-SPH, document unique challenges of purely-local implementation of WC model, and resolve them by introducing non-locality. In chapter 3, we conduct a rigorous dynamic analysis of relevant timescales and length scales in our SPH model, and

demonstrate that inclusion of spatial configuration parameter enables existence of chaotic solutions consistent with the state-of-art experimental literature. In Chapter 4, we apply our rheochaotic model to the problem of simple shear rheology and Poiseuille flow and demonstrate the ability of our model to capture a wide range of particular features of these flows.

In Chapter 5, we turn to experimental work, focused on the issues of ageing, slip, and the effects of inertia and confinement on the stability properties of corn starch. Finally, in Chapter 6, we investigate the stability of free surface flows of DST fluids, with a particular focus on the effects of  $N_2$ .

## Chapter 2

# Microstructural Smoothed Particle Hydrodynamics Model and Simulations of Discontinuous Shear-Thickening Fluids

### 2.1 Introduction

Suspensions of both colloidal [77] and non-colloidal [78; 31] particles are ubiquitous in industrially relevant flows [79], and their rich properties have been subject of extensive study. Some dense suspensions of fine non-Brownian particles can exhibit discontinuous shear thickening (DST) behaviour [80], which has been a subject of great interest in the last decade. With possible implications in industries spanning from manufacturing, environmental engineering, and military application, understanding the underlying mechanism responsible for the unique behaviour has become paramount. Multiple physical explanations have been proposed [49], with the most widely adopted being the mechanism of Seto et al. [81] or Wyart–Cates (WC) model [51], where the particles are held apart in a frictionless state by a characteristic repulsive force. Upon application of external stress, the interparticle

repulsion is overcome, bringing about a transition to a frictional state where the developed contact network inhibits the ease of motion of the suspension. Recently, significant effort has been dedicated to characterising and understanding the effect of the force chain networks in DST [82; 83; 84; 85]. In the work of Sedes et al. [53], the macroscopic microstructure parameter  $f$ , which in the WC model represents the fraction of particles in contact within some averaging fluid element, was shown to be congruent with the microscopic description of contact force networks.

A defining feature of DST, as opposed to continuous shear-thickening (CST), is the characteristic ‘S’ shape of the flow curve. This unique non-monotonic shape facilitates unstable behaviours in rheometric [86; 76] and complex flows. For example, Texier et al. [87; 57] demonstrated that the negative gradients of the flow curve ( $\frac{d\dot{\gamma}}{d\sigma} < 0$ ) present in DST materials cause instability in free surface flows of corn-starch suspension, leading to roll-waves. [57] In the context of simple shear, Cho et al. [88] investigated relaxation dynamics in a parallel-plate setup and proposed a non-trivial two-step mechanism based on a viscoelastic response and force network disintegration, although their system never fully transitioned back to the entirely frictionless state. Rathee et al. [89] employed Boundary Stress Microscopy (BSM) to study stress distribution in rheometric flows. Their results revealed a high degree of heterogeneity in stress fields [90], including two separate high-stress regions in contact with upper and lower plates, respectively, and propagation of high-stress fronts [91].

WC-type models are inherently microstructural — the key parameter governing the state of the suspension at any point is the arrangement of the particle contact network. Typically, works in the context of WC theory propose a relationship between development of the microstructure and macro-hydrodynamic flow properties through a transient evolution equation. Nakanishi et al. [92] employed a scalar model with an assumed S-shape rheology curve in a range of geometries, including simple shear, Poiseuille flow, and free surface inclined plane. The results in simple shear exhibited periodic solutions, accompanied by formation of inhomogeneous fields of the microstructural parameter across the gap. Baumgarten and Kamrin [26] proposed a scalar model based on the balance of strain-dependant hardening and softening

attributed to load buckling, shearing, and electrostatic repulsion. Their model predicted rheological behaviour in good agreement with the experimental evidence.

Another development comes from the work of Gillissen et al. [56], who proposed a full tensorial evolution equation. In addition to predicting DST rheology, they were able to predict negligible first normal stress difference, significant negative second normal stress difference, and flow behaviour in more complicated flow arrangements, including flow reversal and superposed transverse oscillations [27], although the values of normal stress differences predicted by their model were quantitatively too high ( $N_1$ ) and too low ( $N_2$ ) relative to the discrete element method (DEM) values, along with the increases during thickening being underestimated. Their model also did not consider the role of contact friction in the development of microstructure and excluded tangential forces and torque balance.

So far, nearly all continuum microstructural models have been implemented in Eulerian frameworks. In recent times, there has been much interest in simulations of complex fluids with grid-less methods, primarily Smoothed Particle Hydrodynamics (SPH) [69; 93]. SPH was originally developed by Gingold and Monaghan [67] and Lucy [94] in 1977 in the study of astrophysical problems. It is a fully Lagrangian scheme, where the fluid is represented by a set of discrete ‘particles’ carried by flow. Hydrodynamic properties are computed at the position of each ‘particle’ by averaging via a smoothing kernel at each time step, and the trajectories of particles evolve over time. In comparison with Eulerian and mixed Lagrangian–Eulerian methods, SPH has a number of advantages and disadvantages. Generally, grid-based schemes benefit from superior convergence rates and easier implementation of boundary conditions [69]. On the other hand, SPH is inherently mass conservative and handles free surface boundaries and interfacial multiphase flows naturally [68] — which is of importance in a number of studies, including the behaviour of granular bed loads [95], mixing [96], and cavitating flows [97]. Moreover, SPH allows for direct access to the flow history — a crucial feature for microstructural models of complex fluids. This can be leveraged in heterogeneous multi-scale modelling (HMM) [98], with an example application in biologically relevant flows [99], or by directly solving integral constitutive equations [100].

Beyond Newtonian fluids, SPH has been used in a host of fields, including solid and complex fluid mechanics. In 2002, Ellero et al. [101] simulated viscoelastic flow by incorporating the corotational Maxwell model in SPH, followed by Oldroyd-B [102]. Since then, Fang et al. [103; 104] studied the behaviour of free surface flows of an Oldroyd-B fluid, with a focus on addressing tensile instability. Rafiee et al. [105] implemented both Maxwell and Oldroyd-B models in SPH free-surface flows, including impacting drop and jet buckling. Xu et al. [106] simulated three dimensional (3D) injection molding of a Cross-model fluid. Implementation of Oldroyd-B was studied in a periodic array of cylinders by Vázquez-Quesada and Ellero [107] and Grilli et al. [108], and in extrudate swell by Xu and Deng [109].

Furthermore, a range of viscoplastic and elasto-viscoplastic models have been implemented in SPH. Rodriguez-Paz and Bonet [110] simulated debris flow down an incline using the Bingham model and the generalized viscoplastic model. Minatti and Paris [111] considered free surface granular flows, with a constitutive relation based on the works of Pouliquen et al. [112] and Jop et al. [113], and validated their model against granular column collapse experiments. Furthermore, Bingham-like viscoplastic models have been applied to sedimenting flows [114; 115], rheometric flows [116] and mixed fluid-structure cases [117; 118]. Recently, Rossi et al. [119] implemented a modified microstructural Papanastasiou model to study thixoviscoplastic flows around a cylinder. The first application of SPH to DST flow was carried out in the work of Vázquez-Quesada et al. [120], wherein they considered a non-microstructural inverse biviscous model in a simple planar flow.

In this work, we present in detail the first implementation of a scalar non-local microstructural DST rheological model in an SPH scheme. Unlike previous models [120], we obtain typical S-shaped DST rheology in the simple shear and characteristically inflexed velocity profiles accompanied by flow reduction behaviour in channel flow. In both cases, stress-splitting is observed as a result of the local term in the evolution equation acting on a perturbed microstructure field. Section 2.2 lays out the details of the model used in this study. Section 2.3 presents the details of the numerical scheme and boundary condition treatment.

In section 2.4.1, the origin of stress-splitting and the effect of non-locality on

establishing spatial correlations in the structure are discussed in context of simple shear. In section 2.4.2, we derive a solution for planar channel flow for a fluid following the Wyart–Cates model and use it to validate our SPH simulations. Finally, we compare our results to a previous non-microstructural model.

## 2.2 Governing Equations

In this section, we outline the main equations used to model our DST fluid system. The continuum system can be written in the Lagrangian frame:

$$\frac{d\rho}{dt} = -\rho \nabla \cdot \mathbf{v}, \quad (2.1)$$

$$\frac{d\mathbf{v}}{dt} = \frac{1}{\rho} \nabla \cdot \boldsymbol{\sigma} + \mathbf{a}, \quad (2.2)$$

$$\boldsymbol{\sigma} = -p\mathbf{I} + \eta (\nabla \mathbf{v} + \nabla \mathbf{v}^T), \quad (2.3)$$

where  $d/dt \equiv \partial/\partial t + \mathbf{v} \cdot \nabla$  is the material derivative,  $\rho(\mathbf{x}, t)$  is the density field,  $\mathbf{v}(\mathbf{x}, t)$  is the velocity field,  $\boldsymbol{\sigma}(\mathbf{x}, t)$  is the stress field,  $p$  is the pressure, and  $\mathbf{a}$  is the acceleration due to a body force acting on fluid. In this DST model, the local suspension viscosity is determined using the Maron–Pierce expression [41].

$$\eta(\phi, \phi^J, t) = \eta_s \left(1 - \frac{\phi}{\phi^J}\right)^{-2}, \quad (2.4)$$

where  $\eta(\phi, \phi^J, t)$  and  $\eta_s$  are, respectively, the suspension and constant solvent viscosities.  $\phi$  is the particle volume fraction, and  $\phi^J$  is the jamming volume fraction. Assuming particle migration is negligible for the problems studied in the present work, the value of  $\phi$  is kept constant and homogeneous across space. The value of  $\phi^J$  is inferred dynamically as

$$\phi^J(f(\mathbf{x}, t)) = \phi^m f(\mathbf{x}, t) + \phi^0 \{1 - f(\mathbf{x}, t)\}, \quad (2.5)$$

where  $\phi^m$  and  $\phi^0$  are frictional and frictionless divergence volume fractions, respectively.



The discontinuous shear-thickening phenomenon wherein the viscosity of the medium undergoes a sharp transition from a lower to a higher value is modeled with the help of a single microstructure scalar field called the fraction of frictional contacts  $f(\mathbf{x}, t)$ . The use of this scalar field model follows from the Wyart–Cates model [51], in which the value of  $f$  is determined as  $\exp(-\sigma^*/\sigma)$ . The repulsive force between particles,  $F_0$ , sets the characteristic stress scale at the onset of shear-thickening  $\sigma^* = F_0/6\pi a^2$  [121]. Figure 2.1 shows (a) typical flow curves produced by the model and (b) the corresponding viscosity dependence on shear stress. For sufficiently low volume fractions ( $\phi < 0.50$ ), continuous shear-thickening (CST) is achieved. Increasing volume fraction above 0.50 leads to a transition from CST to a DST regime, marked by the appearance of the characteristic S-shape, where stress is a multi-valued function of shear rate. Further increases in volume fraction sharpen the S-curve up to a point of divergence ( $\phi = \phi^m$ ).

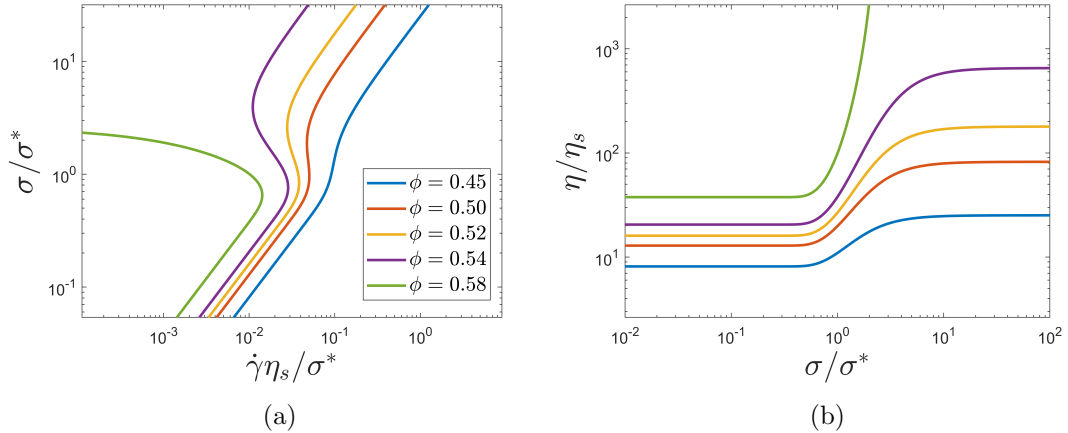


Figure 2.1: WC model of the DST fluids: (a) Flow curves in the stress-shear plane, (b) viscosity dependence on shear stress. Plots for  $\sigma^* = 0.005$ ,  $\phi_m = 0.562$ , and  $\phi_0 = 0.693$ .

The value of  $f(\mathbf{x}, t)$  at a point in the flow field depends on the local value of stress, and the dependency follows a sigmoid function. Time dependence of microstructure is captured in the microstructure evolution equation (2.6), which in the present work

consists of a local and a non-local term. The local term has been widely used in the DST literature [92; 58; 57; 122; 26] and represents approach of the system towards a shear-stress dependent steady-state prescribed by the Wyart–Cates model (2.7) with a characteristic time-scale set by the shear-rate and a microstructural rate constant  $K_f$ . In addition to the usual local term, we introduce a non-local contribution in the dynamics of structure, where the microstructural parameter  $f$  diffuses with a diffusion coefficient  $\alpha$ . In this work, we follow the approach of Kamrin and Henann [123] and include microstructure diffusivity directly in the evolution equation. The non-local feature of our model has the benefit of stabilising the local-driven instability discussed in sec. 2.4.1.

$$\frac{df(\mathbf{x}, t)}{dt} = K_f \dot{\gamma} \left( \hat{f}(\mathbf{x}, t) - f(\mathbf{x}, t) \right) + \alpha \nabla^2 f(\mathbf{x}, t), \quad (2.6)$$

$$\hat{f}(\mathbf{x}, t) = \exp \left( - \left[ \frac{\sigma^*}{\sigma_{xy}(\mathbf{x}, t)} \right]^\beta \right), \quad (2.7)$$

where  $\dot{\gamma}(\mathbf{x}, t) = \sqrt{\dot{\boldsymbol{\gamma}} : \dot{\boldsymbol{\gamma}}/2}$  is the local shear calculated as the second invariant of the strain rate tensor  $\dot{\boldsymbol{\gamma}}(\mathbf{x}, t) = (\nabla \mathbf{v} + \nabla \mathbf{v}^\top)/2$ . The first term on the right-hand side of (2.6) accounts for the local evolution of microstructure, whereas the second term introduces non-local effects via microstructure diffusivity, where  $\alpha$  is the diffusion coefficient.

## 2.3 SPH–DST model

### 2.3.1 SPH equations of motions

The Navier–Stokes equations are solved using the SPH methodology. A possible discretized form of the governing equations is given below [72]:

$$\frac{d\rho_i}{dt} = \sum_j m_j \mathbf{v}_{ij} \cdot \nabla_i W_{ij}, \quad (2.8)$$

$$\begin{aligned} \frac{d\mathbf{v}_i}{dt} = & - \sum_j m_j \frac{p_i + p_j}{\rho_i \rho_j} \nabla_i W_{ij} \\ & + \sum_j \frac{m_j (\eta_i + \eta_j) \mathbf{x}_{ij} \cdot \nabla_i W_{ij}}{\rho_i \rho_j r_{ij}^2} \mathbf{v}_{ij} + \mathbf{g}_i, \end{aligned} \quad (2.9)$$

where  $m_j$  is the mass of a particle,  $W_{ij} = W(|\mathbf{x}_{ij}|)$  is the smoothing kernel,  $\mathbf{v}_{ij} = \mathbf{v}_i - \mathbf{v}_j$ ,  $\mathbf{x}_{ij} = \mathbf{x}_i - \mathbf{x}_j$ , and  $r_{ij} = \sqrt{\mathbf{x}_{ij} \cdot \mathbf{x}_{ij}}$ .

Following the weakly compressible SPH (WCSPH) formulation, a 1 % variation in density is permitted. The fluid pressure is then calculated based on the Tait’s equation of state:

$$p = \frac{\rho_0 c^2}{\gamma} \left[ \left( \frac{\rho}{\rho_0} \right)^\gamma - 1 \right] + p_b, \quad (2.10)$$

where  $\rho_0$  is the density of the fluid,  $p_b$  is the background pressure, and  $c$  is the numerical speed of sound typically set as 10 times the maximum flow velocity  $v_{\max}$ .

### 2.3.2 SPH–DST microstructure model

So far, we have described details of SPH for general flows with Navier–Stokes equations. In this section, we discuss the SPH closure model for the definition of viscosity  $\eta_i(f_i, t)$  in the SPH–DST model. The constitutive equations are written as follows,

where the subscript  $i$  indicates the particle index (that is  $f(\mathbf{x}_i, t) = f_i$ ):

$$\dot{f}_i = K_f \dot{\gamma}_i (\hat{f}_i - f_i) + \alpha \nabla^2 f_i, \quad (2.11)$$

$$\phi_i^J = \phi^m f_i + \phi^0 (1 - f_i), \quad (2.12)$$

$$\eta_i = \eta_s \left( 1 - \frac{\phi_i}{\phi_i^J} \right)^{-2}. \quad (2.13)$$

In (2.11),  $f_i$  is calculated to evaluate  $\phi^J$  in (2.12), which in turn is used to obtain viscosity via (2.13). The value of  $\dot{\gamma}$  in (2.11) is computed as the contraction of the strain rate tensor  $\dot{\gamma}$  as follows:

$$\dot{\gamma} = \frac{1}{2} \sqrt{\dot{\gamma} : \dot{\gamma}}, \quad \dot{\gamma}_{kl} = \frac{1}{2} \left( \frac{\partial u_k}{\partial x_l} + \frac{\partial u_l}{\partial x_k} \right). \quad (2.14)$$

The SPH approximation of the gradient of the  $k$ -component of the velocity vector in  $l$ -direction is obtained as

$$\left( \frac{\partial u^k}{\partial x^l} \right)_i = \sum_j \frac{m_j}{\rho_j} (u_j^k - u_i^k) \nabla_i^l W_{ij}. \quad (2.15)$$

The non-local term in eq. (2.11) is discretised in a manner consistent with the Morris formulation of the moment equation [69],

$$(\nabla^2 f)_{i \in f} = \sum_{j \in f} \frac{2m_j (f_i - f_j) \mathbf{x}_{ij} \cdot \nabla_i W_{ij}}{\rho_j r_{ij}^2}. \quad (2.16)$$

To simulate the ‘S’-curve (see Fig. 2.1) with the above definition of order parameter  $f$ , the choice of  $\phi$  has to be sufficiently close to  $\phi_m$  which in the above case is  $\phi > 0.50$ . However, the value of  $\eta/\eta_s$  for  $\phi = 0.54$  at a high shear rate is approximately 3000, which drastically lowers the time step size required for stable integration of the governing equations. A simple idea used to address this was to modify the definition of  $f$  so that we can anticipate the ‘S’ at a lower volume fraction. Therefore, the modified definition of  $f$  is as follows.

$$\hat{f}_i = \exp\{-(\sigma^*/\sigma_i)^\beta\}, \quad (2.17)$$

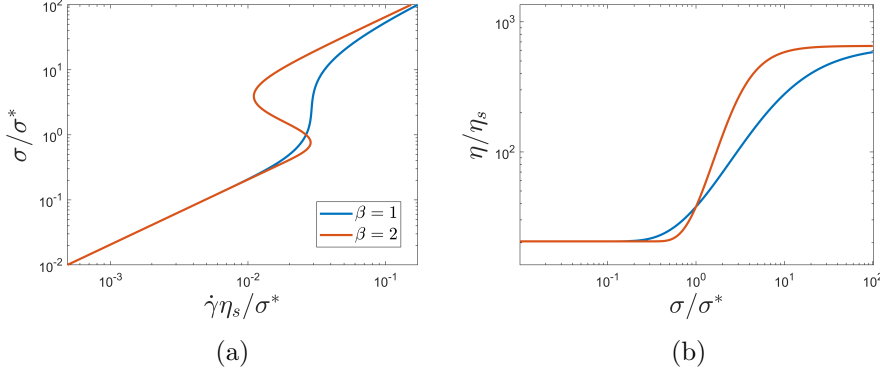


Figure 2.2: Comparison of WC model flow curves, i.e., (a) rate dependence of viscosity and (b) stress dependence of viscosity for  $\beta = 1$  and  $\beta = 2$ . Larger values of  $\beta$  result in stronger shear thickening effect at equivalent volume fractions.

where  $\beta$  is the parameter setting the ‘sharpness’ of the transition between the frictional and frictionless plateaus, without changing the plateau values. We set  $\beta = 2$  in this work. Increasing it allows us to introduce the previously discussed S-shaped rheology to an otherwise CST volume fraction, resulting in DST behaviour without increasing viscosity to computationally prohibitive values. Furthermore, we choose the rest of the parameters, primarily  $\phi^m$  and  $\phi^0$ , such that all simulations lie within the prescribed region of  $10^{-3} < Re < 1$ . The lower bound was chosen to facilitate feasible run time by preventing excessively small time-steps (2.36) due to shear-thickening. The upper bound is used to exclude fluid inertial effects from all cases in this work. Once the values of  $f_i$  and  $\phi^J(f_i)$  are obtained, the dynamic viscosity of a SPH particle is updated using (2.13).

### 2.3.3 Solid wall boundary modeling

The dummy particle method of Adami et al. [124] is employed for imposing no-slip velocity boundary conditions and impermeability conditions. For a full explanation behind this method, we direct the reader to their work. Below we present their method in notation consistent with the present model.

Pressure, density, and velocity are assigned to the dummy particles as

$$p_{i \in w} = \frac{\sum_{j \in f} p_j W_{ij} + (\mathbf{g} - \mathbf{a}_{i \in w}) \cdot \sum_{j \in f} \rho_j \mathbf{x}_{ij} W_{ij}}{\sum_{j \in f} W_{ij}}, \quad (2.18)$$

$$\mathbf{a}_{i \in w} = -\frac{\nabla p_{i \in f}}{\rho_{i \in f}} + \mathbf{g}, \quad (2.19)$$

$$\rho_{i \in w} = \rho_0 \left( \frac{p_{i \in w} - p_b}{p_0} + 1 \right)^{\frac{1}{\gamma}}, \quad (2.20)$$

$$p_0 = \frac{\rho_0 c^2}{\gamma}, \quad (2.21)$$

$$\mathbf{v}_{i \in w} = 2\mathbf{v}_{\text{wall}} - \tilde{\mathbf{v}}_{i \in w}, \quad (2.22)$$

where subscript  $w$  and  $f$  denote the dummy wall and fluid particles, respectively,  $\mathbf{v}_{i \in w}$  is the prescribed wall velocity, and

$$\tilde{\mathbf{v}}_{i \in w} = \frac{\sum_{j \in f} \mathbf{v}_j W_{ij}}{\sum_{j \in f} W_{ij}}. \quad (2.23)$$

### 2.3.4 Time integrators

A semi-implicit predictor-corrector type integration scheme is used for time marching as follows.

(1) Predictor step:

$$\mathbf{v}_i^{n+\frac{1}{2}} = \mathbf{v}_i^n + \frac{\Delta t}{2} \left( \frac{d\mathbf{v}_i}{dt} \right)^n, \quad (2.24)$$

$$\rho_i^{n+\frac{1}{2}} = \rho_i^n + \frac{\Delta t}{2} \left( \frac{d\rho_i}{dt} \right)^n, \quad (2.25)$$

$$\mathbf{x}_i^{n+\frac{1}{2}} = \mathbf{x}_i^n + \frac{\Delta t}{2} (\mathbf{v}_i)^n, \quad (2.26)$$

$$f_i^{n+\frac{1}{2}} = f_i^n + \frac{\Delta t}{2} \left( \frac{df_i}{dt} \right)^n. \quad (2.27)$$

(2) Corrector step:

$$\mathbf{v}_i^{n+\frac{1}{2}} = \mathbf{v}_i^n + \frac{\Delta t}{2} \left( \frac{d\mathbf{v}_i}{dt} \right)^{n+\frac{1}{2}}, \quad (2.28)$$

$$\rho_i^{n+\frac{1}{2}} = \rho_i^n + \frac{\Delta t}{2} \left( \frac{d\rho_i}{dt} \right)^{n+\frac{1}{2}}, \quad (2.29)$$

$$\mathbf{x}_i^{n+\frac{1}{2}} = \mathbf{x}_i^n + \frac{\Delta t}{2} (\mathbf{v}_i)^{n+\frac{1}{2}}, \quad (2.30)$$

$$f_i^{n+\frac{1}{2}} = f_i^n + \frac{\Delta t}{2} \left( \frac{df_i}{dt} \right)^{n+\frac{1}{2}}. \quad (2.31)$$

The flow variables at the subsequent time step are obtained as follows:

$$\mathbf{v}_i^{n+1} = 2\mathbf{v}_i^{n+\frac{1}{2}} - \mathbf{v}_i^n, \quad (2.32)$$

$$\rho_i^{n+1} = 2\rho_i^{n+\frac{1}{2}} - \rho_i^n, \quad (2.33)$$

$$\mathbf{x}_i^{n+1} = 2\mathbf{x}_i^{n+\frac{1}{2}} - \mathbf{x}_i^n, \quad (2.34)$$

$$f_i^{n+1} = 2f_i^{n+\frac{1}{2}} - f_i^n, \quad (2.35)$$

where  $n$  represents the current time instant,  $n + \frac{1}{2}$  represents the predicted time instant (variables at an intermediate time level), and  $n + 1$  represents the corrected time instant. This scheme is second-order accurate in time. Finally, the time-step size  $\Delta t$  is determined based on the following condition

$$\Delta t = \min \left\{ 0.25 \frac{h_{\text{sl}}}{c}, 0.125 \frac{h_{\text{sl}}^2}{\nu}, 0.25 \left( \frac{h_{\text{sl}}}{|\mathbf{g}|} \right)^{1/2} \right\}, \quad (2.36)$$

where  $h_{\text{sl}}$  is the smoothing length, and  $\nu$  is the kinematic viscosity. The adaptive time-step approach ensures that the CFL condition [125] is satisfied, along with additional constraints due to the viscous diffusion and particle acceleration [72]. Due to the extreme shear-thickening nature of the material studied in the present work, viscous diffusion is likely to be the most restrictive condition.

### 2.3.5 Particle Shifting Technique

Following the work of Lind et al. [126], we introduce shifting of particle position to disallow SPH particles from following the streamlines of the flow, which might lead

to anisotropic particle distribution under certain conditions. Lind et al. [69] points out that the accuracy of SPH approximations diminishes with irregular particle distribution. The shifting of particle position is completely *numerical* in origin and not physical. Therefore, we keep the shifting to a minimal level by setting the condition that maximum particle shifting  $\boldsymbol{x}_{i,\text{shift}}^{\text{max}} < 0.1h_{\text{sl}}$ , where  $h_{\text{sl}}$  is the smoothing length (approx. equal to the average inter-particle spacing).

The particles are shifted based on a shifting velocity  $\boldsymbol{v}_{i,s}$  which depends on the local particle concentration gradient vector  $\nabla C_i$ .

$$\boldsymbol{v}_{i,s} = D_i \nabla C_i \quad (2.37)$$

Here,  $D_i$  is the shifting velocity coefficient. The normalised particle concentration  $C_i$  at a given particle location is computed as

$$C_i = \sum_j V_j W_{ij} \quad (2.38)$$

where  $V$  is the volume of the particles. The gradient of the particle concentration is then calculated as,

$$\nabla C_i = \sum_j \left\{ 1 + \frac{1}{4} \left( \frac{W_{ij}}{W_{ii}} \right)^4 \right\} V_j \nabla W_{ij}, \quad (2.39)$$

For more details on the treatment of free surface boundary conditions in SPH, the reader is referred to the work of Lind et al. [126].

## 2.4 Numerical Simulations

### 2.4.1 Stress-Imposed Shear Flow

The behaviour of the previously introduced DST model is explored by simulating the rheology in a simple shear geometry. The fluid is bound between two solid walls vertically (gap height  $h = 0.01$ ) and two periodic boundaries horizontally at a distance  $l = 0.01$  m. The domain is planar with no depth in the vorticity direction.



Table 2.1: Simulation Parameters

$h$ [m]	$l$ [m]	$\rho$ [kg m <sup>-3</sup> ]	$\eta_s$ [Pa s]	$\phi$	$\phi^m$	$\phi^0$	$\sigma^*$ [Pa]
0.01	0.01	1000	0.001	0.48/0.50/0.54	0.562	0.693	0.005

Unlike previous shear-imposed simulations [127], input stress  $\sigma_{\text{in}}$  is set here on the upper wall by assigning wall particles an appropriate velocity.

To impose specified stress on the top wall of the Couette geometry, the following approach is used. The wall particles are assigned with velocity ( $v_{i \in w}$ ) computed from the wall force ( $F_{\text{diff}}$ ), which is in turn determined from a predictor–corrector method.

$$v_{i \in w}^{n+1} = v_{i \in w}^n + k_p F_{\text{diff}} \Delta t. \quad (2.40)$$

The net wall force ( $F_{\text{diff}}$ ) is computed as the difference between the applied wall force ( $F_{\text{in}}$ ) and the resistive shear force ( $F_r$ ) exerted by the fluid on the top wall

$$F_{\text{diff}} = F_{\text{in}} - F_r, \quad (2.41)$$

$$F_r = \sum_{j \in w} F_j, \quad (2.42)$$

$$F_{i \in w} = \sum_{j \in f} F_{ij}^\nu, \quad (2.43)$$

where subscripts  $w$  and  $f$  denote wall and fluid particles, respectively.  $F_{ij}^\nu$  is the inter-particle viscous force in eq. (2.9). All simulations use a quintic kernel, and smoothing length  $h_{\text{sl}} = 1.1\Delta x$ , where  $\Delta x = 0.02l$  is the initial spatial resolution. Simulations are carried out for the same material parameters (see table 2.1) with different imposed stress values. Three microstructure diffusion coefficients are tested to probe the effects of the non-local term — strong non-locality ( $\alpha = 10^{-5} \text{ m}^2 \text{ s}^{-1}$ ), moderate non-locality ( $\alpha = 10^{-8} \text{ m}^2 \text{ s}^{-1}$ ), and zero non-locality ( $\alpha = 0 \text{ m}^2 \text{ s}^{-1}$ ). In addition, three values of volume fraction were simulated for the case of strong non-locality: CST ( $\phi = 0.48$ ), moderate DST ( $\phi = 0.50$ ), and strong DST ( $\phi = 0.54$ ). Steady-state values are used to construct the flow curve (Fig. 2.4). All rheometric values are obtained by averaging over the entire domain and across time, after allowing

the system to reach steady state for at least 100 s. A convergence study was carried out in the context of purely local channel flow (sec. 2.4.2), where the obtained SPH velocity profiles were compared to the theoretical solution. Significant improvements in the solution accuracy were seen up to the resolution of  $50 \times 50$  particles, beyond which only marginal improvements were observed. Hence, in both sections resolution of  $50 \times 50$  is employed. Both walls were constructed with 200 dummy particles each. Simulations were run for up to 72 hours of computing time and 10 minutes of simulation time.

Far below onset stress the behaviour is essentially Newtonian — all three measured properties (shear stress, shear rate, and microstructural parameter  $f$ ) approach their respective steady-state values asymptotically and within relatively short timescales. Once the stress is increased, the time required to achieve a steady state is significantly increased, and over/under-shoots are present prior to achieving a steady state. This is likely due to the formation of microstructure being relatively slow compared to purely inertial transient effects — in the initial stages, the lack of structure allows shear rate to peak above the steady-state value. This overshoot then accelerates formation of microstructure, increasing viscosity, which in turn adjusts the shear rate (or undershoots). To mitigate this behaviour, we choose to initialise all simulations from a pre-defined homogeneous field  $f$  corresponding to the correct prediction of the WC at a given input stress, along with the appropriate shear rate via the upper wall velocity. For all values of  $\alpha$ , simulation results (Fig. 2.4(a)–(c)) on stable branches are in excellent agreement with the theoretical model predictions.

In the case of strong non-locality, the simulation results for all three volume fractions (Fig. 2.3) match the WC model very well across the entire flow curve, including the region of negative gradient for the DST volume fractions. Both the stress and microstructure fields are entirely homogeneous Fig. 2.4(d) and (g) due to the strong non-local term, with minor deviations in the computed shear rate field, likely due to the imprecision associated with numerical approximations and low resolution.

In the purely local ( $\alpha = 0$ ) case, for all imposed stresses falling within the unstable region of negative flow curve gradient, seemingly spurious ‘jumps’ in microstructure, local stress and viscosity were observed, where individual particles attain either much

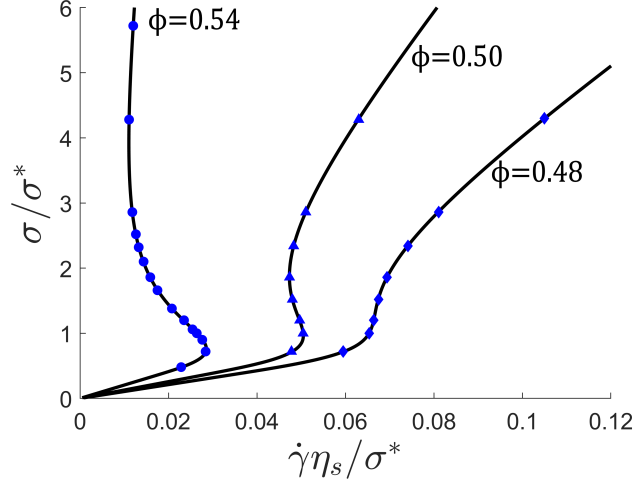


Figure 2.3: Results for three volume fractions: 0.54 (circles), 0.50 (triangles), and 0.48 (diamonds). Strong non-locality ( $\alpha = 10^{-5}$ ). Simulation results (blue symbols) compared against the analytical solution of the WC model (black lines).

higher or lower stress and microstructural parameter with respect to the imposed stress. This behaviour had no impact on the numerical stability of the simulations, and a solution could be computed even in this extreme case. These jumps occurred with no clear spatial correlation, yet both the domain averaged properties and the properties measured at the wall remained in close agreement with the correct theoretically predicted values. By plotting all individual SPH particles for a given applied stress over the expected flow diagram (Fig. 2.4(f)), it is apparent that these jumps are directed towards the valid stable solutions of the WC model.

In principle, a DST fluid could undergo vorticity banding under stress-controlled regime, which, in the simplest case, would manifest as any stress applied within the unstable branch (the branch joining frictional and frictionless branches) being split vertically into two bands organised along the vorticity direction each with either higher or lower stress, but the same shear rate (as opposed to gradient banding, where two bands of equal stress but different shear rates would be expected). The width of the bands is then decided by a lever rule, such that the total average stress is equal

to the applied stress. Such phenomena in DST materials have been experimentally observed in the work of Herle et al. [86], who reported formation of clear bands along the vorticity direction. The onset of vorticity banding is accompanied by large oscillations in shear rate, and the bands themselves were reported to oscillate along the vorticity position. This behaviour is consistent with the theoretical argument of Hermes et al. [8], who excludes the possibility of steady-state vorticity bands in non-Brownian suspensions on the account of particle migration and normal stresses. For a purely local model and a constant volume fraction field, no effects counteract such splitting, giving rise to a new steady state configuration, where all individual SPH particles occupy stable branches of the flow curve ( $\frac{df_i}{dt} = 0$ ), while being split such that the stress control equation is also satisfied ( $\frac{dv_{\text{wall}}}{dt} = 0$ ).

The lack of spatial correlation in structure (Fig. 2.4(i)) is caused by the action of the microstructure evolution equation on the numerical noise introduced in the SPH solution. Suppose all particles are initialised exactly at the steady state solution, with small perturbations in a random direction in the rate-stress plane. The particles that find themselves to the right of the flow curve will experience  $\frac{df_i}{dt} > 0$ , leading to an increase in local viscosity. This will, in turn, increase the local shear stress, increasing the value of  $\hat{f}_i$ , ensuring that the particle will continue to move upwards until it reaches a stable upper branch where  $\frac{df_i}{dt} = 0$ . An identical argument applies to the particles to the left of the curve, with the resultant downward movement instead. In the case of our simulations, the small perturbations are introduced by the inherent numerical noise associated with meshless calculation of the local shear rate  $\dot{\gamma}_i$  via eq. (2.14). These small imprecisions do not have a spatial correlation, hence after stress-splitting amplification we arrive at discontinuous spatial distribution of microstructural parameter. The low-high stress split of particles should approach an even split; however, the flow curve is not symmetric about the horizontal imposed stress line, and such split would result in an increase of measured shear stress. This means that as the stress-splitting takes place, particles are simultaneously rearranged between the lower and upper branches via the stress-control mechanism of eqs. (2.40)–(2.43) to achieve correct average stress.

To further explore both the microstructural transients and steady states, new

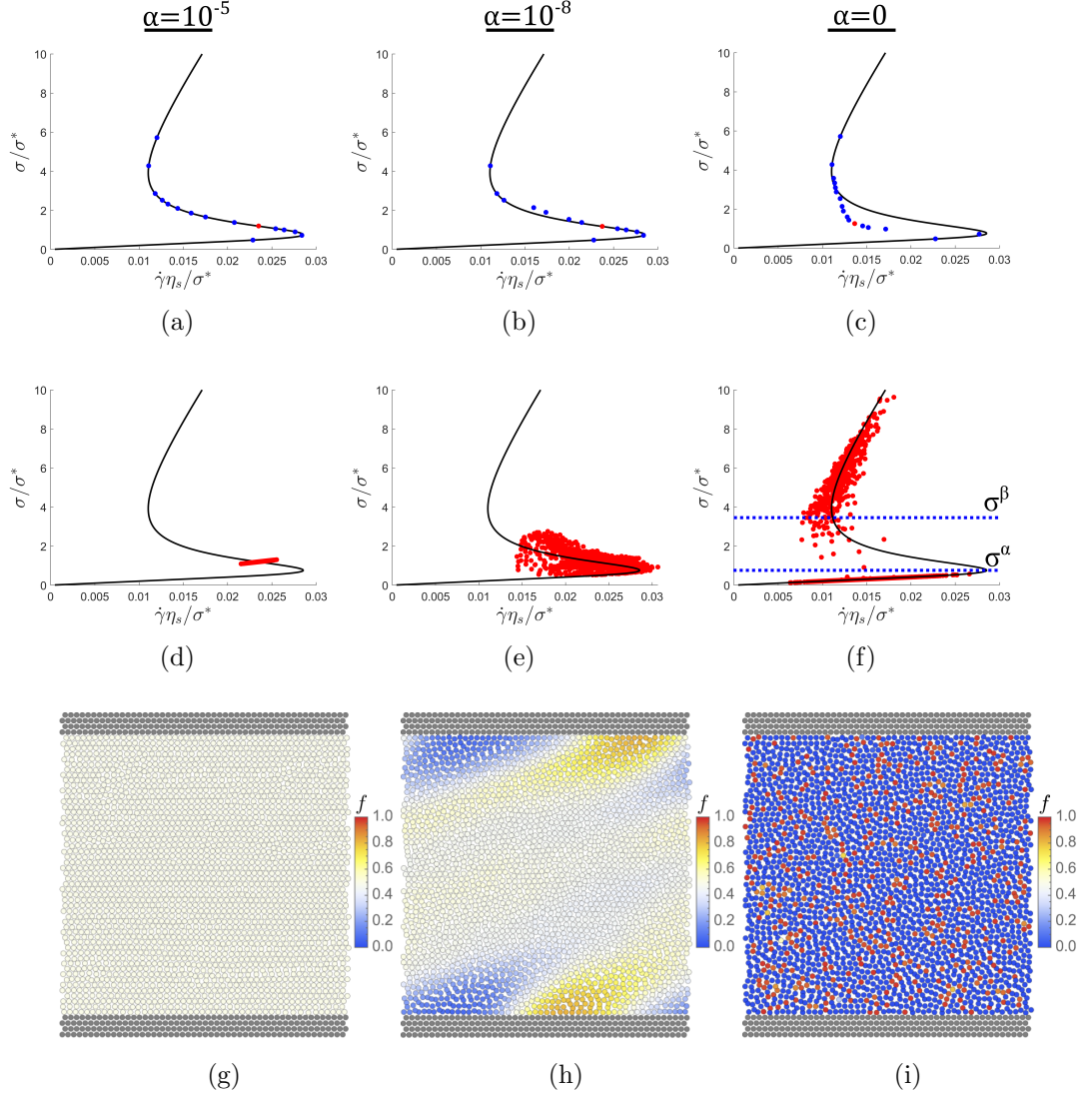


Figure 2.4: The results of the SPH simulation compared against the WC model (black) for strong ((a), (d), and (g)), moderate ((b), (e), and (h)), and zero ((c), (f), and (i)) non-locality. The top row (a)–(c) consists of domain-time averaged shear stress and shear rate signal (SPH in blue and red). A single simulation (red) in each diagram ( $\Sigma_E = 1.25$ ) was chosen, and values of all SPH particles were plotted over the WC flow curve (d)–(f). Fields of the microstructure parameter  $f$  associated with the previously chosen simulations in (d)–(f) visualised in (g)–(i). For high non-locality (g) entire smooth fields of  $f$  and stress are achieved. In case of moderate non-locality (h), two high stress regions are attached to the upper and lower walls with bands propagating in the flow direction. Zero non-locality (i) yields discontinuous microstructure fields.

dimensionless parameters are defined:

$$\psi^1 = \frac{\text{number on the lower branch}}{\text{total number}}, \quad (2.44)$$

$$\psi^2 = \frac{\text{number on the upper branch}}{\text{total number}}, \quad (2.45)$$

$$\psi^u = \frac{\text{number on the unstable branch}}{\text{total number}}. \quad (2.46)$$

The number of particles on either the upper or lower branch is measured with reference to the two threshold stress values  $\sigma^\alpha$  and  $\sigma^\beta$ , which occur at the intersection of the unstable branch with the upper and lower branches, respectively. Typical response consists of a 50 s period for banding process to begin and almost 150 s to 200 s to reach a steady state. Different spatially homogeneous initial configurations were tested, including a) relaxed microstructure ( $f \approx 0$  across space), b) correct steady-state microstructure ( $f$  consistent with the value calculated by WC model at the applied stress set point across space), and c) excessive level of structure ( $f \approx 1$  across space). Due to the local nature of this process, the splitting is independent of the resolution, as there is no finite characteristic length scale associated with this process. All three configurations yielded the same steady-state banding ratios, i.e., the above-mentioned steady-state is broadly independent of the path taken to achieve it. Furthermore, shear-controlled cases were tested both within and outside the multi-valued region and yielded results with no apparent banding; a result consistent with the theory where only stress-controlled flow of DST fluids should experience vorticity banding.

To better understand the exact split between  $\psi^1$  and  $\psi^2$  at steady-state, a simple model of DST vorticity banding is considered. Suppose that stress is applied within the unstable region of the flow curve at a coordinate  $(\dot{\gamma}^u, \sigma^u)$ . This unstable point will split directly in the vertical direction until it meets the lower and upper branches, resulting in a new steady-state consisting of two stable points  $(\dot{\gamma}^u, \sigma^1)$  and  $(\dot{\gamma}^u, \sigma^2)$ , respectively. We also assume that the total average stress is preserved such that:

$$\sigma^u = \psi^1 \sigma^1 + \psi^2 \sigma^2. \quad (2.47)$$

By considering that the system is now in a steady state ( $\psi^1 + \psi^2 = 1$  and  $\psi^u = 0$ ),

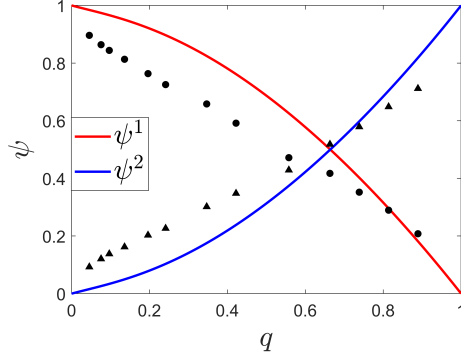


Figure 2.5: Theoretically predicted branch split ratios (lines) vs. simulations. Simulation values represented by black circles ( $\psi^1$ ) and triangles ( $\psi^2$ ) .

both fractions can be uniquely determined for any input stress. It is immediately apparent that the exact split will be governed by the exact shape of the flow curve. Finally, we define a dimensionless stress coordinate  $q$  using critical stress values  $\sigma^\beta$  and  $\sigma^\alpha$  (see Fig. 2.4(f)):

$$q = \frac{\sigma^u - \sigma^\beta}{\sigma^\alpha - \sigma^\beta}, \quad (2.48)$$

such that, for  $q < 0$ , input stress is on the lower stable branch,  $0 \leq q \leq 1$  input stress is on the unstable branch, and for  $q > 1$ , input stress is on the upper stable branch. The results along with simulations are presented in Fig. 2.5. The simulation results exhibit a significantly lower number of particles on the lower branch and a higher number of particles on the upper branch relative to the theoretical predictions. This is due to how the split rearrangement is achieved. Since an even split would result in an increase in the measured shear stress, initial splitting causes the stress-control scheme to reduce shear rate. The shear rate reduction is set by the decrease in wall velocity, which affects all particles, causing a shift to the left in the  $(\dot{\gamma}-\sigma)$  phase diagram. Particles on the upper branch can only shift to the lower branch by crossing the critical stress  $\sigma^\beta$ , where particles can no longer follow the linear relationship between shear rate and shear stress and ‘fall’ down to the stable branch, due to the combined effects of the microstructure evolution equation and the stress-control scheme. This results in the particles on the upper stable branch, occupying

shear stress and shear rate values lower than anticipated in the naive vertical splitting scenario. A lower stress value of  $\sigma^1$  in eq. (2.47) necessitates a higher value of  $\psi^2$  (and a lower value of  $\psi^1$ ) at steady state. This mechanism also accounts for the poor agreement between the simulations and the WC model Fig. 2.4(c) — average shear stress is close to the correct input value, but the splitting causes much lower shear rate values.

Finally, the case of moderate non-locality is considered. The averaged results show good agreement with the WC model Fig. 2.4(b) along the entire flow curve, just as in the homogeneous case. Unlike the homogeneous case, the plot of individual SPH particles in Fig. 2.4(e) shows a clear and significant spread in both shear stress and shear rate. However, this spread is different from the local case — particles occupy mainly the unstable region between the two stable branches. The bands in the microstructure parameter are also accompanied by bands in shear stress and shear rate. This steady state occurs as a result of a balance between the split-inducing local term and the smoothing non-local term in the microstructure evolution equation. Furthermore, the competition between the local and non-local effects yields an apparent spatial correlation in the microstructure field Fig. 2.4(h) reminiscent of the bands observed in the work of Nakanishi et al. [92].

### 2.4.2 Channel Flow

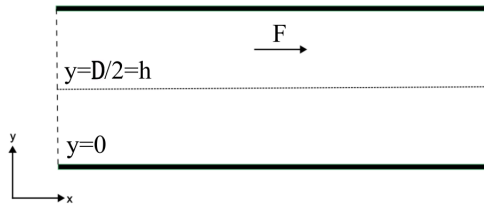


Figure 2.6: Sketch for the channel geometry. The geometry consists of a closed 2D channel with  $u = 0$  at  $y = 0$  and  $\sigma_{xy} = 0$  at  $y = h$ , symmetric at centreline  $y = h$ . The flow is driven solely by a constant body force  $F = \rho g$ .



## Theoretical Analysis

In this section, we consider flow in a planar channel (Fig. 2.6), with gap  $d = 0.01$  m and periodic boundary conditions in the flow direction. Body force  $F$  parallel to the flow direction is applied to all particles. In the following, a derivation of the theoretical solution is provided. We begin by assuming a steady state, well-developed unidirectional ( $\mathbf{u} = (u, 0, 0)$ ) axial flow driven by a body force  $F$ , with no pressure gradient along the flow direction. Eq. (3.2) simplifies to

$$\frac{\partial \sigma_{xy}}{\partial y} = -F = \rho g. \quad (2.49)$$

The constitutive equation for the only non-zero component of the stress tensor is  $\sigma_{xy} = \eta \frac{du}{dy}$  subject to no-slip and vanishing stress boundary conditions  $u = 0$  at  $y = 0$  and  $\sigma_{xy} = 0$  at  $y = h$ .

Integrating eq. (2.49) with appropriate boundary conditions yields solution between  $y = 0$  and  $y = h$

$$\sigma_{xy} = F(h - y). \quad (2.50)$$

Using eqs. (2.4) and (2.5), the constitutive relation can be rewritten to yield an ODE

$$\frac{du}{dy} = \frac{F(h-y)}{\eta_s} \left( 1 - \frac{\phi}{\phi_m \exp\left(-\left[\frac{\sigma^*}{F(h-y)}\right]^\beta\right) + \phi_0 \left(1 - \exp\left(-\left[\frac{\sigma^*}{F(h-y)}\right]^\beta\right)\right)} \right)^2. \quad (2.51)$$

which can be solved via direct integration of the right hand side to obtain shear rate, velocity and viscosity profiles. In this work, the solution was obtained via ODE45 MatLab algorithm with a relative tolerance of  $10^{-8}$ .

## Numerical Results

With the chosen parameters, we focus primarily on the transitional DST regime where both frictional and frictionless states are meaningfully present within the flow

and consider only the purely local case ( $\alpha = 0$ ). At the steady state, the velocity shape of DST flow displays a sharp profile with an upward inflection near the centreline (Fig. 2.7(c)) and are in good agreement with the theoretical solutions of our model. The inflection corresponds to the threshold transition region between primarily frictional and frictionless regimes.

It is worth noting that for the values of frictional and frictionless divergence volume fractions used in this study, the ratio between frictionless and frictional viscosity,  $\bar{\eta}$ , is approximately 30 — far lower than typical magnitudes observed in experimental model systems such as cornstarch, where the viscosity can span multiple orders of magnitude during shear thickening [128; 129]. This low value of  $\bar{\eta}$  was chosen to facilitate feasible simulation run time by avoiding excessively low or high viscosity at any point during shear thickening.

The resulting velocity profiles obtained in SPH simulations and by direct integration of the (2.51) are presented in Fig. 2.7. The driving force (and thus the stress profile) was varied to probe the influence of shear thickening on the shape of the velocity profiles.

For sufficiently low driving forces, the velocity profile remains parabolic (a) due to lack of developed microstructure (b) — viscosity remains close to the lower branch viscosity  $\eta_0$ . The microstructural profile is in good agreement with the theoretical profile, with minor deviation near the centre line. This is due to the initialisation of the structure from a finite value — particles near centre line experience near-zero shear rate, and thus the structure can not evolve to the appropriate steady state. This deviation is not significantly reflected in the velocity profile due to the weak scaling of viscosity with the microstructure at such low values, resulting in an excellent agreement in the velocity profile.

At intermediate driving forces, flow in the centre ( $y/D = 0.5$ ) remains unconstrained; however, the microstructure builds up from the walls (d) towards the centre leading to a sharpened velocity profile (c) with an upward inflection - feature characteristic of the S-shaped rheology. It is apparent that the stress-splitting is present here, with large deviations in the simulated microstructure from the theoretical values. Despite this discrepancy, the simulated velocity profile has very good agreement

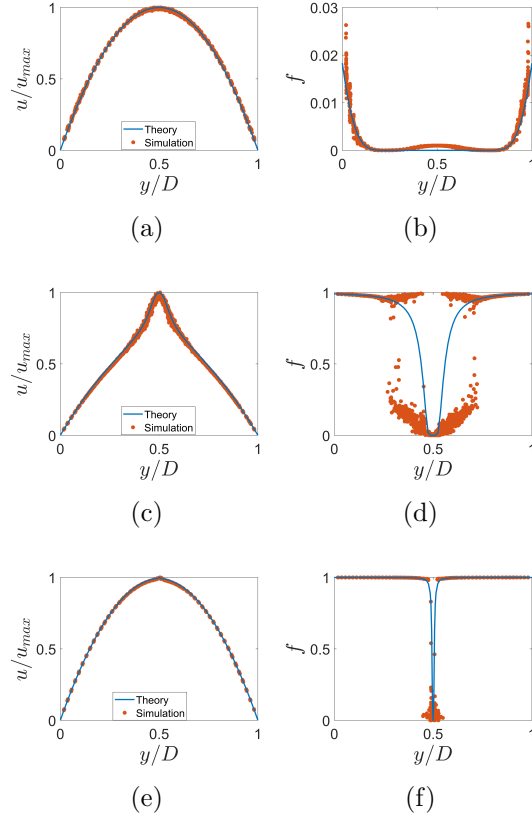


Figure 2.7: Velocity profiles (left) and corresponding microstructural profiles (right) for dimensionless driving forces  $Fh/\sigma^*$  of 0.5 (a)–(b), 10 (c)–(d), and 100 (e)–(f) for  $\phi = 0.54$ . Theoretical solutions for homogeneous WC model in blue and SPH simulations with stress splitting in red.

with the theory. The banding behaviour seems to preserve average velocity, stress, and microstructural profiles within the channel.

Further increase in the driving force leads to almost completely shear frictional flow (f) — the velocity becomes broadly parabolic (e) again with the velocity corresponding to the upper branch viscosity  $\eta_1$ , however, small inflection persists at the tip, where the transition takes place over a very thin region. Any banding behaviour is constrained to the small transitional slice, leading to a deteriorated microstructural

solution near the centre line.

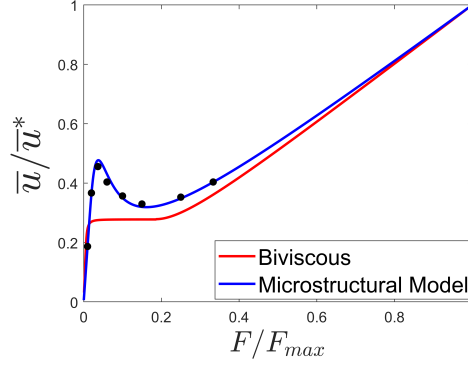


Figure 2.8: Comparison between the present model (blue) and biviscous model [120] (red). Simulations (black) carried out for  $\phi = 0.54$ ,  $\phi^0 = 0.64$ , and  $\phi^m = 0.56$ ,  $\bar{u}$  is the average velocity in the channel, and  $\bar{u}^*$  is an arbitrary average velocity chosen at  $F/F_{\max} = 1$ . The upper and lower viscosity in the biviscous model re-scaled to match frictionless and frictional viscosity.

The model was compared to the simplest DST model, i.e., inverse biviscous [120] previously implemented in SPH. The biviscous model consists of a piecewise viscosity function, where low or high viscosity is attained as a function of the local shear rate in relation to a critical threshold shear rate parameter. In its most basic form, the viscosity function is itself discontinuous, but it has been modified to include a linear viscosity transition regime to connect high and low viscosity plateaus (note that even here, discontinuities still arise). Due to its piecewise implementation, and the lack of microstructural 'memory', the inverse biviscous model does not predict S-curves, rather, it produces two Newtonian branches with a discontinuity at the threshold shear rate values, such that  $d\gamma/d\sigma > 0$  for all cases. The two models were compared by plotting the average velocity for a range of driving forces (Fig. 2.8) for an equivalent viscosity ratio. The biviscous model predicts two branches corresponding to lower and upper viscosities, joined together by a plateau where increasing the driving force does not affect the average flow. The model presented in this work exhibits similar low and high viscosity branches; however, the conjoining region

exhibits a flow reduction pattern unique to the S-shape rheology. It is noteworthy that the presence of a negative flow curve gradient is not always sufficient on its own — a certain minimum viscosity ratio is required to achieve flow reduction behaviour.

## 2.5 Conclusions

In this work, we have presented the first implementation of a microstructural model of discontinuous shear thickening in SPH simulations. A simple non-local scalar microstructural evolution equation based on the work of Baumgarten and Kamrin [26] was proposed and implemented in simple shear and channel geometries. Measured transients in shear rate were found to be in qualitative agreement with experimentally measured shear rates under constant imposed stress.

The simple shear results were used to construct flow curves and compare the macroscopic results with the microscopic WC model which we employ. Simulation results were in good agreement along lower or upper viscosity branches and predicted the characteristic ‘S-shape’ transition between them. In the absence of non-locality, the stress-splitting instability has been observed as a result of the action of the local term in the microstructure evolution equation upon small numerical perturbations in the shear rate field. The resulting steady state was found to be characterised by correct domain-averaged shear stress, despite all SPH particles occupying stable upper and lower branches, lack of spatial correlation, and a low shear rate relative to the WC model. Both the low shear rate and the discrepancy between theoretical and measured split ratios were contextualised in terms of the particle rearrangement mechanism resulting from the stress-control scheme. Both moderate and strong non-locality yielded good agreement in average shear rate and shear stress, with banding spatial correlation being observed in the case of moderate non-locality.

Channel flow simulations showed excellent agreement in velocity profiles with the theoretical solution of the WC model across a range of driving forces. Once channel flow is forced into the intermediate DST regime, the velocity profile forms an upward inflection as a result of the S-shaped rheology. Stress-splitting was observed in the

channel flow, with no discernable impact on the agreement between the theoretical and simulated velocity profiles. Comparison in channel flow was made with the inverse biviscous mode [120]. The present S-shape microstructure model produced a flow reduction behaviour, in contrast to the flow plateau displayed by the biviscous model.

Further study is required to assess stability of the present model and implementation. Exhaustive assessment of the stress-splitting phenomena, band spatial correlation, and the associated characteristic length scale is required. Reproduction of known instability phenomena [76; 58] along with introduction of depth in the vorticity direction could provide further insight into the chaotic rheology of the DST materials.

## Chapter 3

# Numerical Simulations of Spatiotemporal Instabilities in Discontinuous Shear Thickening Fluids

### 3.1 Introduction

Discontinuous shear-thickening (DST) dense suspensions of non-Brownian particles are characterised by a rapid increase in viscosity, attributed to a transition from a frictionless state to a frictional state facilitated by a shear stress sufficient to overcome the characteristic stress scale  $\sigma^*$ , inherent to the particular nature of the suspension particles and solvent [51; 52; 54; 130]. The distinguishing feature of DST as opposed to continuous shear-thickening (CST) is the presence of a negative gradient of the flow curve ( $d\dot{\gamma}/d\sigma < 0$ ), due to the increase in viscosity spanning multiple orders of magnitude [6]. Recently, the stability properties of DST materials have been a subject of extensive research [131], partly because of their potential for understanding the role of internal microstructure in flows applicable to rheometric conditions and large-scale free surface flows.

Instabilities in rheometric flows are of particular interest due to their role in the difficulties associated with the characterisation of DST materials [6] under typical simple shear conditions. In stress-controlled conditions, DST fluids exhibit aperiodic or almost periodic oscillations in the measured shear rate and normal stress [8]—a phenomenon often referred to as ‘rheochaos’. The onset of the instability occurs at a critical stress and grows in strength up to a point, after which further increases in stress reduce the amplitude.

A plausible explanation for the observed temporal instability is the existence of an accompanying spatial instability. Dense frictional suspensions are understood to form contact force networks [53; 52], facilitating stress transmission. As such, it is reasonable to expect that large magnitude temporal fluctuations in normal stress are associated with formation, destruction, and rearrangement of the internal microstructure. Based on the multi-valued nature of the flow curve, DST materials could be expected to undergo formation of bands along the vorticity direction [132]; however, the existence of stable vorticity bands can be ruled out on the basis of particle pressure balance at the band interface [8]. In fact, instead of stable vorticity bands, transient vorticity banding has been reported [86].

A further connection between spatial and temporal instabilities comes from recent literature utilising direct online measurements of the internal fluid state. Force and pressure sensors have been used to detect localised regions of high and low pressure travelling in the direction of flow [133]. Ultrasonic echography has yielded direct imaging of bands propagating in the vorticity direction during temporal oscillations [134]. Perhaps the most illuminating direct imaging comes from recent work [135; 90; 91] using boundary stress microscopy (BSM), in which the stress exerted on the bottom plate in a parallel plate setup can be imaged in real time along with the movement of individual particles via particle image velocimetry (PIV). BSM imaging revealed regions of localised high stress (a peak magnitude of an order larger than the bulk) in simple and oscillatory shear. Tracking these solid-like phases (SLPs) over time allowed for inference of the existence of SLPs at the upper and lower plate boundaries moving with the velocity close to their proximate solid boundaries.

Continuum modelling of DST fluids ubiquitously begins with the definition of the



characteristic S-shaped flow curve, primarily through the Wyart–Cates (WC) model [51], with some exceptions [92; 122]. The WC model is a phenomenological approach, with solid microscopic evidence [53], that proposes that particles are held apart by a characteristic repulsive force  $F_0$  which sets the characteristic stress scale  $\sigma^*$ . Below the characteristic stress scale, the particles are held apart in a low-viscosity, frictionless state. When a stress is applied above the onset stress, the particles enter frictional contact and rapidly increase the viscosity. The key parameter in the WC model,  $f(\sigma)$ , represents the fraction of particles in a frictional contact at a given stress. Most works on continuum modelling use this scalar parameter [133; 26; 58; 87], along with a microstructural evolution equation, which seeks to describe the dynamics of the frictionless-to-frictional transition. Typically, the rate of evolution is a rate-dependent approach of  $f$  towards the WC prescribed steady-state value  $\hat{f}(\sigma)$  at a given stress.

One potential mechanism of temporal instabilities identified in the literature comes from competition between the timescales of system-inertia ( $t_i$ ) and microstructure formation ( $t_f$ ) [76]. Stability analysis of the coupled dynamics of a stress-controlled plate and the commonly used local form of the microstructure evolution equation reveal that such a system can undergo a Hopf bifurcation. When the rate of formation is much higher than the rate of boundary deceleration ( $t_i \gg t_f$ ), an overshoot in the shear rate will induce rapid shear thickening, which in turn will further increase the material stress since the plate cannot decelerate sufficiently quickly, resulting in a feedback loop. In addition to the required ratio of timescales, negative gradients of the flow curve are also necessary, indicating that this mechanism is unique to DST materials. The primary limitation in the analysis associated with this mechanism is the inherent assumption of homogeneous space, which clearly does not account for the spatial pattern formation observed in real systems. Furthermore, because of the two-dimensional aspect of the system in phase space, only periodic oscillatory solutions are possible, which limits the applicability to a narrow region in which periodicity is observed in experiments.

Alternatively, coupling of the simple evolution of the scalar microstructure with the dynamic migration of particles through the suspension balance model [58] has

been shown to produce transient vorticity banding, uniquely for DST conditions. The observed pattern formation was shown to be in a good agreement with direct particle simulations; however, the continuum modelling was limited to a gradient–vorticity space, with assumption of spatial homogeneity in both flow and gradient directions.

In this work, we present a systematic study of the possible interactions between the microstructural, inertial, and stress-diffusive timescales, by framing pattern formation in the context of a competition between local and non-local contributions to the microstructure evolution, in the presence of DST rheology. In Section 3.2.1, we outline the continuum model and numerical implementation, respectively. In Section 3.3.1, we consider the case of dominant non-locality for the purpose of validation of our SPH model against a temporal instability mechanism proposed in the literature. In Section 3.3.2 we demonstrate the stress-splitting instability inherent in the shape of DST flow curves. Finally, in Section 3.3.3 we consider regimes of mixed non-locality where spatial pattern formation is possible and present an alternative mode of temporal instability, driven by variations in microstructural spatial patterns within the geometry.

## 3.2 Method

### 3.2.1 DST - continuum scalar model

The governing equations, written in the Lagrangian frame, are

$$\frac{D\rho}{Dt} = -\rho \nabla \cdot \mathbf{v}, \quad (3.1)$$

$$\frac{D\mathbf{v}}{Dt} = \frac{1}{\rho} \nabla \cdot \boldsymbol{\sigma} + \mathbf{a}, \quad (3.2)$$

$$\boldsymbol{\sigma} = -p\mathbf{I} + \eta (\nabla \mathbf{v} + \nabla \mathbf{v}^T), \quad (3.3)$$

where  $D/Dt \equiv \partial/\partial t + \mathbf{v} \cdot \nabla$  is the material derivative,  $\rho(\mathbf{x}, t)$  is the density field,  $\mathbf{v}(\mathbf{x}, t)$  is the velocity field,  $\boldsymbol{\sigma}(\mathbf{x}, t)$  is the stress field,  $p$  is the pressure, and  $\mathbf{a}$  is the acceleration due to body force acting on the fluid.

The viscosity of the suspension is defined by the Maron–Pierce relation [41]

$$\eta(\phi, \phi^J, t) = \eta_s \left(1 - \frac{\phi}{\phi^J}\right)^{-2}, \quad (3.4)$$

where  $\eta(\phi, \phi^J, t)$  and  $\eta_s$  are, respectively, the suspension and constant solvent viscosities. The divergence volume fraction,  $\phi^J$ , is used to introduce shear thickening by interpolating its value between the frictionless state ( $\phi^0$ ) and the frictional state ( $\phi^m$ ),

$$\phi^J(f(\mathbf{x}, t)) = \phi^m f(\mathbf{x}, t) + \phi^0 \{1 - f(\mathbf{x}, t)\}. \quad (3.5)$$

Here, the interpolating state parameter,  $f(\mathbf{x}, t)$ , is interpreted as the fraction of particles in frictional contact at a given position in space, as defined in the WC model. The dynamics of the state parameter is defined via the microstructure evolution equation:

$$\frac{Df(\mathbf{x}, t)}{Dt} = k_f \dot{\gamma} \left( \hat{f}(\mathbf{x}, t) - f(\mathbf{x}, t) \right) + \alpha \nabla^2 f(\mathbf{x}, t), \quad (3.6)$$

$$\hat{f}(\mathbf{x}, t) = \exp\left(-\left[\frac{\sigma^*}{\sigma(\mathbf{x}, t)}\right]^2\right), \quad (3.7)$$

which consists of a local term modelling the approach of the system towards a stress-prescribed WC steady state,  $\hat{f}(\mathbf{x}, t)$ , and a non-local term modelling stress-diffusive components of microstructure formation in space. The local contributions are tuned with a microstructural rate constant,  $k_f$ , whereas the non-local dynamics are set by the microstructure diffusivity parameter,  $\alpha$ . The fluid stress is calculated as  $\sigma = \eta \dot{\gamma}$ , where  $\dot{\gamma}(\mathbf{x}, t) = \sqrt{\dot{\gamma} : \dot{\gamma} / 2}$  is the local shear rate calculated as the second invariant of the strain rate tensor  $\dot{\gamma}(\mathbf{x}, t) = (\nabla \mathbf{v} + \nabla \mathbf{v}^T) / 2$ .

### 3.2.2 Numerical Implementation

In all simulations, unless otherwise noted, we use the WC parameters  $\phi = 0.54$ ,  $\phi^J = 0.693$  and  $\phi_m = 0.562$ , resulting in a well-defined 'S'-shaped flow curve [136]. In Sections 3.3.1 and 3.3.2, we simulate a square box with a gap height of  $h = 0.01$  m, while, in Section 3.3.3, we use a wide box  $l = 3h$  with the same gap height to fully

capture the resulting spatial pattern. In all simulations, the numerical resolution is kept constant at  $\Delta x = h/50$ .

We simulate simple shear in stress-controlled mode by setting the velocity on the upper wall ( $v_w$ ) and evolving it over time:

$$\frac{dv_w}{dt} = k_p(\sigma_E - \sigma), \quad (3.8)$$

where  $\sigma_E$  is the target stress set-point,  $\sigma$  is the shear stress measured at the upper wall, and  $k_p$  is a tuning parameter in the control scheme. A small value for  $k_p$  corresponds to slow adjustment of velocity in response to rheological changes (high system inertia). A large value for  $k_p$  corresponds to fast adjustment (low system inertia). The microstructural field,  $f(\mathbf{x})$ , and the shear rate,  $\dot{\gamma}$ , are initialised, in most cases, from a steady state exactly on the WC flow curve corresponding to the stress set-point, with  $f(\mathbf{x})$  uniform.

### 3.2.3 Dimensional Analysis

The dynamics of our model is captured by three characteristic timescales:

$$t_i = \frac{h}{k_p \eta_s}, \quad t_f = \frac{\eta_s}{k_f \sigma^*}, \quad t_d = \frac{L^2}{\alpha}, \quad (3.9)$$

where  $t_i$  is the system-inertia timescale,  $t_f$  represents the local microstructure evolution timescale, and  $t_d$  is the microstructure diffusive (or non-local) timescale. The relevant length scale,  $L$ , is the numerical resolution length,  $\Delta x$ , allowing us to interpret the non-local term as an artificial diffusive term, where the resolution can be scaled out as  $\alpha = \alpha' L^2$ . We proceed by defining the dimensionless parameters

$$\Sigma = \frac{\sigma}{\sigma^*}, \quad \dot{\Gamma} = \frac{\dot{\gamma} \eta_s}{\sigma^*}, \quad \epsilon = \frac{t_f}{t_i}, \quad \omega = \frac{t_d}{t_i}, \quad (3.10)$$

where  $\Sigma$  is the dimensionless stress,  $\dot{\Gamma}$  is the dimensionless shear rate,  $\epsilon$  and  $\omega$  are local and non-local microstructural timescales, respectively, normalised with the inertial timescale.

The corresponding nondimensional forms of the microstructural evolution equation (3.6) and the stress control equation (3.8) are given by:

$$\frac{df(\tilde{\mathbf{x}}, t)}{d\tilde{\tau}} = \frac{\dot{\Gamma}}{\epsilon} \left( \hat{f}(\tilde{\mathbf{x}}, t) - f(\tilde{\mathbf{x}}, t) \right) + \frac{1}{\omega} \nabla^2 f(\tilde{\mathbf{x}}, t), \quad (3.11)$$

$$\frac{d\dot{\Gamma}}{d\tilde{\tau}} = \Sigma_E - \Sigma, \quad (3.12)$$

where  $\tilde{\mathbf{x}} = \mathbf{x}/L$  and  $\tilde{\tau} = t/t_i$ .

### 3.3 Numerical results

#### 3.3.1 Dominant Non-Locality

To classify relative magnitudes of local and non-local contributions to the evolution of microstructure, we define a characteristic stress-diffusive length scale,

$$l_c = \sqrt{\frac{\alpha}{k_f \dot{\gamma}}}, \quad (3.13)$$

which determines the spatial scale of potential pattern formation. In this section, we consider an entirely homogeneous state by setting  $l_c \approx h$ . We set  $k_f = 1$ , and since in the flow curve range of interest  $\dot{\gamma} = O(10^{-1})$ , using  $\alpha = 10^{-5}$  allows for characteristic length scale spanning approximately the entire spatial domain (see Table A.1 for full parameter list).

In the extreme case of dominant non-locality, we can expect an entirely homogeneous state, and due to the vanishing gradients of  $f(\mathbf{x})$ , we can simplify the dynamic model equations by neglecting the effects of the stress-diffusive term (last term in Eq. (3.11)) on the stability of the dynamics. Doing so simplifies the equations to a system directly equivalent to the one studied by Richards et al. [76], allowing a comparison to their stability analysis. Following their analysis, the stability criterion for the mechanism based on the competition of the system-inertia timescale ( $t_i$ ) and the microstructural formation timescale ( $t_f$ ) can be written as

$$\frac{t_f}{t_i} < -\dot{\Gamma} \frac{d\dot{\Gamma}}{d\Sigma_E}, \quad (3.14)$$

which, if satisfied, indicates unstable dynamics and the existence of periodic solutions. The condition can be rewritten into a more convenient formulation with the overall stability parameter

$$\mu = - \left( \frac{k_p \eta_s^2}{k_f \sigma^* h} + \dot{\Gamma} \frac{d\dot{\Gamma}}{d\Sigma_E} \right), \quad (3.15)$$

the system has all bifurcation points at  $\mu = \mu_c = 0$ , with stable solutions for  $\mu < 0$  and periodic solutions for  $\mu > 0$ . The stable solutions consist of an inward spiral towards the exact solution on the WC model, resulting in a steady state where the system lies exactly on the flow curve for any stress applied, regardless of the presence of DST [136]. The bifurcation occurs when the response of the stress control mechanism is no longer fast enough to deal with the overshoots in the shear rate, leading to an increasing shear rate at the point of a large DST viscosity jump, which further increases the stress and thus drives the particles into an even more frictional state, initiating a positive feedback cycle of increasing viscosity and stress. Eventually, the direction of stress control will invert, initiating a similar feedback loop in the opposite direction, and completing the limit cycle as shown in Fig. 3.1(a). To evaluate the capability of the SPH model to handle instabilities, we varied  $k_p$  to obtain unstable solutions and measured the amplitude of the apparent oscillations (Fig. 3.1(b)) in spatially-averaged dimensionless shear rate,  $\Delta\dot{\Gamma}$ , in both our SPH results and the results obtained via alternative direct numerical integration (DNI) of the ODEs (Eq. (3.11) and Eq. (3.12)). Direct integration was carried out with the ODE45 Matlab algorithm with a relative tolerance of  $1 \times 10^{-10}$  and smoothed with the Savitzky-Golay algorithm with a window size of 5 subsequent points (less than 0.5% of points) to correct the random numerical errors introduced by the solver. Comparison between SPH simulations and the direct integration of the dynamics equations (3.11) and (3.12) shows clear congruence between the two. The plots of the shear rate amplitude measured in SPH for both gap heights (Fig. 3.1(b–d)) show clear bifurcation in line with the predicted bifurcation condition, marked by a sudden increase in amplitude at  $\mu = 0$ . Furthermore, the SPH model is capable of accurate predictions of exact limit cycle sizes (Fig. 3.1(b)) along the shear rate dimension for

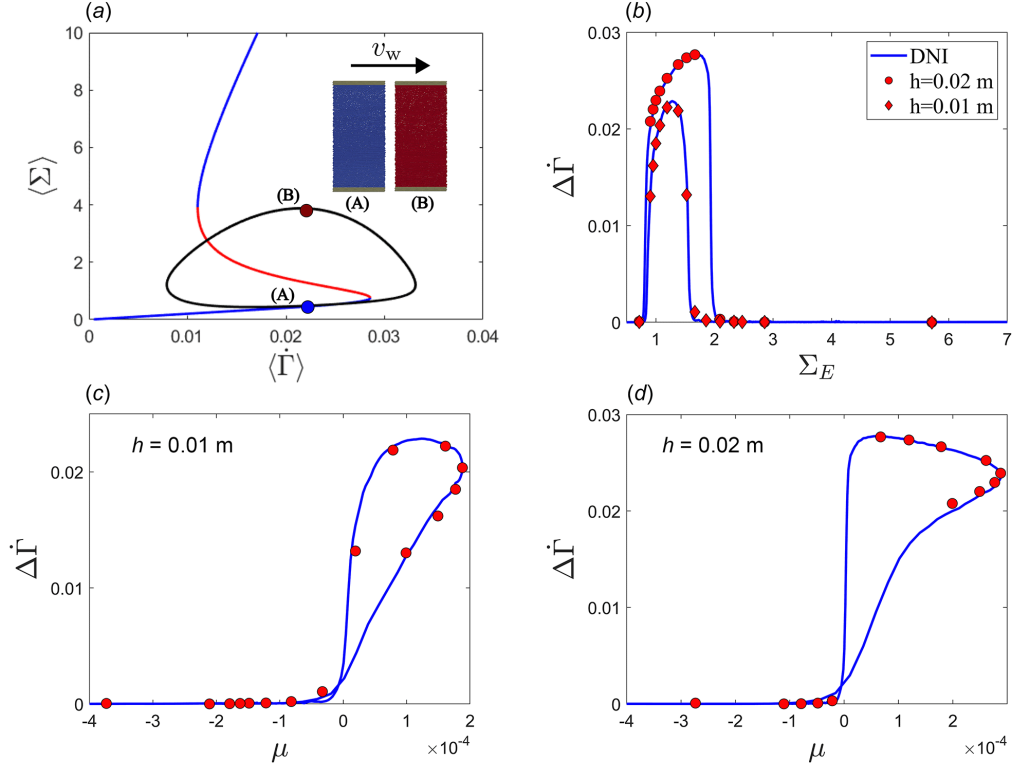


Figure 3.1: (a) A typical trajectory of an unstable solution ( $\alpha = 10^{-5}$ ) exhibits periodic cycling between entirely frictionless and frictional domain (microstructural fields are entirely homogeneous across the entire system size). The trajectory is based on the spatially averaged stress and shear rate, and is plotted over a WC model flow curve where blue and red segments indicate regions of positive and negative gradients. The inset shows simulation frames of typical microstructural states  $f$  during the minima (A) and maxima (B) of stress along the trajectory, where (A) is uniformly frictionless (blue) and (B) is uniformly frictional (red). (b) Comparison of limit cycle size  $\Delta\dot{\Sigma}$  as a function of  $\Sigma_E$  along the range of the flow curve shows an increase in peak and broadening of the bifurcation points with increasing gap height. (c) and (d) show stability diagrams  $\Delta\dot{\Sigma}(\mu)$  for  $h = 0.01$  m  $h = 0.02$  m respectively. Blue lines indicate solutions obtained by direct numerical integration of equations (3.11) and (3.12), and red points are measurements from SPH simulations.

a range of imposed stress values ( $\Sigma_E$ ) spanning the entire frictionless-to-frictional transition of the flow curve. This agreement is illustrated in Fig. 3.1(b) for two different geometry gap heights.

### 3.3.2 Vanishing Non-locality

Having validated our implementation in the regime of homogeneous state, we can now consider instabilities with spatial heterogeneity. Here we consider the limit of vanishing non-locality. Strictly, we set  $l_c = 0$  and thus exclude non-locality entirely, but as we will show later, we can expect the following analysis to hold for  $l_c < L$ , as any patterns with characteristic length below the resolution scale will not be resolved (see Table A.2 for full parameter list). In this and the following sections, we consider the regime of  $\mu < 0$  and  $d\dot{\gamma}/d\sigma < 0$  to investigate primarily spatial effects while excluding the temporal instability discussed in the previous section.

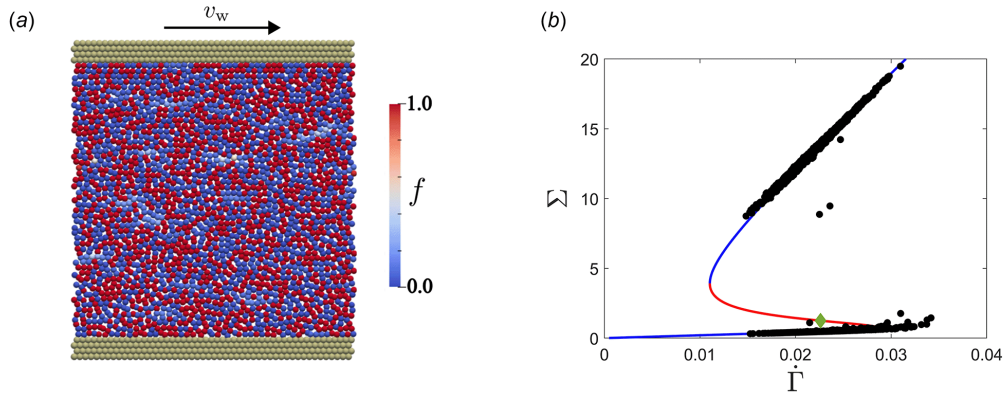


Figure 3.2: (a) The field visualisation of  $f$  in steady state ( $\alpha = 0$ ) in shear rate controlled mode exhibits nondifferentiable microstructure (and stress) fields. The value of  $f$  varies between the entire allowable range at the scale of numerical resolution. (b) Individual SPH particles plotted on top of the theoretical WC curve. The particles split onto the two stable segments. Green diamond indicates initialisation state.



We start by considering two particles in  $\dot{\gamma}$ - $\sigma$  phase space with coordinates  $A(\dot{\gamma}^*, \sigma^*)$  and  $B(\dot{\gamma}^* + \delta\dot{\gamma}, \sigma^*)$ , respectively, where particle  $A$  lies exactly on the flow curve predicted by the WC model for a given input stress set-point (indicated by the superscript  $\sigma^*$ ) and the particle  $B$  receives a small positive perturbation in shear rate (see Appendix B for a diagram). Since the perturbation is horizontal, point  $B$  preserves the stress such that

$$\sigma_A = \sigma_B, \quad (3.16)$$

which can be rewritten as

$$\eta_A \dot{\gamma}^* = \eta_B (\dot{\gamma}^* + \delta\dot{\gamma}). \quad (3.17)$$

This implies that the viscosity at  $B$  must be less than the viscosity at  $A$ , from which we can infer that

$$\hat{f} - f_B > 0 \quad (3.18)$$

for any particle  $B$  to the right of the flow curve.  $\hat{f}$  is the steady state WC value at a given stress  $\Sigma$ , and  $f^*$  indicates the steady state value corresponding to the applied stress  $\Sigma_E$ . Notice that this is part of the local term in the microstructure evolution equation; hence, we can deduce that for any point to the right of the flow curve, the vector fields of the microstructure evolution must point directly upward in phase space, as the evolution of  $f$  is positively correlated with the evolution of stress. By the same argument, we can also show that the vector fields to the left of the flow curve must always point downwards. For flow curves with monotonous positive gradient ( $d\dot{\gamma}/d\sigma > 0$ ), the resulting vector fields will always return any perturbed points to the flow curve. However, whenever negative gradients of the flow curve are present ( $d\dot{\gamma}/d\sigma < 0$ ), the vector field acting on the point will move it away from the flow curve. On the basis of this analysis, we can expect a spatial instability unique to the DST regime, where individual SPH particles receiving random numerical perturbations will ‘split’ along the stress axis.

To confirm this behaviour, we performed rate-controlled simulations, in which the shear rate was maintained by a constant upper wall velocity. All particles were initialised with the same state exactly on the WC flow curve in the unstable region. The resulting field of  $f$  (Fig. 3.2(a)) becomes discontinuous at the resolution level,

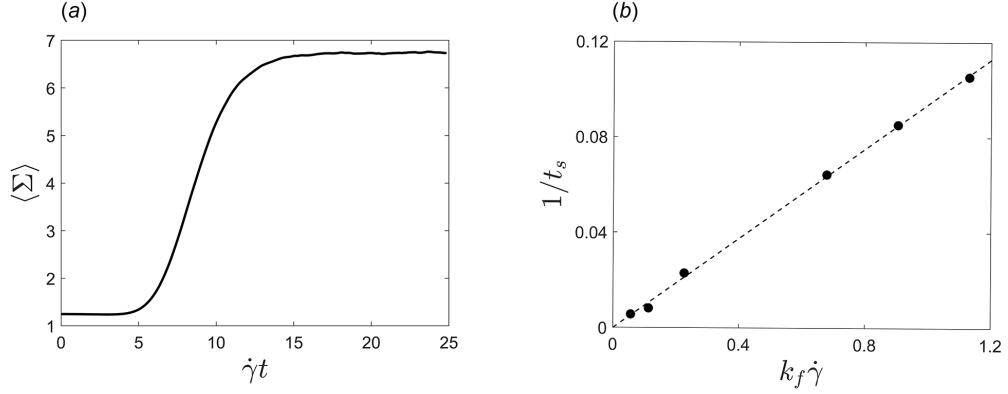


Figure 3.3: (a) Transient in average stress induced by the splitting of SPH particles for  $k_f = 1$ . (b) Plot of the rate of stress equilibration against the prefactor  $k_f \dot{\gamma}$  of local contributions to the microstructure evolution.

with a lack of clear continuous spatial patterns, like the ones observed in the experiments [91]. In the  $\dot{\gamma}$ - $\sigma$  space, individual particles (Fig. 3.2(b)) are attracted to the stable Newtonian branches of the flow curve, where the vector fields act as a restoring force. The number of particles that split “upwards” and “downwards” is approximately equal because of the randomness in the numerical noise that places particles arbitrarily on either side of the WC flow curve.

The dynamics of the instability were probed by varying  $k_f$  in Eq. (3.6). The typical transient response during the instability (Fig. 3.3(a)) consists of a significant increase in the average stress within the domain, the lower stress plateau indicating the homogeneous initial state and the upper stress corresponding to the entirely split state. The increase in stress is a result of an even number split in SPH particles along an asymmetric flow curve, with a much higher jump upward toward the frictional branch than the downward jump to the frictionless branch. In this case, the dynamics of stress evolution can be used as a proxy for the dynamics of the instability. For each value of  $k_f$ , we define and measure a splitting equilibration time,  $t_s$ , which corresponds to the time required to attain 95% of the upper stress value. The plot of inverse equilibration time (or the rate of equilibration) against the prefactor of

the local term in the evolution (Fig. 3.3(b)) reveals a direct relation between the dynamics of stress-splitting and the dynamics of the local microstructure evolution, in line with the argument above based on Eq.(3.18).

### 3.3.3 Moderate Non-Locality

We can expect the extent of inhomogeneity in the microstructural fields to be governed by the balance of local and non-local dynamics captured by the characteristic length scale  $l_c = \sqrt{\alpha/k_f\dot{\gamma}}$ . When  $l_c$  is small, microstructural fields are strongly inhomogeneous (and discontinuous) due to the dominant stress-splitting effects. When  $l_c$  is large, diffusion dynamics dominate resulting in entirely homogeneous fields. It is noteworthy, that the definition of  $l_c$  includes  $\dot{\gamma}$  which can vary in time (and space), which implies possible variations of microstructural field ‘smoothness’ in time. It is plausible that some intermediate region exists when the characteristic length falls below the domain size, but above the resolution, to produce inhomogeneous but continuous spatial flow fields. To explore the parameter space we carry out stress-controlled simulations for a range of values of  $\alpha$  (see Appendix Table A.3), at a constant stress set-point ( $\Sigma_E = 1.25$ ). At the extremes of the range, previously discussed scenarios associated with vanishing and dominant non-locality were present. However, for intermediate values of  $l_c$  new patterns arise, characterised by significant spatial inhomogeneity combined with smooth, continuous microstructural gradients.

The typical fields associated with this regime are visualised in Fig. 3.4, including fields of viscosity (Fig. 3.4(a,d,g)), local (Fig. 3.4(b,e,h)) and non-local (Fig. 3.4(c,f,i)) contributions to the rate of microstructure formation. The fields shown correspond to a simulation with typical characteristic length  $l_c = 0.0316h$ , and for a stable parameter configuration for the boundary-driven instability ( $\mu = -1.96 \times 10^{-2}$ ). With the addition of moderate non-locality, the stress-splitting acts as a seeding instability, which after an induction period results in microstructure organised in clumps of high viscosity (or solid-like phases - SLPs) material attached to the wall boundaries. Both clumps travel in the direction of the flow with velocities approximately equal to the flow near their respective boundaries, resulting in a periodic scenario

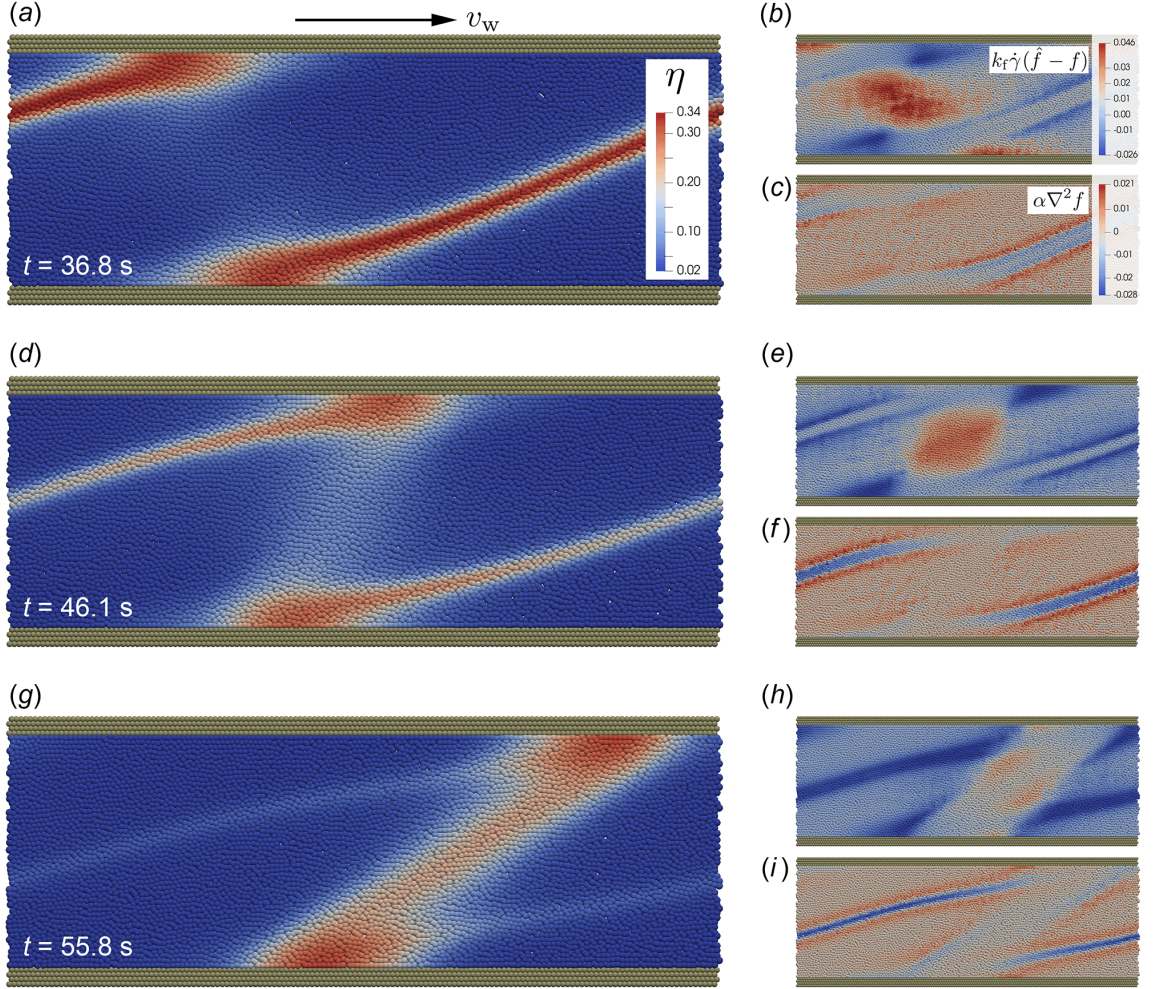


Figure 3.4: Simulation time series showing solid-like phases (red) at the top and bottom wall connected by a thin band. The large panels (a,d,f) show viscosity fields. The upper and lower smaller panels (b,c and e,f and h,i) show local and non-local contributions to microstructure formation as per Eq. (3.6). The snapshots shown capture the process of a typical oscillation: just before constriction (a), during constriction (b), and after constriction (c). Simulation parameters:  $l_c = 0.0316h$  and  $\Sigma_E = 1.25$ .

in which the upper SLP passes over the lower SLP, due to the periodic boundary in the flow direction, where the period of the passing is in part determined by the geometry length. Fig.3.4(a) shows a situation where two previously formed SLPs on the upper and lower plate are approaching each other as the upper plate moves from left to right. The two SLPs are connected by a long band of high-viscosity (frictional state) material which formed in the previous cycle, the last time the SLPs passed each other. During the approach (Fig.3.4(a)), SLPs begin forming a constriction thereby deforming the flow fields between them. This produces a region of elevated high-shear in the constriction space (compressive direction) where the local term in the microstructure evolution equation (Fig.3.4(b)) pushes  $f$  towards the frictional branch, beginning the formation of a new high-viscosity connecting band as can be seen clearly in (Fig.3.4(d)). Once the SLPs have passed each other and the constriction is resolved (Fig.3.4(g)), the newly formed connecting band continues to increase in viscosity, while the previous old band is stretched thin allowing for diffusion to overcome the microstructure-building contributions localised within the band, and the band dissipates.

During each pass, the average shear rate and stress oscillate (Fig.3.5(a,b)) as a result of flow field deformation, and formation and dissipation of the connecting high-viscosity band. During each cycle, the shear rate between the snapshots shown in Fig.3.4 (a, d, g) decreases, before again increasing. Looking at the initial field of local contributions to the microstructure formation (Fig.3.4(b)), we observe that the formation of the connecting band begins during the approach (compressive direction) and is driven by the local elements of the model. During the cycle, the viscous band appears in a subsequent time step, where the formation rate is not at its maximum (Fig.3.4(e)), due to the delayed nature of microstructure formation. In general, as the shear rate decreases, the local contributions to the microstructure evolution decrease in magnitude (Fig.3.4 (b, e, h)), while the non-local effects are enhanced (Fig.3.4(c,f,i)). This behaviour is in accordance with definition of  $l_c$ , where the extent of splitting is mediated by the shear rate due to the varying balance of local and non-local forces.

The present view of spatial patterns is broadly consistent with that proposed



by [91] on the basis of boundary stress microscopy (BSM), wherein they infer the existence of high-stress SLPs at wall boundaries. Their SLP formation can occur on both boundaries [135] or a single boundary, whereas in our simulations, with the particular parameter values described here, two SLPs — one on each wall — are always formed. Our model also does not display the rich dynamics of pattern formation in the wake of the SLP interaction [90]. Regardless, our simulations capture the broad picture of the spatial pattern and demonstrate a mode of temporal instabilities induced by the formation and evolution of a distinct spatial arrangement of the microstructure. Our result can also be viewed in congruence with the work of Nakanishi et al. [92], where similar geometry-spanning bands of microstructure were reported, and a mode of inhomogeneous oscillatory flow was presented.

The spatial pattern was further characterised by measuring the stress distribution along a line going through the SLP a small distance away from, and parallel to, the upper wall. ( $5 \times 10^{-4}$  m). As the non-locality ( $\alpha$ ) is increased at constant local parameters, the SLPs become broader, while the peak stress inside the SLP decreases (Fig. 3.5(c)). Measured stress profiles were fitted to a normal distribution, measuring their standard deviation,  $A$ , as a proxy measurement for the characteristic length. The resulting fit (Fig. 3.5(d)) confirms SLPs grow in width with the square root of the diffusion coefficient,  $\sqrt{\alpha}$ , or in other words, linearly with the characteristic length scale Eq.(3.13).

### 3.3.4 Viscosity Ratio

A major difference between the present results and the experimental work on a stress-controlled system lies in the permanence of the SLPs. During BSM measurements in a *shear rate* controlled system, the SLPs are persistent in time Rathee et al. [90, 91], but in a stress-controlled mode the SLPs are observed to dissipate during the oscillatory behaviour of the system. The proposed mechanism for this relies on the large stress fluctuations measured via BSM, which act through the stress-control scheme to sharply reduce the shear rate below the critical value,  $\dot{\gamma}_c$ , allowing SLPs to erode. The dissipation of SLPs will cause the total stress acting on the plate to

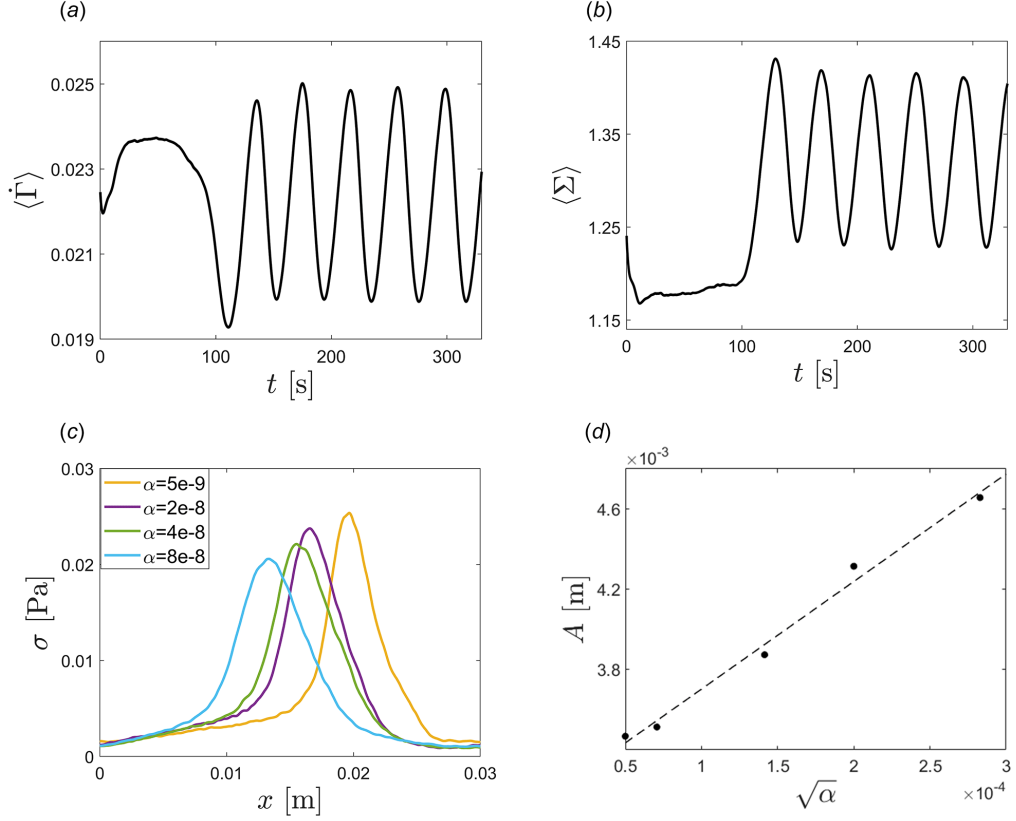


Figure 3.5: Typical average shear rate (a) and stress (b) measured during oscillations driven by relative motions of the SLPs, including the induction period of 100 s. (c) Spatial profiles of the upper SLP at varying strengths of non-locality. (d) Scaling of the SLP width on the strength of non-locality. The SLP width,  $A$ , was obtained by fitting a Gaussian distribution to profiles in (c) and taking standard deviation.

diminish and the shear rate to increase, starting a new oscillatory cycle.

Our model should have all the component required to capture this proposed phenomenology. In figure 3.3(a) we demonstrated that the stress-splitting instability will act to increase the total average stress in the domain. A similar effect is expected to occur in the spatial pattern-forming regime: the appearance of SLPs is accompanied by a large increase in the average stress acting on the upper plate. The stress control will react to formation of SLPs by decreasing the shear rate, with the extent of shear rate reduction being proportional to the additional stress produced by the formation of the SLP. In accordance with the definition of  $l_c$ , the decrease in shear rate will favour the non-local elements of the model, pushing the fields towards a homogeneous state and eroding the SLPs. The dissipation of SLPs will then in turn reduce total stress, potentially below the target stress set-point, resulting in an increase in shear rate. Increasing shear rate will drive the characteristic length scale from the homogeneous regime to a continuous spatial pattern regime initiating a new cycle.

This phenomenology is not observed in Fig. 3.4 likely due to the small amplitude of the oscillation in the shear rate, where a single cycle does not span a range of characteristic length scale wide enough to capture both the SLP-forming and homogeneous regimes. The underlying issue is the choice to artificially restrict the viscosity ratio in the rheology with the chosen parameters. In a real system, the viscosity ratio ( $H = \eta(f = 1)/\eta(f = 0)$ ) defined as the ratio of the completely frictional state and the frictionless state is observed to span up to three orders of magnitude. In the simulations so far, we have chosen to limit the viscosity ratio to a moderate value ( $H = 31.77$ ) for numerical purposes. Extending this parameter to a more realistic value should result in higher ‘excess’ stress production as a result of SLP formation, and higher range of shear rates during oscillations.

To test this, we carried out simulations with a modified flow curve shape (see Appendix Table A.4 for details). Due to the change in the rheology we also adjusted relevant dynamic parameters to maintain equivalent timescales. For a choice of input stress set-point of  $\Sigma_E = 10$ , we obtain nearly equivalent characteristic length scale ( $l_c = 0.0316h$ ) to the simulations in Fig.3.4, and we can exclude the inertia-driven



instability by setting  $\mu = -8.87 \times 10^{-3}$ . The main differences in the new rheology are a significantly increased viscosity ratio ( $H = 583.51$ ) and a reduced diffusive timescale ( $\omega = 0.79$ ).

The results of this high viscosity ratio (high- $H$ ) simulation (Fig. 3.6) are in stark contrast to the previous low- $H$  simulations. Both shear rate and stress oscillate in an aperiodic high-frequency mode, with a significantly increased amplitude of both signals. Despite the chaotic nature of the signals, a clear trend can be observed in which an increase in the shear rate induces a sharp increase in stress, followed by a sudden drop in the shear rate. Similarly, the fields no longer display persistent, well-defined SLPs attached to the boundaries (as seen for the low- $H$  case in Fig. 3.4), but rather the microstructural patterns consist of geometry-spanning structures, which nucleate and dissipate accordingly with oscillations in shear and stress. The highly aperiodic nature of the oscillations in this case is a result of rapid increases in the shear rate during the SLP dissipation phase. As the plate accelerates, a thin layer of high shear rate forms near the upper wall resulting in a microstructure nucleation and propagation in pulses from the top to the bottom of the geometry. Comparing these results to the experimental dynamics in [90], it is clear that the simulated dynamics do not display a clean distinction between a pattern-forming and homogeneous regimes such as observed experimentally. To more closely reproduce the experimental observations, we increase the inertia of the system by setting  $k_p = 0.01$ . Increasing the inertial timescale by two orders of magnitude should ensure ample time for microstructure dissipation. Note that now  $\mu > 0$  and we admit the possibility of a boundary-driven instability as in Section 3.3.1.

Figure 3.6 shows a comparison between low system inertia (a,c,d) and high inertia (b,d,f) stress and shear rate oscillations for three set-point stresses. In both high and low inertia cases, the signal retains significant aperiodic features and a comparable range of shear rate oscillations, but the pattern of increasing shear rate inducing a stress spike becomes even clearer for high inertia (Figure 3.6 (b,d,f)). Due to the slow action of the stress control scheme, the microstructure is allowed to form more extensive SLPs resulting in significantly higher and sharper increases in stress. In the same vein, oscillations in shear rate proceed by qualitatively regular (but

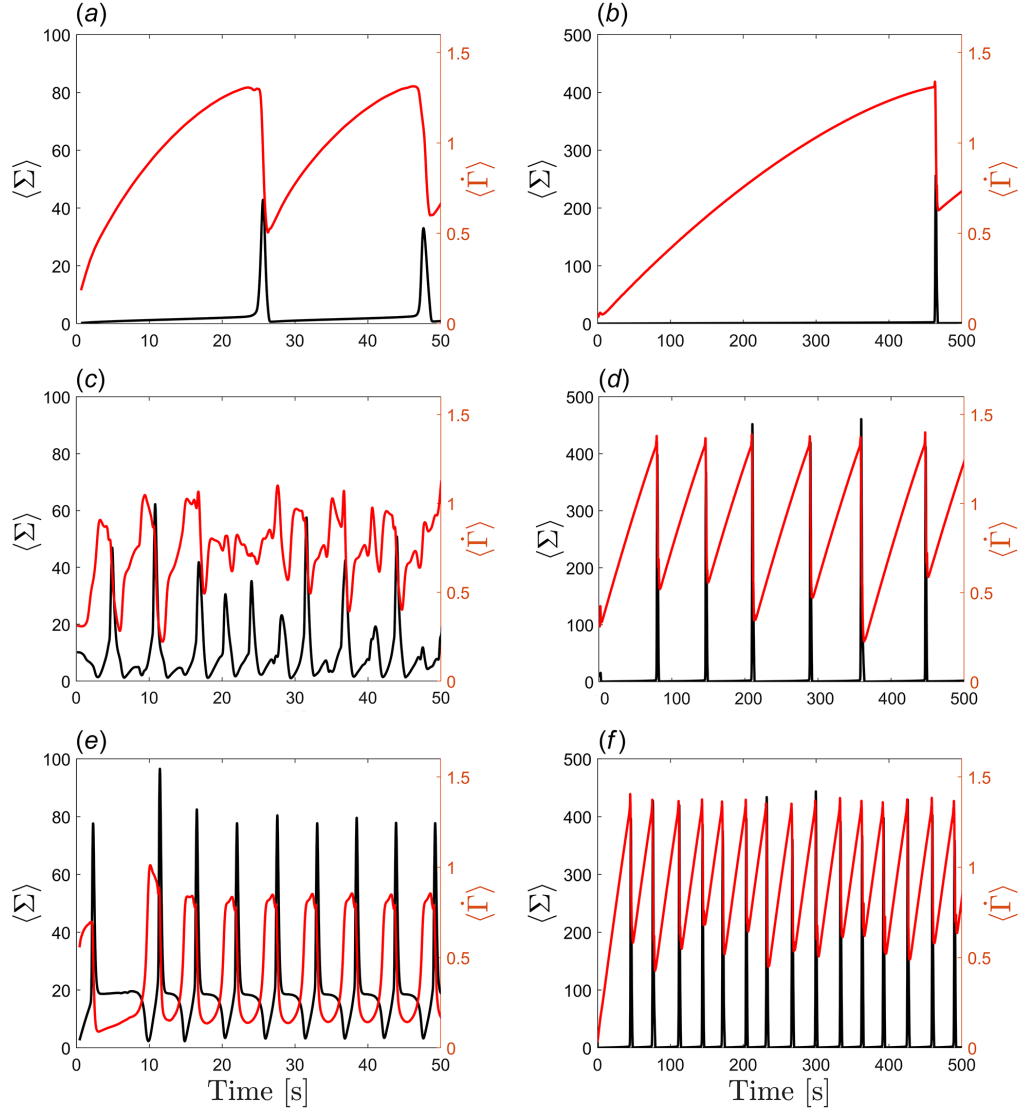


Figure 3.6: Normalised stress (black) and shear rate (red) signals with the modified rheology for (left column)  $k_p = 1$  and (right column)  $k_p = 0.01$ . Solutions for three different stress set-point values shown for both cases: (a,b)  $\Sigma_E = 3$ , (c,d)  $\Sigma_E = 10$ , and (e,f)  $\Sigma_E = 20$ .  $k_p$  represents the rheometer inertial response, with high values indicating low inertia. All three stresses applied in the range of negative gradients of the flow curve. For full set of parameters see Table A.4.

quantitatively aperiodic) slow increases in shear, followed by sharp decreases in shear rate due to massive spikes in stress. This result shows remarkable congruence with the oscillatory patterns reported for a stress-controlled system ( Rathee et al. [90]), where the oscillations were accompanied by the formation and disappearance of high-stress events acting on the lower plate. Microstructural fields now feature clear separation between regimes, with the existence of spatial patterns confined to short periods of time associated with spikes in stress; periods of increasing shear rate (and low stress) are associated with entirely homogeneous fields of microstructure. Typical fields of viscosity during a microstructure nucleation and dissipation cycle are shown in Fig. 3.7 for a simple shear in a wide geometry with  $l = 15h$ . No clear structures isolated to the boundaries can be observed. The microstructure spans the entire width of the gap with no clear alignment with either the extensional or compressive axes. Further simulations with an extended geometry ( $l = 15h$ ) were carried out to test the robustness of this phenomenology, with similar patterns being observed, i.e. the observed patterns of microstructure displayed in Fig. 3.7 are independent of system width size. Further simulations with double resolution ( $N = 100$ ) for  $l = 3h$  yielded close agreement with the results obtained at  $N = 50$ .

### 3.3.5 Fluid Inertia

In Figure 3.6, we present simulations for the depth averaged Reynolds number  $0.015 < Re < 8.1$ , with the range corresponding to the span of the oscillations. In cases of high system inertia ( $k_p = 0.01$ ), slow dynamics of wall velocity dominate resulting in clear linear velocity profiles throughout the oscillations, with no noticeable effects of fluid inertia. However, in the case of low system inertia ( $k_p = 1$ ), the effects of fluid inertia becomes apparent with the high stress regions initiating near the upper wall and propagating in short bursts, accompanied with consistently non-linear velocity profiles. To investigate the influence of fluid inertia on our results, we repeated both low and high system inertia simulations in the range  $0.0002 < Re < 0.13$  (see Appendix Table A.5). In case of high system inertia, reductions in fluid inertia yielded little difference, with qualitatively identical phenomenology. On the other

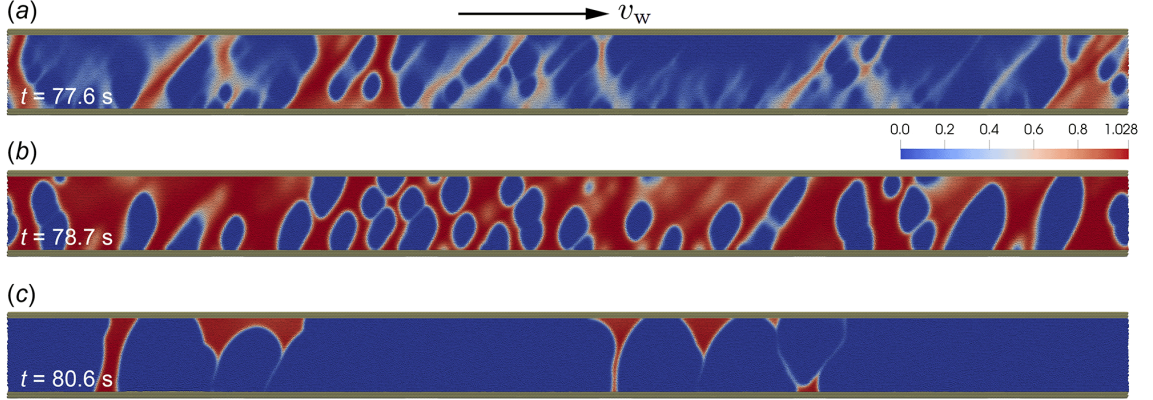


Figure 3.7: Visualisation of the viscosity field for a modified high-viscosity ratio rheology with high system inertia ( $k_p = 0.01$ ). Three subsequent time steps of nucleation (a,b) and dissipation (c) of high-viscosity structures.

hand, the oscillations in the low system inertia case differ significantly. Microstructure no longer propagates in bursts, rather semi-stable bands are formed. These bands propagate in the flow direction and occasionally interact with each other or the domain boundaries to undergo rearrangement. This results in signals where the microstructure rearrangements drive aperiodic fluctuations in stress and shear rate. The resulting signals have significantly lower relative amplitude of the oscillations (note that  $\mu < 0$  for both high and low fluids inertia).

Varying the stress set-point ( $\Sigma_E$ ) revealed a significant positive correlation between applied stress and the frequency of oscillations (Fig.3.6(b,d,f)), a feature reported in the experimental work Rathee et al. [90] - with no substantial alterations to the oscillation pattern in case of high inertia, but clear progression from near-periodic (Fig.3.6(a)) to strongly chaotic (Fig.3.6(c)) back to near-periodic solutions (Fig.3.6(e)) in the case of low inertia.

### 3.4 Conclusion

We have presented the application of an SPH scalar DST continuum model to the problem of instabilities in simple shear. We checked the accuracy of the model using a previously reported (instrument) inertia instability mechanism and found excellent agreement with the relevant stability properties. Validation of our model at the extreme of dominant locality compared to the model of Richards et al. [76] resulted in accurate predictions of both bifurcation points and limit cycle sizes in simulations, across a range of stress set points that span the entire flow curve, for two different gap height geometries.

To overcome shortcomings of an entirely homogeneous view of the instability, we considered a spatial instability in the form of stress-splitting. We demonstrated that such an instability is unique for the DST regime and documented its origin in local contributions to the commonly used microstructural evolution equation. Although stress splitting reliably produced inhomogeneous flow fields in the region of negative flow-curve gradients, it also yielded nondifferentiable stress and microstructure fields. Inclusion of non-locality allowed formation of continuous spatial patterns in microstructure. The form of non-locality in the present work was based on the formulation proposed by [123], but the analysis is expected to be general enough to anticipate alternate inclusions of non-locality. For example, particle migration as per suspension balance models should fulfil similar stress-diffusive role, with the added benefit of producing compaction fronts. With intermediate non-locality in the model, the obtained fields of microstructure showed formation of high viscosity phases - or solid-like phases (SLPs) - near the solid geometry boundaries, connected by a band material in a highly frictional state. The simulated DST-rheology in this case was characterised by a relatively low viscosity contrast which severely limited the range of the amplitude of the shear rate oscillations. This produced long-lived SLPs, more akin to the experimentally observed SLPs for shear rate controlled systems [90].

Simulations with high viscosity contrast (similar to realistic DST fluids) were able to capture the oscillatory phenomenology observed in the BSM measurements

of Rathee et al. [90], along with commonly reported aperiodic solutions (Hermes et al. [8]). Here, aperiodicity was found to be driven by the nucleation and dissipation of the microstructural patterns within the geometry, which were broadly similar but different in detail each cycle. The role of inertia was probed, and while it did not appear to have a determinative role in the presence of instabilities in the range of parameters used in this work, it had a significant influence on the oscillatory patterns. It is noteworthy that this suggests that measurements of identical materials should have significantly different patterns based on the parameters such as the inertia of the used geometry or the rheometer itself. Across the range of input stresses in the entire multivariate region of the flow curve, high inertia simulations maintained their near-periodic (but still strictly aperiodic) oscillation patterns with significant increases in frequency as stress increased. In the case of low inertia, high-stress events increase in frequency, but now the oscillatory pattern transitions from near-periodic to chaotic and back to near-periodic oscillations with increasing stress.

The primary limitation of our implementation is the lack of vorticity direction. Much of the instabilities in DST have an aspect along the vorticity direction, both in experiments [86; 91] and in simulations [58]. The inclusion of both gradient and vorticity instabilities is likely a key next step in future work toward a complete picture of rheochaos. In addition, the transition away from scalar microstructure representation toward tensorial microstructure orientation implementations could pose a significant advantage, allowing for distinguishing compressive and extensional shear effects in formation and destruction of the microstructure [137].

As a last remark, it should be noted that the microscopic DEM-based method with explicit solvent model and resolved hydrodynamics at a particle level [?] would allow us to describe the problem of heterogeneous flows. However, in order to reach the macroscopic scales of flow instabilities (due to scale separation), a prohibitively large number of degrees of freedom would be needed for these DNS simulations. In the present approach, we are proposing a continuum-based microstructural model allowing to reach larger scale and address the possibility of rheochaos.

# Chapter 4

## Instabilities in Complex Flows

### 4.1 Motivation

Having documented the stability properties of our model in simple shear, we now turn to more complex flow geometries. While in our simulations we have the benefit of being able to access the detail of the flow fields, in experimental works more indirect measurements are required. In the following sections, our aim is to bridge the gap between our simulation results and the experimentally observed phenomenology in simple shear and Poiseuille flow.

### 4.2 Simple Shear

We begin by revisiting simple shear. In the previous chapter, we have shown that our model is capable of reproducing chaotic oscillations under constant imposed stress. Those simulations effectively correspond to typical creep tests in which constant stress is applied to the sample. However, experimental investigators are often interested in measuring a flow curve for the material, which captures the relationship between shear stress and shear rate. Often such measured flow curves display complicated behaviour (Fig.4.1) which does not correspond to the typical 'S'-shape predicted by the WC model [8; 129; 6; 60; 57; 138]. Instead, experimental mea-

measurements tend to have good agreement along the frictionless branch, then deviate around the multi-valued region. The initial deviation is often characterised by a sudden backward shift (reduction) in the measured shear rate, after which the measurement continues to climb vertically upward (approximately constant shear rate) with increasing applied stress. The upward climb is characterised by significant noise in the measured shear rate, which is larger for higher volume fractions [8]. Finally, the measured curves never return to a stable mode even with high applied stresses ( $\Sigma_E \approx 100$ ) [8].

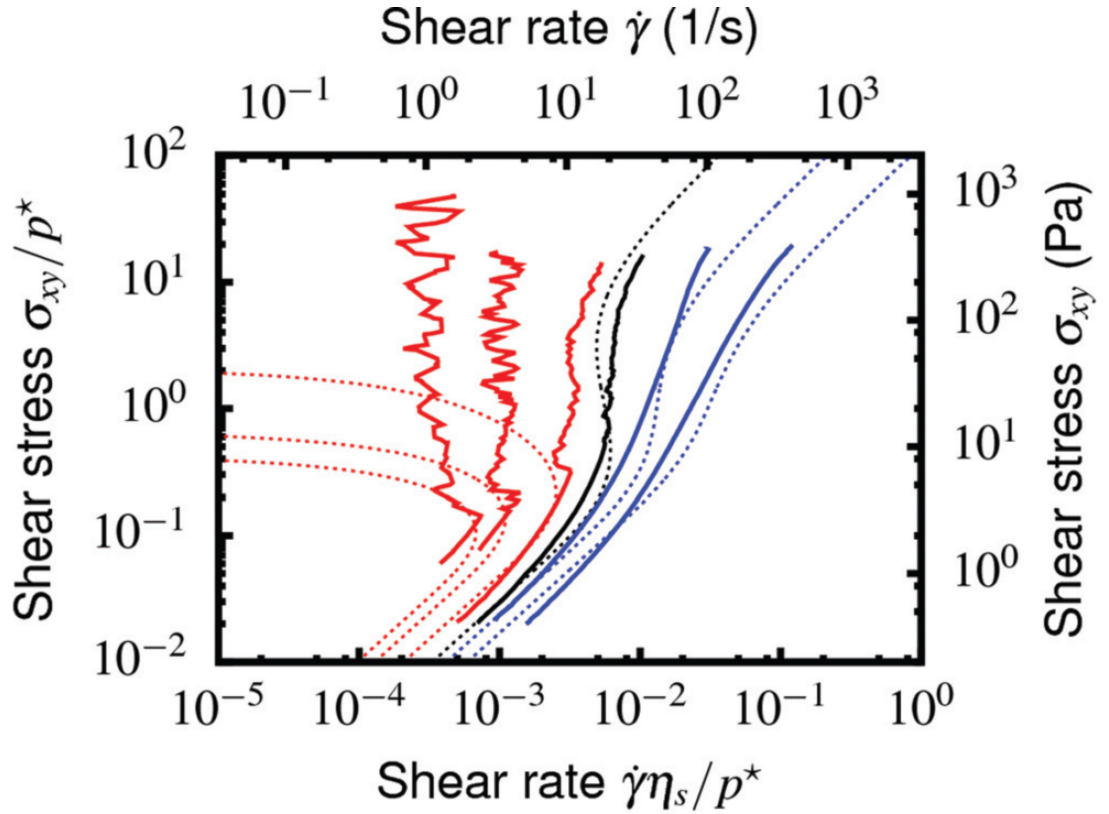


Figure 4.1: An example of typical flow curves obtained in simple shear of DST fluids. In this case, parallel plates were used to probe various mass fractions of corn starch. From right to left (blue to red) solid mass fractions of 0.45, 0.46, 0.465, 0.47, 0.50, and 0.52. Image source: Hermes et al. [8]



To understand how our model relates to the experimental phenomenology, we must first discuss how the flow curves are constructed from the experimental measurements. In constant applied stress experiments, the rheometer applies a constant torque ( $M$ ) to the rod attached to the geometry. For steady state, the applied torque must be balanced by the shear stress of the fluid acting on the surface of the geometry, thus the shear stress can be calculated  $\sigma = 2M/(\pi R^3)$ , where  $R$  is the radius of the plate. During the experiment, the angular velocity  $\Omega$  of the rotating plate (in the parallel plate setup) is measured, allowing the calculation of the shear rate at  $r = R$  ( $\dot{\gamma} = R\Omega/h$ ), where  $h$  is the height of the gap. For each applied torque, a set equilibration time ( $t_{\text{eq}}$ ) is allowed to reach steady state, after which the shear rate signal is averaged over an averaging window ( $t_{\text{avg}}$ ).

The first thing to note is that the measured shear rate is the global (or average) shear rate, which can be different from the local shear rate. The second issue is that in rheochaotic measurements the assumption of steady state required for shear stress measurement is clearly not true. To conform to the experimental framework of measurements, we will use the stress control simulations with spatially averaged shear rate as the measured signal (the spatially averaged and wall shear rate are essentially identical in the simulations). The measured signal will receive a constant equilibration time ( $t_{\text{eq}} = 20$  s) and averaging time (depending on the inertia). The exception is the measurements for low applied stresses, where no oscillations are present, but instead a long time is required to reach steady state; here the averaging time is extended since we are not interested in the inertial period in absence of oscillations. Instead of reporting the actual measured stress, we will report the applied stress set point  $\Sigma_E$ .

The rheology used in the simulations is identical to the rheology used in the rheochaotic oscillations reported in the previous chapter. Starting with results for  $k_p = 0.01$  (high system inertia), a constructed flow curve is plotted in Fig. 4.2(a). At low applied stress, the resulting flow curve matches the frictionless branch well. Once the multi-valued region ( $\frac{d\dot{\gamma}}{d\Sigma} < 0$ ) is reached, the previously discussed instability sets in, leading to large oscillations (approximately an order of magnitude) in the measured shear rate. At the same time, the mean measured shear rate falls to a

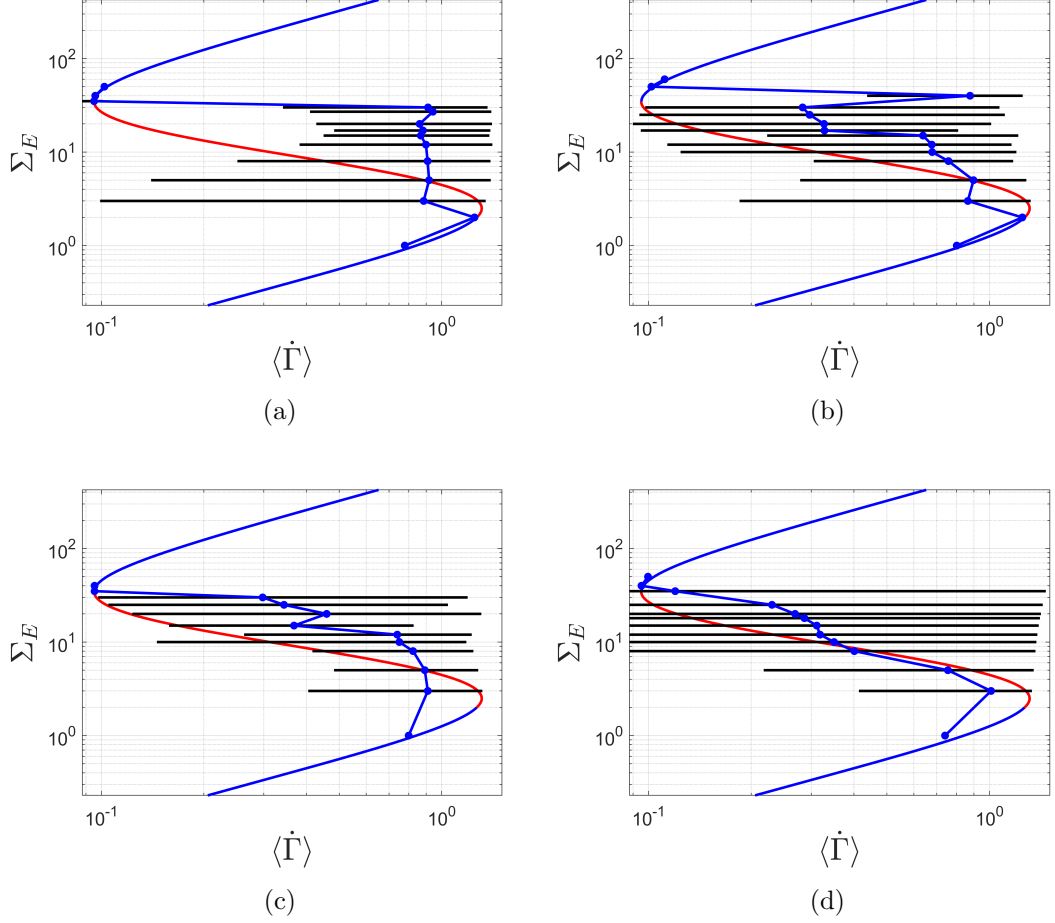


Figure 4.2: Constructed flow curves for (a)  $k_p = 0.01$  ( $t_i = 633$  s), (b)  $k_p = 1$  ( $t_i = 6.33$  s), (c)  $k_p = 10$  ( $t_i = 0.633$  s), and  $k_p = 0.01$  with reduced domain height  $h = 0.004$  ( $t_i = 253$  s). Rheology consists of  $\phi_m = 0.56$ ,  $\phi_0 = 10$ ,  $\phi = 0.54$ ,  $\eta_s = 0.00158$ , and  $\sigma^* = 0.0005$ . Black bars indicate the maxima and minima of measured shear rate oscillations, ignoring any initial inertial transient. Inertial timescale calculated as  $t_i = h/k_p\eta_s$ . Gap height in (a)-(c) is kept constant at  $h = 0.01$ .

value below the prediction of the WC model, resulting in a backward kink. Further increases in applied stress alter the amplitude of the signal, but the mean measured shear rate remains nearly constant, leading to a vertical climb in the flow curve that spans the entire multi-valued range of the WC model. Once the applied stress reaches the frictional branch, the oscillations vanish very suddenly, and the measurements again follow the WC model.

The present results show remarkable agreement with some of the key features of the experimentally measured flow curves. Our model predicts the initial drop in the shear rate at the onset of instabilities and the vertical climb that does not capture the S-shape. Our model also predicts a sudden onset of stability at sufficiently high applied stresses, which is not seen in the experiments. In the context of our model, the condition for instability is

$$\left( \frac{d\dot{\Gamma}}{d\Sigma} \right) \bigg|_{\Sigma_E} < 0, \quad (4.1)$$

where in our simulation, the applied stress at which the gradient is evaluated is a single value. For a parallel plate, the applied torque results in a distribution of applied steady-state stress, where the maximum stress is applied at the rim. This means that as the torque increases, the instability region (where the condition 4.1 is satisfied) will grow from the rim towards the centre at the onset of instability. Eventually, a sufficiently high applied torque will induce formation of a stable area growing from the rim accompanied by the shrinkage of the unstable area. Since the stress at the centre of the geometry vanishes, even at high applied torques, there will be a part of the geometry, near but not exactly in the centre, occupied by fluid experiencing applied stress that satisfies the instability condition, which could explain the persistence of instabilities. In our model, such a mechanism is not possible, since we do not simulate the radial dimension, resulting in a sudden onset of stability once the frictional branch is reached. The proposed explanation is expected to be true for parallel plates; however, measurements in Couette flows do not have a stress distribution in the vorticity direction, yet they yield persistent instabilities. A simpler explanation could be that experimental investigations do not

apply sufficiently high stresses to reach the stable branch; however, further study in 3D flow would be required to conclude as to what is the source of the discrepancy between our model and the experiments.

Another interesting question in experiments is that of the system inertia ( $t_i = h/k_p\eta_s$ ) and its influence on the results. In experiments, the inertial timescale can be varied by a multitude of factors, including the diameter of the plate, the material of the plate, the rheometer model used, the viscosity of the solvent, and the height of the gap. Our previous results showed a clear effect of inertia on the oscillatory pattern of the shear rate signal; it would be of interest to know how inertia affects the construction of flow curves. We construct flow curves with decreased inertia (higher  $k_p$ ) and plot the results in Figure 4.2(b-c). The reduction in system inertia significantly altered the constructed flow curves in the multi-valued region. Instead of the upward vertical climb, clear 'S'-shaped bending and negative gradients can be discerned. This is in general in line with the experimental work of Hu et al. [139], where reducing gap size yielded strong measurements of the negative gradients in the flow curve. Hu et al. [139] ascribed the difference in the measured flow curve to the confinement effects; however, reducing the gap size would have both confinement and inertial effects.

To discern between the effects of inertia and confinement, we carry out another set of stress-controlled simulations at  $k_p = 0.01$  with a reduced gap height  $h/h_0 = 0.4$ , where  $h_0 = 0.01$  is the original gap height in the rest of the simulations. We keep the numerical resolution constant by reducing the number of particles in the gradient direction to 20. The resulting constructed flow curve (Fig.4.2(d)) shows a dramatic difference compared to the base gap height simulation (Fig.4.2(a)). The confined results reproduce negative gradients across the entire multi-valued regime and display much stronger agreement to the WC model than any of the low-inertia simulations. In the confinement simulation, we reduced the inertial timescale by a factor of 0.4, while in the low-inertia simulations, we reduced the same timescales by a factor of at least 0.01. However, despite many more orders of magnitude changes in  $t_i$ , low-inertia simulations produced an effect significantly weaker than the confinement simulations. Thus, we can conclude that confinement has an effect that is much

stronger and distinct from simply lowering the system inertia.

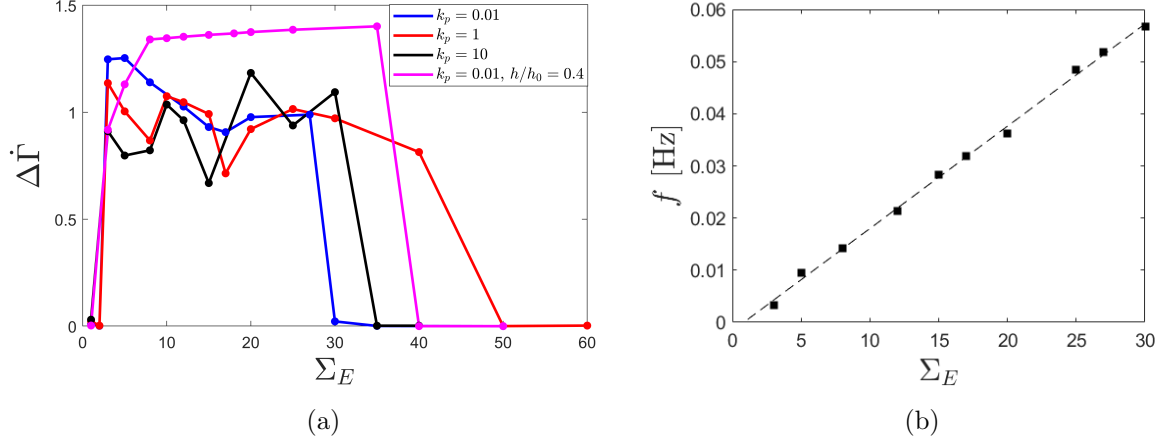


Figure 4.3: (a) Plot of oscillation amplitude at varying applied stresses for three different amount of system inertia. (b) Oscillation frequency as a function of applied stress for  $k_p = 0.01$ .

Next, we look at the property of oscillations reported in our simulations. In Figure 4.2, we report error bars in the shear rate corresponding to the minimum and maximum shear rates measured during the oscillation (ignoring the early inertial period). We plot the measured amplitude for all three system inertia flow curves in Figure 4.3(a). At the onset of instability, the amplitude appears to have inertia dependence, with higher inertia simulations attaining higher amplitudes. Beyond the onset, the trend is difficult to discern. The highest inertia simulations appear to decrease in amplitude with increasing applied stress, while the other two inertia values have a noisy response to increasing stress. The confinement simulations present a clear trend with little noise and progression in amplitude that is reminiscent of the Richards instability under homogeneous conditions. This is interesting since all the present simulations (except  $k_p = 10$ ) are unstable as per Richards analysis [76], with  $\mu > 0$ , yet they display very different stability properties based on confinement. In the confined geometry, the microstructure does not form distinct SLPs, or rather the SLPs occupy the entire domain. This results in a scenario where spatial heterogene-

ity is present only in the formation or dissipation transients, not when the structure is fully formed. For all simulations, the applied stress has an effect on the frequency of the oscillations. In the simulations presented in Figure 4.2, for  $k_p = 1$  and  $k_p = 10$ , this effect is difficult to quantify since the signals are very clearly aperiodic (chaotic), but for  $k_p = 0.01$  the signals are regular enough (yet still strictly speaking aperiodic) to allow crude measurements of frequency by simply counting peaks. Interestingly, the measured frequency appears to have a strong linear relationship with applied stress, an observation made in the experimental work of Hermes et al. [8].

Finally, we remark on the classification of signal patterns. Throughout this work, we have used terms 'periodic', 'aperiodic', and 'chaotic' in a strict and narrow sense consistent with the mathematical approach to nonlinear dynamics. For example, a signal which appears regular in frequency, but in each apparent cycle it attains a significantly different maximum or minimum value would be classified as aperiodic or chaotic interchangeably, as the signal never really repeats. Hermes et al. [8] use the terms 'periodic', 'intermittent', and 'chaotic' in a different way. They do not require strict adherence to repeating signal for periodicity; rather, they use these terms to classify the extent of signal 'regularity'. Both approaches are valid, but carry different meanings. For the sake of comparison, we adopt the meanings of these terms consistent with Hermes et al. [8] for the rest of this discussion (and only for this discussion). Having addressed the linguistic challenges, we plot the shear rate signals for increasing applied stresses in Figure 4.4. At  $\Sigma_E = 3$  (Fig. 4.4(a)) the signal is clearly regular and 'periodic'. Increasing stress ( $\Sigma_E = 5$ ) introduces a degree of irregularity (Fig. 4.4(b)), but this signal is still 'periodic'. Eventually ( $\Sigma_E = 12$ ) the signal loses much of its regularity (Fig. 4.4(c)) and would best correspond to an 'intermittent' signal. Increasing stress further ( $\Sigma_E = 20$ ), another transition occurs, this time the signal regains its regularity and returns to a periodic mode. For any of the stresses above this point, the signal will remain periodic until an eventual transition to stability. This pattern is robust for all values of  $k_p$ , although the exact transition values are different, with high-stress periodicity appearing at lower values for higher values of  $k_p$ .

Our simulations appear to reproduce the stable to periodic to intermittent transi-

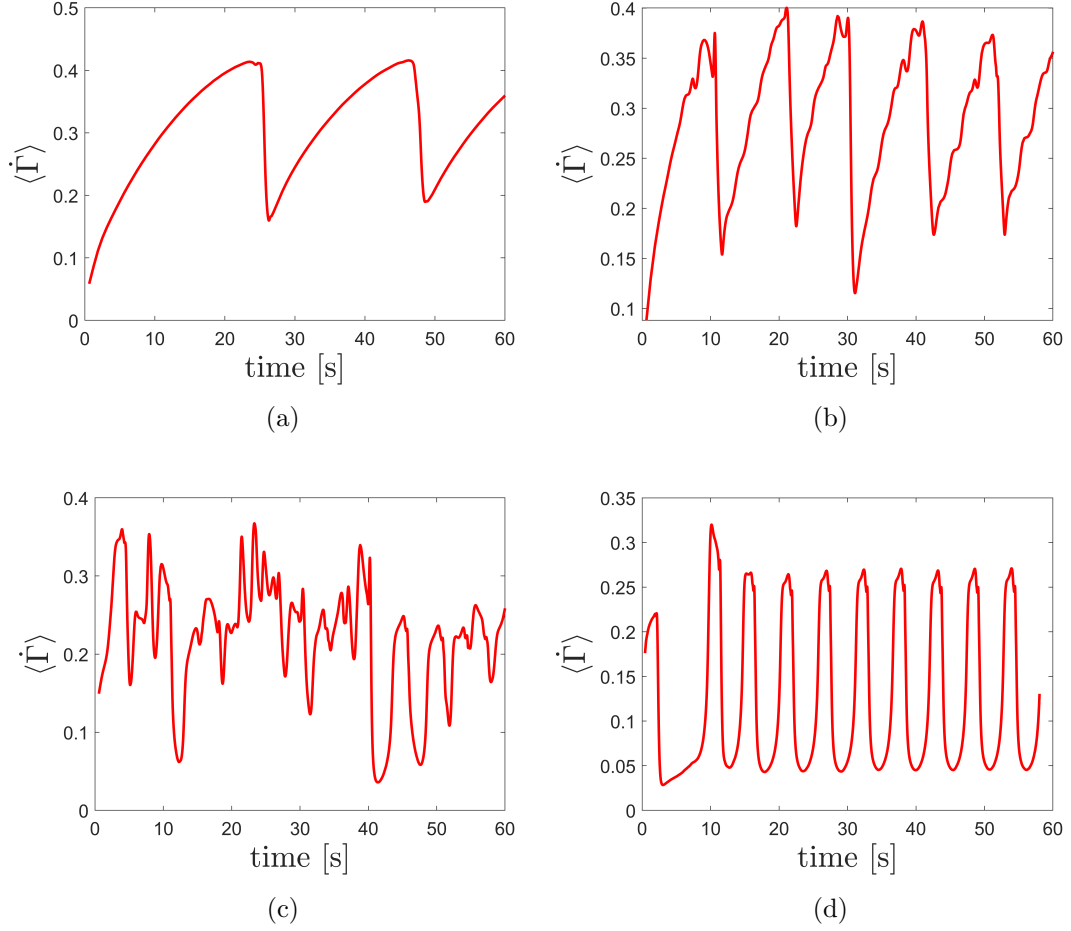


Figure 4.4: Progression of signals from (a) periodicity ( $\Sigma_E = 3$ ) to (b) transitional periodic pattern ( $\Sigma_E = 5$ ) to (c) an intermittent signal ( $\Sigma_E = 20$ ) and (d) return to periodicity ( $\Sigma_E = 20$ ), for  $k_p = 1$ ,  $h = 0.01$ ,  $\alpha = 2 \cdot 10^{-7}$ , and  $t_i = 633$  s.

tion reported by Hermes et al. [8], but fail to reproduce the 'chaotic' pattern at high stress. It is likely not incidental that this failure coincides with the previous discrepancy in the persistence of instabilities at high stress. Whether this is a difference in the kind of instability mechanism present at high stresses that our simulations lack, or if it is a question of tuning in dynamic parameters is not clear at this stage and would require further work.

### 4.3 Poiseuille Flow

The key work on DST instabilities in Poiseuille flow is the recent work of Bougouin et al. [60]. Their setup consisted of a circular pipe filled with corn starch suspension, inclined at an angle ( $\theta$ ) to facilitate gravity-driven flow. Their work revealed a new mode of instability in which the base flow (laminar phase) is disturbed by the formation of a superdissipative frictional structure at the pipe entrance. This structure propagates against the flow direction, with a velocity approximately equal to the mean suspension flow velocity and the length scale set by the diameter of the pipe. The transition between stable and unstable modes of flow occurs when the wall stress ( $\sigma_b$ ) is approximately equal to the minimum stress required to achieve negative gradients of the flow curve ( $\sigma_c$ ). Note that this is not the characteristic stress scale  $\sigma^*$ . At the onset of instability, Bougouin et al. [60] report a sudden decrease in volumetric flow rate reminiscent of faster-is-slower DST behaviour and a region of localised high wall stress associated with the formed structure.

To obtain the first approximation to the experimental pipe setup, we simulate the Poiseuille flow in a 2D channel with periodic boundary condition. The material parameters for the fluid are identical to the previous section on simple shear. We conduct the investigation by setting the inclination angle to  $90^\circ$  and changing the wall stress by adjusting the gravitational driving force ( $g$ )

$$\sigma_b = \rho g R \sin \theta, \quad (4.2)$$

where  $\rho$  is the suspension density and  $R$  is half the diameter of the channel.

Our results show stable base flow at low values of wall stress, with a sudden onset of instability at sufficiently high ( $\sigma_b/\sigma_c \approx 1.4$ ) applied wall force. The instability begins with the formation of small frictional structures localised near the walls (Fig.4.5(a)). At wall stresses near the onset of the instability, the structures are small enough to allow for base flow most of the time. However, the base flow has a strip of high shear rate (as predicted by the solution to the previously derived base flow equation (2.51)), which can occasionally become disturbed by the encroaching structures. When the region of high shear starts growing inward toward



the channel centreline, it facilitates the formation of the microstructure because of the dominant local contributions to the microstructure evolution equation. Thus, the initial deformation of the shear band causes an inward elongation of the initial structure, which, in turn, impinges on the base flow by creating a flow-concentrating obstacle. The flow concentration in a narrower region of the channel results in a locally increased shear rate, which in turn induces further microstructure growth. This positive feedback loop continues until the frictional structure spans the entire width of the channel (Fig.4.5(b)), effectively restricting flow. The drop in shear rate favours the nonlocal components, which results in dissipation of the microstructure across the channel (Fig.4.5(c)) and return to base flow after a short inertial period.

The frequency of these flow-restricting events increases drastically with an increase in the applied wall stress (Fig.4.6), resulting in an intermittent flow that rapidly becomes chaotic. We plot the spatial and temporal average shear rate as a function of wall stress in Figure 4.7(a). The results show a linear flow response at small applied stresses ( $\sigma_b/\sigma_c < 1$ ) with noticeable but continuous effects of shear thickening near  $\sigma_b/\sigma_c \approx 1$ . In contrast, at  $\sigma_b/\sigma_c \approx 1.4$ , a discontinuous decrease in the measured shear rate marks the transition from stable to unstable mode of flow. After this point, further increases in the applied stress further reduce the flow rate. This apparent faster-is-slower behaviour matches the experimental findings of Bougouin et al. [60]. Next, we investigate the trend of the average stress in the channel; we measure the average total stress in the domain as a function of the applied wall stress. The average measured stress follows the applied wall stress linearly (Fig.4.7(b)) until  $\sigma_b/\sigma_c \approx 1.4$ , where a bifurcation occurs. In this new regime, the measured stress drastically increases before it settles into a new linear relationship with the high applied wall stress. This picture is similar to the progression of the measured wall stress based on the pressure drop across the frictional structure in experiments [60].

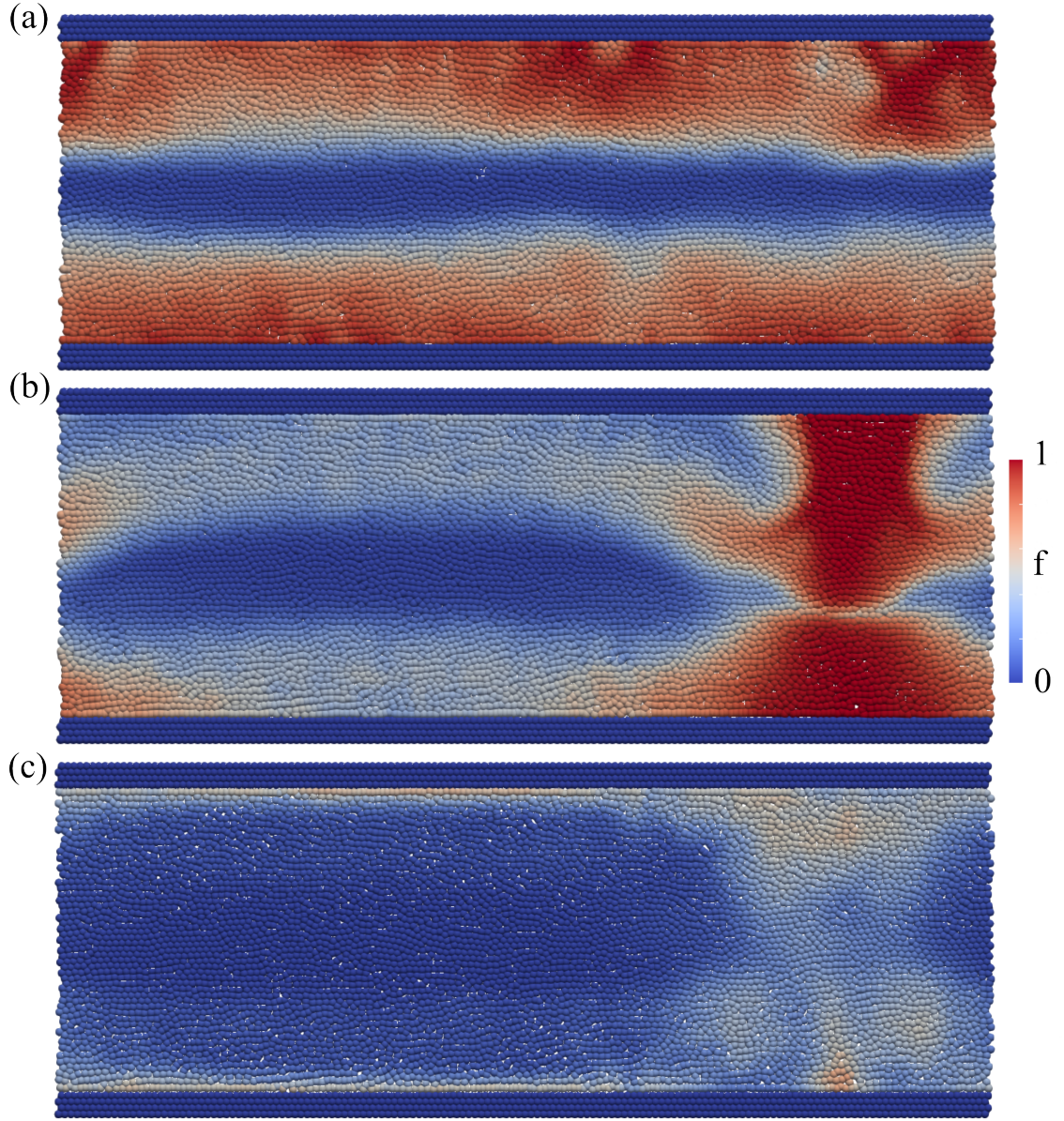


Figure 4.5: Progression of an instability cycle in Poiseuille flow for  $\sigma_b/\sigma_c = 1.49$ . (a) Formation of structures near walls disturbs the base flow towards the channel centreline, (b) local positive feedback loop facilitates growth of width-spanning frictional structure and flow restriction, (c) dominant nonlocal forces dissipate frictional contacts in the blocked channel and return the domain to base flow.

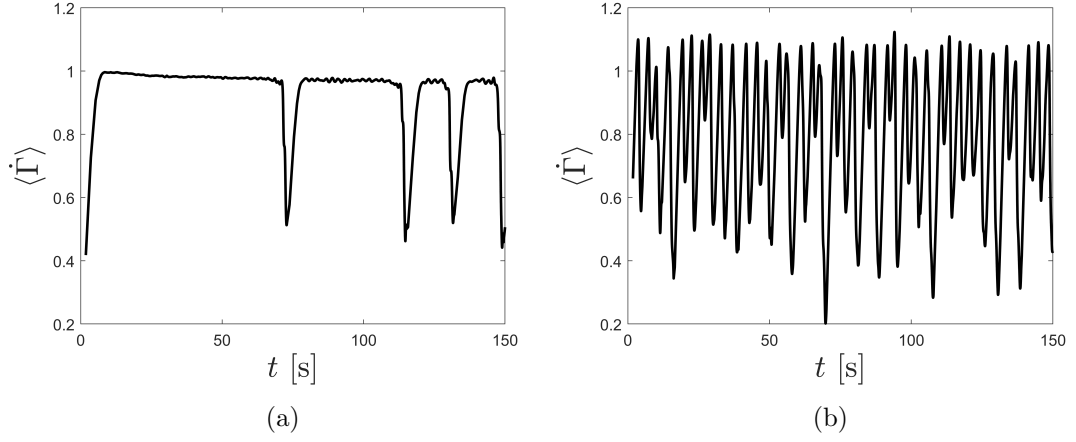


Figure 4.6: Typical shear rate signals (a) near the onset ( $\sigma_b/\sigma_c = 1.49$ ) and (b) at high wall stress ( $\sigma_b/\sigma_c = 2.38$ )

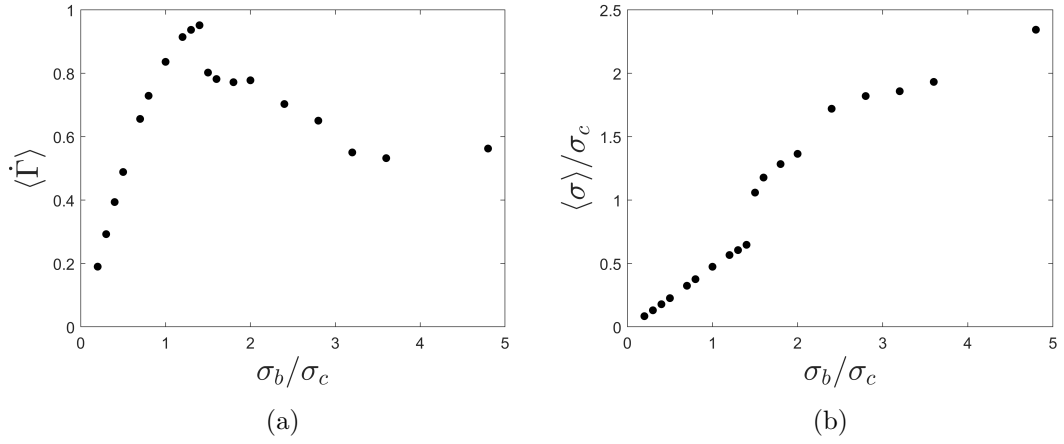


Figure 4.7: (a) Average shear rate and (b) stress as a function of applied wall stress.

## 4.4 Conclusion

In this section, we consolidated the understanding of rheochaos developed in the previous chapter and applied it to experimentally relevant simple shear and Poiseuille flows. We considered the practical elements of the flow curve construction and applied a measurement procedure equivalent to the experimental technique and applied it to our stress-controlled simulations, with known rheochaotic dynamics. The construction of flow curves from the oscillatory signals resulted in a pattern commonly observed in the experiments, with a sudden decrease in the shear rate at the onset of the multi-valued region and a subsequent upward climb at a near-constant shear rate. Our model reproduced the reported transition from stable to periodic to intermittent signals with increasing applied stress; however, it failed to produce the 'chaotic' pattern reported at high stresses. Instead, our model predicts the return to periodicity before reaching stability on the frictional curve. A plausible mechanism for the discrepancy in the radial stress distribution in parallel plates was identified, but it is not clear that the same mechanism would explain the experimental results obtained in the Couette flows. This difference between the experiments and the present model highlights the need to move into more realistic geometry domains, which would consist of simulations extending into the vorticity direction along with the fine detail of specific rheometer flow geometries. The effect of inertia and confinement was investigated in the context of flow curve measurements. Reducing inertia and increasing confinement allowed for measurements of negative gradients in the flow curves (rather than the upward climb); however, the effect of confinement was found to be separate, unique, and dominant relative to the inertial effects, allowing for near exact agreement with the WC model.

Simulations of the Poiseuille flow revealed a new intermittent flow regime, marked by the formation of a flow-restricting frictional structure that spans the entire width of the channel. The mechanism of this instability was documented in the context of local and non-local action on the previously presented base flow solution. Across both stable and unstable regimes, our simulations showed a phenomenology consistent

with the experiment work of Bougouin et al. [60], including sudden decrease in flow rate at the onset, accompanied by the formation of structures carrying excess stress. In contrast to the experiments, our model did not predict the upstream movement of the developed frictional structure. A potential limitation is the use of periodic boundary conditions in our simulations, which is not well suited to a problem of the experimental pipe, where the symmetry is broken along the flow direction. Furthermore, our model does not feature particle migration, while Bougouin et al. [60] proposed dilatancy as a key mechanism of upstream propagation.

In summary, our 2D simulations employing the scalar model serve as a good first approximation to realistic complex flows of DST materials, despite the limited nature of our model. The key features that should be considered in future work include moving to a 3D computational domain to include vorticity effects, moving away from the use of periodic boundary condition to allow for symmetry breaking in the flow direction, and inclusion of particle migration effects.

# Chapter 5

## Material Characterisation

### 5.1 Ageing

For the purpose of experimental investigation, corn starch suspended in a mixture of water and glycerol was chosen as a DST model system. Corn starch is relatively inexpensive, readily available, has been used in significant works on DST [8; 48; 133; 7; 49], and is completely safe to handle. These properties make it ideal for experimental setups that require large volumes of suspension, but corn starch also has a number of stability issues in suspensions. In the course of handling corn starch suspensions, it became apparent that any samples left for an extended period of time (multiple hours) became more viscous and more shear-thickening until eventually completely jamming.

It is clear that before the desired experimental work can be performed, we must first consider the ageing nature of the suspensions. In general, we will assume that the ageing consists of an increase in the volume fraction, with the ageing rate affected only by the solvent viscosity such that the suspension with a given corn starch mass fraction ( $x_{cs}$ ) and glycerol-water mass fraction ( $x_g$ ) has identical properties for an identical ageing history. Unless otherwise stated, all results presented in this work will be given for a particular mass fraction, solvent ratio, and specific ageing time. The potential ageing mechanisms considered in this work are: sedimentation, pore

intrusion, evaporation, and particle swelling.

### 5.1.1 Sedimentation

The density of corn starch particles ( $\rho_{cs} = 1.62 \text{ g cm}^{-3}$ ) [140; 138] is larger than the solvent density ( $\rho_L$ ) meaning sedimentation will occur. The observed ageing process is almost certainly not caused by sedimentation, as ageing causes thickening throughout the sample, including the surface, which is entirely inconsistent with sedimentation. However, it would be beneficial to understand the sedimentation dynamics as it can affect rheological measurements and large-scale flow experiments. To assess the timescales associated with sedimentation we employ the Richardson-Zaki relationship for hindered settling [141] for  $Re < 0.2$

$$u = u_o(1 - \phi_v)^{4.65}, \quad (5.1)$$

where  $u$  is the settling velocity,  $\phi_v$  is the effective solid volume fraction, and  $u_o$  is the settling velocity for a single particle, given by

$$u_o = \frac{d^2(\rho_{cs} - \rho_L)g}{18\eta_s}, \quad (5.2)$$

where  $\eta_s$  is the solvent viscosity, determined by the solvent ratio. From this we can estimate that the time required for a suspension to sediment 1 cm for an effective volume fraction of 0.40 is approximately 25 min, 6 h, and 670 h, for pure water, 65% glycerol and pure glycerol, respectively. In most experiments, the three timescales would be appropriate as no single measurement should take more than 25 min and suspension can be resuspended between measurements, with the exception of rheometer measurements, where pure water would face significant sedimentation issues. Some works in literature address sedimentation by density matching the solvent with Cesium Chloride [138; 128], however, CsCl would significantly increase the costs associated with preparing large samples of corn starch and would have significant safety issues. Instead, we use 65% glycerol solvent ( $\rho_L = 1.17 \text{ g cm}^{-3}$  [142]), focus on resuspending the particles where appropriate, and monitoring effects of sedimentation in long-term rheological measurements.



### 5.1.2 Pore Intrusion

Corn starch particles are porous, and calculations of the volume fraction must account for it. Calculating volume fraction without accounting for the porous nature of corn starch would give us

$$\phi = \frac{m_{cs}/\rho_{cs}}{m_{cs}/\rho_{cs} + m_L/\rho_L}, \quad (5.3)$$

where  $m_{cs}$  and  $m_L$  are masses of mixed corn starch and solvent. In reality Eq.(5.3) underestimates the actual volume fraction, as some of the solvent will intrude into the porous particle structure and will be essentially excluded from the suspending volume. In addition, dry corn starch exposed to air has a tendency to absorb moisture from air, so in practice a fraction ( $\beta$ ) of measured corn starch mass will be due to the presence of water, meaning that the actual mass of cornstarch added is  $(1 - \beta)m_{cs}$  and additional  $\beta m_{cs}$  mass of water is added to the solvent. The resulting equations for the material volume fraction ( $\phi_m$ ) and the effective volume fraction ( $\phi_v$ ) [143] are

$$\phi_m = \frac{(1 - \beta)m_{cs}/\rho_{cs}}{(1 - \beta)m_{cs}/\rho_{cs} + m_L/\rho_L + \beta m_{cs}/\rho_w} \quad (5.4)$$

$$\phi_v = \frac{1}{1 - \psi} \phi_m, \quad (5.5)$$

where  $\rho_w$  is the density of water, and  $\psi$  is the porosity of corn starch particles.

Infiltration of fluid into pores will take some time, during which the volume fraction will increase from  $\phi_m$  to  $\phi_v$ , which could explain the apparent ageing of corn starch. The dynamics of this process can be estimated using Lucas-Washburn equation [144] for capillary flow

$$t = \frac{2\eta_s L^2}{\gamma r \cos(\theta)}, \quad (5.6)$$

which relates the time required for a fluid to invade distance  $L$  into the pore space, with wetting angle  $\theta$ . Here, the properties of the fluids are the viscosity ( $\eta_s$ ) and the surface tension coefficient ( $\gamma$ ), and the properties of the pores are the radius of the pores ( $r$ ) and the length of the pores ( $L$ ). Importantly, assuming constant



pore properties, increasing solvent viscosity would increase the intrusion time, which would explain why glycerol samples age slower than water-glycerol samples, making pore intrusion a feasible ageing mechanism.

### 5.1.3 Evaporation

Evaporation in the case of water-glycerol mixtures could reduce the amount of solvent and increase the effective volume fraction, and it is likely a contributing factor in experiments. It is not expected to be the main ageing mechanism as it would not explain the ageing in pure glycerol samples, where the hygroscopic nature of glycerol would inhibit evaporation and actually absorb moisture from the air. In addition, the ageing is not affected by covering the samples with parafilm to insulate the material from exposure to air. However, evaporation is expected to occur in experiments with water-glycerol mixtures. In rheometer measurements, evaporation can be excluded by adding a small amount of silicon oil around the rim of the parallel plates. In large-scale free surface experiments, the rheology of the sample should be monitored to detect potential changes owing to evaporation.

### 5.1.4 Swelling

Some authors reported swelling of cornstarch particles in the presence of solvent [8], which could explain the ageing process. This can be taken into account by measuring the particle size distribution at the beginning and end of the ageing process.

### 5.1.5 Ageing in Glycerol

A suspension of corn starch in 99.5% glycerol ( $\phi_v = 0.475 \pm 0.007$ ) was prepared by manually mixing corn starch in moderate increments. Suspending corn starch in solvent is tricky as it tends to form dry clumps which need to be identified and broken apart manually during the mixing process. Immediately after preparation, the sample was transferred to a cup geometry and its rheology was measured using vane geometry (AR G2, TA Instruments). The measurements consisted of a creep at

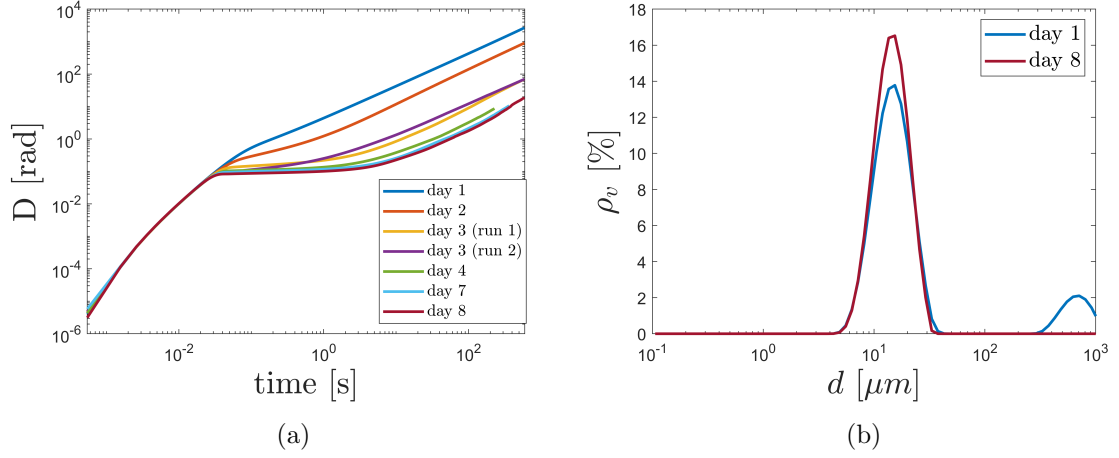


Figure 5.1: (a) Plots of displacement over time for the corn starch-glycerol suspension in a vane geometry over the duration of 8 days. (b) Volume density distribution of cornstarch on day 1 (red) and day 8 (blue). The second peak on day 1 at approximately  $d = 700 \mu\text{m}$  is due to the presence of air bubbles, which can sometimes affect the measurement. The same bubbles were seen on day 8, but by chance did not show up during the actual measurement.

constant torque ( $M = 6156.40 \mu\text{N m}$ ). After measurement, the sample was retained and covered with parafilm. The vane measurement was repeated six times for a duration of 8 days. In parallel, right after preparation and on the final day, the particle size distribution was measured using laser diffraction (Malvern Panalytical Mastersizer 3000).

Figure 5.1 shows the results of the ageing study. From the plot of vane displacement (Fig. 5.1(a)) we can see that on each subsequent day the displacement achieved over the duration of the creep decreases, indicating an increase in viscosity. The increase spans multiple orders of magnitude, but it is difficult to tie it to an exact increase in the volume fraction, as the applied stress here is above the characteristic onset stress scale for shear thickening, which means that changes in the volume fraction would have the two-fold effect of increasing viscosity via the Maron-Pierce [41]

type relationship and by altering the shear-thickening properties of the material [51].

We once again consider the possible ageing mechanisms previously discussed. Firstly, evaporation and sedimentation can likely be ruled out as both should be minimised by using glycerol solvent, along with resuspension mixing between measurements and covering the sample with parafilm during downtime. This leaves us with pore intrusion and swelling. Measurements of particle size distribution (Fig. 5.1(b)) reveal that there is no significant change in the size of corn starch particles after 8 days in suspension, leaving us with pore intrusion as the sole ageing mechanism. A complete study would be required to confirm whether the ageing time scale is consistent with pore intrusion, which falls well beyond the scope of this work. Instead, we adopted the approach widely used in the literature on DST using corn starch as the model system, where each sample is given an identical rest time before measurements, and the results are monitored for ageing processes. In addition, our results highlight the critical balance in the choice of solvent. If pore intrusion is indeed the main driving mechanism for ageing, then pure glycerol is clearly not a suitable solvent if we are interested in using fully saturated samples (and the nominal value of volume fraction will become important later on). Each sample would need to be prepared at least a week in advance, making the experimental investigation highly impractical. A mixture of glycerol and water is preferred as it would allow the sample to reach its effective volume fraction in a shorter period of time, ensuring that the actual volume fraction is consistent with the effective volume fraction reported. However, this has the drawback of reintroducing effects of evaporation and sedimentation, which must be taken into account during subsequent experimental procedures. In summary, our approach will be to use 65% glycerol mixture and assume that the 1 h ageing time is enough to approach full saturation.

## 5.2 Rheology

### 5.2.1 Slip

A corn starch suspension ( $\phi_v = 0.546 \pm 0.007$ ) was prepared by manually mixing corn starch with glycerol-water solvent ( $x_g = 0.50$ ). During mixing, dry corn starch clumps were identified and broken apart by using a crushing motion during mixing, trapping the clumps between the wall of the container and the mixing spoon. After preparation, the sample was allowed to rest for approximately 50 minutes with intermittent stirring and loaded into a parallel plate geometry (AR G2, TA Instruments), with gap height ( $h_{\text{gap}}$ ) of 1000  $\mu\text{m}$ . Once loaded, silicon oil ( $\eta = 9.71 \text{ mPa}\cdot\text{s}$ ) was carefully spread around the rim of the plates (3-5 drops) to insulate the sample from air. The sample was allowed to rest for another 5-8 minutes to give a total ageing time of 60 minutes, while allowing the sample to relax from the shear applied during loading. Measurements were taken by performing creep tests with applied stress  $\sigma_E$  in the range of 0.1 – 204.8 Pa. Each creep lasted 60 seconds, and an additional 60 seconds of rest was allowed before the subsequent creep. The temperature ( $T = 25^\circ\text{C}$ ) was controlled using a peltier plate. This procedure was repeated with smooth and rough (sandblasted) upper plates (60 mm stainless steel).

The resulting creep data were used to reconstruct the flow curves for smooth and rough plates. For each applied stress, the shear rate signal was processed with an equilibration time ( $t_{\text{eq}}$ ) of 20 seconds and averaging time ( $t_{\text{avg}}$ ) of 40 seconds. In the averaging window (Fig. 5.2 (a)), the average shear rate was calculated and plotted against the applied stress (Fig. 5.2(b)). The flow curve shows a significant difference between the smooth and rough plates, which could be attributed to the effects of slip. Using a roughened plate yielded a flow curve with lower measured shear rates at both low and high applied stress. Interestingly, a smooth plate resulted in a monotonous flow curve more akin to typical CST, whereas a roughened plate produced a backward kink where the shear rate decreases with increasing stress, a characteristic feature of DST. In addition, the roughened plate captured a much higher variation in shear rate during the creep.

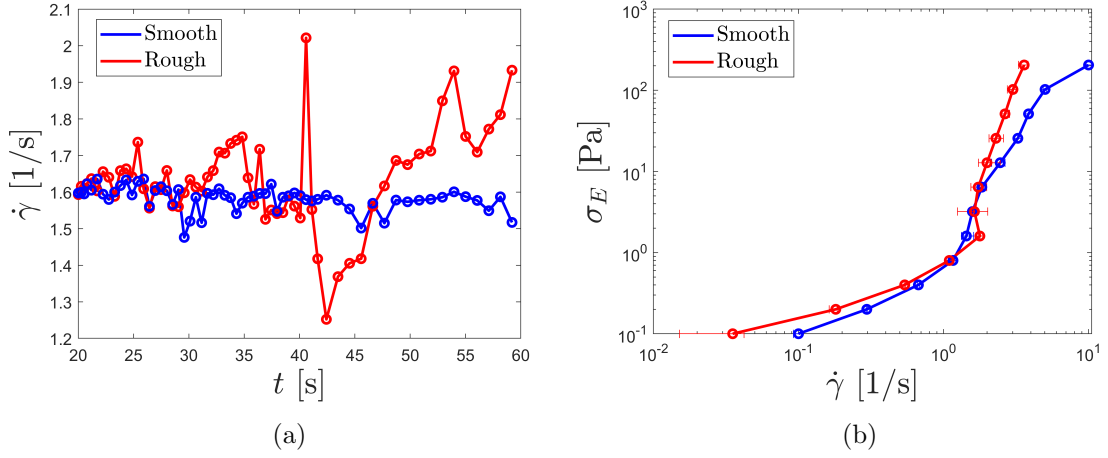


Figure 5.2: (a) Typical shear rate signal obtained during creeps ( $\sigma_E = 3.2$  Pa). (b) Flow curves obtained from the creep data.

### 5.2.2 Inertia: Experimental Design

The motivation for the following experiment is to investigate the effect of system-inertia on the measured oscillations. We reduce the inertia by either decreasing the plate diameter or reducing the gap size. The former only involves inertial effects, while the latter involved changes in inertia and potential confinement effect, hence, testing the effects of both should allow us to separate these two effects. However, since our samples age, each time we adjust either the gap height or plate diameter, we need to prepare a fresh sample and subject it to an identical ageing history. To ensure that the sample preparation does not introduce variance that might interfere with the effects of inertia or confinement, we set up two rheometers in parallel: one will be used as a control where each sample is measured with the same gap height and plate diameter, while the other will be used to modify the gap height and plate diameter.

The sample preparation procedure outlined in the previous section was repeated ( $\phi_v = 0.495 \pm 0.007$ ,  $x_g = 0.65$ ). After 15 minutes of rest, the sample was stirred and split into two parts. One part was loaded into a parallel plate setup (AR G2,

TA Instruments), with roughened lower and upper plates (60 mm sandblasted stainless steel), with a measurement procedure set to flow sweep ( $\sigma_E = 0.1 - 500$  Pa,  $t_{eq} = 10$  s,  $t_{avg} = 20$  s). The rest of the sample was loaded into a separate parallel plate setup (HR 30, TA Instruments), with roughened upper and lower plates. Here, the measurement procedure was set to a sequence of creep tests ( $\sigma_E = 0.1 - 320$  Pa) with 120 second creep duration and a 60 second break between creeps. After loading, at least 5 min rest time was allowed (depending on the loading time) to give total maturing time of 30 min, and both measurements were started simultaneously. Both setups were temperature controlled ( $T = 25^\circ\text{C}$ ) with peltier plates. This sample preparation and loading procedure was repeated with varying gap height ( $h_{gap} = 750, 1000, 1500, 2000$   $\mu\text{m}$ ) and plate diameter (40 mm and 60 mm) on the HR 30 rheometer. The gap height ( $h_{gap} = 1000$   $\mu\text{m}$ ) and the plate diameter (60 mm) on the AR G2 rheometer was kept constant and the flow sweep served as a control experiment.

### 5.2.3 Flow Curves, Oscillations and Inertia

Starting with control flow sweeps (Fig. 5.3), we obtain a typical shear-thickening flow curve often measured in DST systems [6; 129]. Note that while the system used in this experiment is certainly DST (see Section 6.4), we do not measure the unique 'S-shape' rheology, due to the previously discussed challenges in simple-shear rheology for DST materials (see Section 4.2). Of the eight flow sweeps reported, only one produced a slight backward kink at  $\sigma_E = 3.98$  Pa, but none reproduced the negative gradients in any meaningful sense. The second notable feature is the clear evidence of consistent edge fractures around 160 Pa. In fact, in all flow sweeps, edge fractures or expulsion material from the gap was observed. Finally, by far the most significant source of uncertainty in the reported value of the effective volume fraction is the mass fraction of corn starch occupied by moisture,  $\beta$ . This value is affected by both temperature and humidity, neither of which was controlled or measured across experiments. Since the control flow sweep experiments were carried out over a period of approximately two weeks, sample preparations during this period should reflect

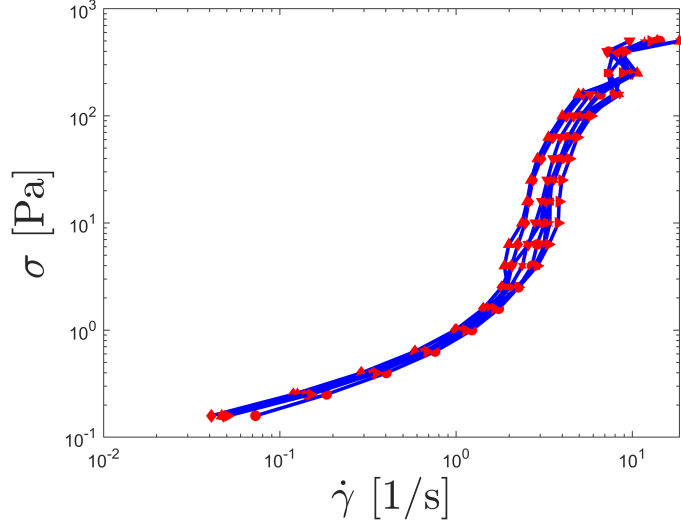


Figure 5.3: Flow curves measured via flow sweeps in the control setup. No systematic variation is present in the reference experiment. Constant gap height of 1000  $\mu\text{m}$  with a 60 mm plate.

typical fluctuations in temperature and humidity, which in turn should appear in the flow sweep measurements. Around  $\sigma_E = 1 \text{ Pa}$  (below the onset of shear thickening), we measure the spread in the measured shear rate of approximately  $\pm 0.24 \text{ s}^{-1}$ . We can relate this to the uncertainty in the reported volume fraction via the Maron-Pierce relationship, leading to an uncertainty of  $\pm 0.007$  in  $\phi_v$ . This value is likely quite conservative, given that we conflate the uncertainty in rheometer measurements with the uncertainty in sample preparation, but the value is not unreasonably high based on the experience with the sample preparation.

By reducing the diameter of the plate at a constant height of the gap, we reduce the amount of inertia involved in the acceleration and deceleration of the plate during oscillations. Decreasing the gap height with a constant plate diameter should have the same effect with respect to inertia, but it may also involve confinement effects. In this context, confinement effects refer to the phenomena observed by [139], where strong confinement (reduction of the gap height) prevents spatial heterogeneities

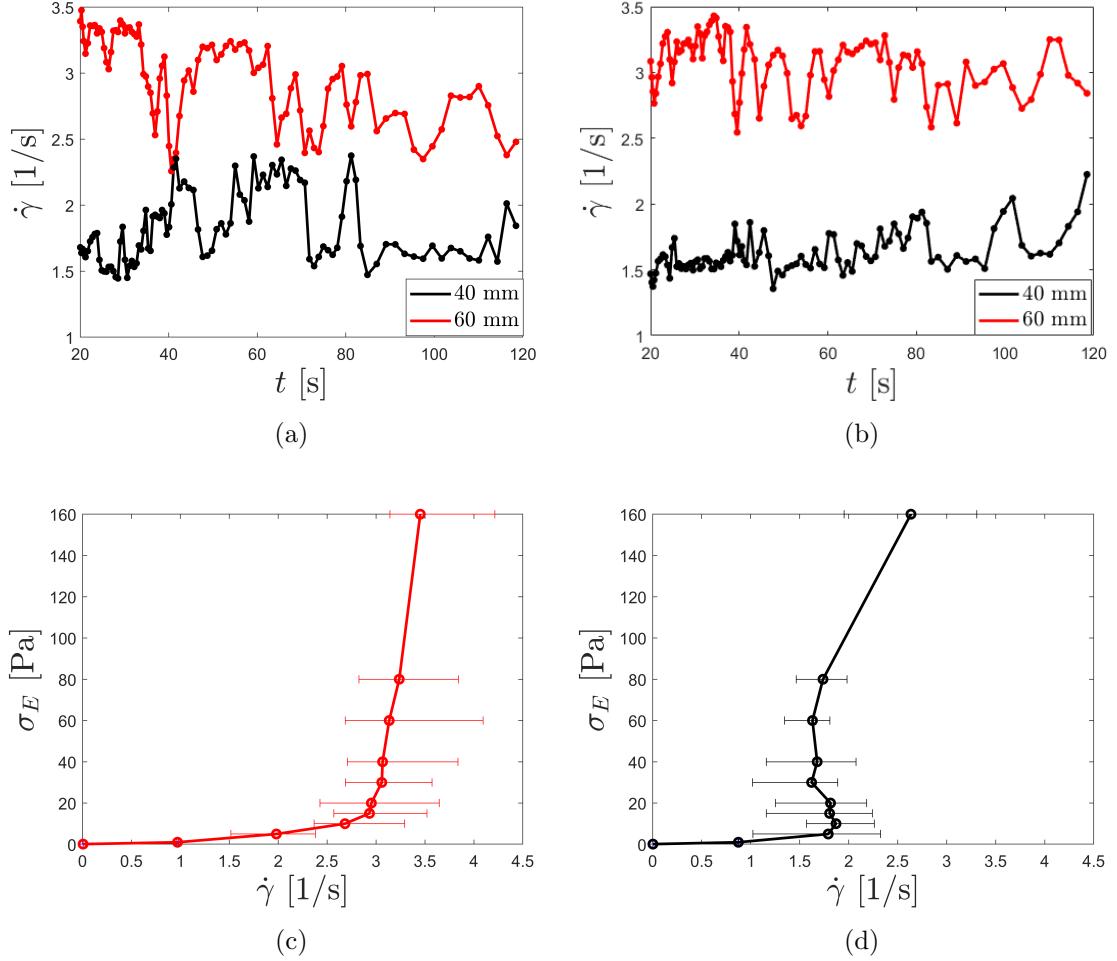


Figure 5.4: (a,b) Oscillations in the measured shear-rate signal ( $h_{gap} = 2000 \mu\text{m}$ ) for (a)  $\sigma_E = 20$  Pa and (b)  $\sigma_E = 30$  Pa. (c,d) Constructed flow curves for  $h_{gap} = 2000 \mu\text{m}$ , (c) 60 mm and (d) 40 mm plate diameters. The error bars in the shear rate indicate the maximum and minimum measured value.



from developing into rheochaotic regimes. This confinement likely best understood in relation to the characteristic spatial pattern length scale, as opposed to the typical confinement with respect to the individual particle size. In principle, by varying both the plate diameter and the gap height, we should be able to separate the effects of inertia and confinement. Figure 5.4 shows typical oscillations in shear rate and flow curves constructed from creep signals ( $t_{eq} = 20$  s,  $t_{avg} = 100$  s). During flow curve construction, the equilibration and averaging time were adjusted to 100 s and 20 s, respectively, for measurements at low applied stresses  $\sigma_E < 1$  Pa as it was clear that no oscillations were present, but the signal required more than 20 s to reach steady state. Comparing the flow curves for high inertia (Fig. 5.4(c)) and low inertia (Fig. 5.4(d)), the high inertia curve displays a monotonous increase, whereas the low inertia curve has a noticeable negative gradient and resembles a weak 'S'-shape. This comparison is identical when comparing plate diameters at 1000  $\mu\text{m}$  and 1500  $\mu\text{m}$ , but not at 750  $\mu\text{m}$  where neither plate diameter produces negative gradients or backward kinks. Conversely, no such trend with respect to inertia can be found when the plate diameter is held constant and the gap height is varied. Between the weak effect in changing the plate diameter and the lack of effect in changing the gap height, it is difficult to draw a conclusion on how the inertia (or confinement) affects the measurement of flow curves.

Finally, we examine the effect of inertia on oscillatory behaviour during creeps. For each creep, the representative amplitude  $A$ , was estimated by measuring the standard deviation in the distribution of the shear rates measured over time. The analysis is limited to the applied stress range  $\sigma_E \leq 80$  Pa, as above this range edge fractures were common. The results plotted in Fig. 5.5 appear noisy and difficult to interpret, yet show a general trend of increasing amplitude with increasing inertia (gap height) for both plate diameters. No clear trend in amplitude is present with increasing input stress, beyond the clear onset of instability around 5 Pa. The lower gap height tends to increase gradually in amplitude with increasing stress, while the higher gap heights tend to peak around 15 Pa and decrease from there.

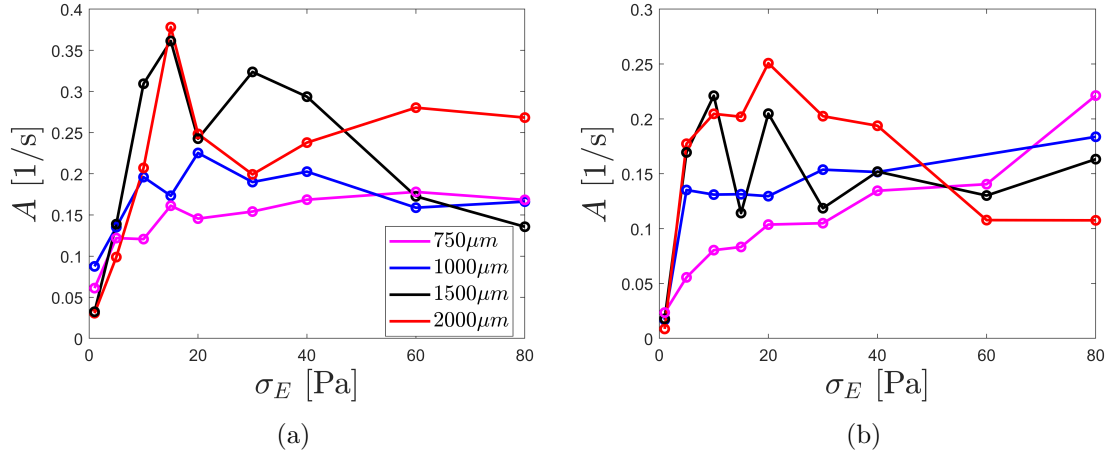


Figure 5.5: Standard deviation,  $A$ , in measured shear rate at different applied stresses for (a) 60 mm and (b) 40 mm.

### 5.3 Conclusion

In anticipation of the main work on the free surface flows, we have considered the model system (corn starch) as an unstable ageing material. We conducted ageing experiments with pure glycerol suspension to demonstrate the degree of time dependence exhibited by corn starch suspensions, highlighting the need to either monitor the material properties in control experiments or present the ageing history along with the usual material parameters. The results of the ageing experiment allowed us to eliminate particle swelling and narrow the range of possible ageing mechanisms to liquid pore intrusion, although decisive confirmation would require extensive work beyond the scope of this work.

The effect of slip was addressed and documented by comparing oscillating shear rate signals and constructed flow curves using smooth and roughened plates. The roughened plates had significantly stronger oscillations and altered flow curve shape, pointing to the influence of slip in the smooth plates. Based on these results and typical procedures used in the literature on DST, a set of disposable upper and lower

plates was roughened by sandblasting for use in future rheological measurements.

The influence of inertia on the construction of the flow curve and oscillatory properties was investigated by repeatedly preparing the same sample and measuring its properties under control and varying inertia conditions, at a constant ageing time. The results displayed a weak effect on the shape of the curves, with presence of negative gradients in measurements using smaller plate diameter, however, due to lack of any effect with varying gap height the study was inconclusive. The lack of effect is interesting in the context of the work of Hu et al. [139], in which they report significant effects of confinement (and thus inertia) on the measured flow curves. It is possible that the range of gap height and plate diameters used in this work is not large enough to achieve a noticeable effect, and using even smaller gaps and swapping stainless steel for a lighter plate material could enhance and clarify the effect of inertia. It is also possible that the inherent material instabilities present in corn starch, which do not affect their model system (polystyrene in water), are significant enough to obfuscate the weak trends. However, increasing the inertia of the system, either by increasing the gap height or the diameter of the plate, seemed to result in a consistent increase in the amplitude of the measured shear rate. The exact trend of the amplitude with changing was found to be unclear and varied depending on the height of the gap, with the exception of bifurcation at 5 Pa.

In future work, focused on the fine detail of material characterisation and DST rheology in simple shear, moving away from corn starch towards more stable model systems would be preferred. However, in the context of the main scope of this work, such systems are not suitable because of the high cost associated with the large volumes of material required for free surface experiments. The work laid out in this section, despite its inconclusive nature in detail, has been critical in laying out the expected type and range of behaviour we can expect in corn starch suspensions. It allows us to use rheological measurements as a monitoring tool in the following large-scale experiments and to account for the ageing nature of corn starch. Perhaps the most important result of this study is the control flow sweep experiment, which allows us to quantify the uncertainty in the reported effective volume fraction associated with fluctuating temperature and humidity.

# Chapter 6

## Instabilities in Free Surface Flows

### 6.1 Introduction

Inclined plane free surface flows are the most well-studied large-scale flows of discontinuous shear thickening fluids. The origin of this setup dates back to the work of Balmforth et al. [7] who reported the formation of well-defined surface roll waves in a thin film (5 – 10 mm) of corn starch flowing in a wide inclined chute. Although the presence of wave formation in inclined fluid flows had already been extensively studied and reported [62; 145; 63; 64], at the time all the literature focused on the inertial instability mode (Kapitza instability [61; 146]) and associated modifications for non-Newtonian fluids. However, the experiments of Balmforth et al. [7] produced a new distinct type of wave (roll waves) at Reynolds number values that were multiple orders of magnitude below the inertial mode. This suggested the existence of some non-inertial (viscous) mode of instabilities, unique for DST fluids. The key work on the primary roll wave instability comes from the group of Darbois Texier et al. [87]. Their experimental work confirmed the existence of a non-inertial instability mode by demonstrating a clear transition in the measured critical onset stress and wave speed for volume fractions with  $\frac{d\dot{\gamma}}{d\sigma} < 0$ . More recently, they continued their work by developing a theoretical framework for the free surface instabilities [57], including the combined effects of inertia in the DST regime and strain delay in microstructure

evolution.

Although the DST origin of the roll waves has been extensively studied, these investigations have focused narrowly on the effects of shear-thickening rheology. However, suspensions such as corn starch are understood to have compounding effects which form a complex picture. For example, dilatancy effects are suspected to play a key role in the upstream motion of localised high-viscosity structures [60]. In simple shear, similar localised solid-like phases (SLPs) are observed and are accompanied by the migration of particles (and solvent) along the vorticity direction [90; 91]. How such phenomena might affect free surface flows is not clear. Furthermore, typical studies involving DST roll waves are limited to small inclination angles.

In this work, we seek to map a wide range of parameter space to better understand the extremes of the roll wave phenomenology. The structure of this chapter is as follows. In sections 6.2, 6.3 and 6.4, we will introduce the tilting table experimental setup, describe the experimental procedure for the surface wave experiment, and discuss the results, respectively. Next, in the section 6.5 we will introduce a theoretical framework for the ridge instability observed in our wave experiments. In the remaining sections of this chapter, we will turn to modifying the experimental design to allow for optical measurements of second normal stress differences to validate the theoretical model with experimental data.

## 6.2 Experimental Setup: Tilting Table

A tilting table setup was designed and manufactured for the purpose of studying the flows of thin suspension films down inclined surfaces. The setup consisted of three primary components: the base, the mounting rod, and a table attachment. The base was a metal frame standing on 4 extendable legs, which could be adjusted via screws in the frame. This allowed for levelling of the table independently of the lab floor. On one side of the frame, a thick metal sheet was attached, with holes for screws positioned in increments of approximately  $5^\circ$  around the rim of the sheet. These holes were used to set the desired tilt angle by screwing in a metal rod on the inner

side of the sheet to serve as a stopping mechanism. Two optical holders were used, one to set the table level and the other for setting the desired tilt angle, so that both could be set before starting the experiment. On the back end of the frame, a vertical screw was attached to serve as an adjustable backstop. With the front-level optic holder firmly screwed in, the backstop screw could be used to level the table.

The table component consisted a clear perspex tray with internal dimensions of 30 cm width, 100 cm length and approximately 10 cm wall height, with an adjustable camera mounting bracket in the middle and an outlet gate in the front. The gate was opened and closed by adjusting a nut and a washer along a guiding thread built into the table. The table was attached to the frame by threading the mounting rod through the bracket slots beneath the table.

### 6.3 Tilting Table Experiment

The glycerol-water mixture ( $x_g = 0.650 \pm 0.002$ ) was prepared by mixing them in a large bucket for approximately 5 min. Corn starch powder (Sigma Aldrich) was added in moderate increments (200 – 350 g) and vigorously mixed into the solvent. During mixing, the dry powder clumps had to be manually broken, either with a mixing spoon or a hookpick, using a crushing motion and dredging the bottom to remove the sedimenting clumps. The stirring became progressively more difficult as corn starch was added, which to some extent was alleviated by the incremental addition. The increments of added corn starch were planned so that the last increment, which would turn the suspension from CST to DST, was as small as feasible to avoid mixing large amounts of powder in the most challenging regime. The mixing process typically took between 30 and 45 minutes, depending on the desired volume fraction and the experimental investigator’s experience with mixing.

After preparing the sample, it was allowed to rest for 45 minutes, with intermittent mixing, and subsequently divided into three parts. A small amount of the sample was loaded into a parallel plate rheometer (AR G2) with 1000  $\mu\text{m}$  gap height and 60 mm sandblasted plate (and roughened lower plate). The rheometer was set

to flow sweep measurements ( $\sigma_E = 0.1 - 500$  Pa,  $t_{eq} = 10$  s, and  $t_{avg} = 20$  s). The sample temperature ( $T = 25^\circ\text{C}$ ) was controlled using peltier plates. The edge of the plates was not covered with silicon oil to allow for evaporation. After loading the rheometer, most of the suspension was transferred to the tilting table setup, with some of the sample (15 – 20%) retained in the bucket for future refilling, and allowed to rest to allow the air bubbles trapped during transfer to reach the surface, and to allow the fluid to distribute evenly across the surface of the table.

After 1 h of ageing time (not including the mixing time), the surface was cleaned by removing any remaining bubbles with a hookpick, and the height of the fluid film was measured using a Vernier caliper. Height measurements were taken approximately along the centreline at three different points, 25 cm, 50 cm, and 75 cm away from the front gate. The experiment started with the camera recording. The nut on the front gate was unscrewed, but the gate was held shut manually (usually adhesion at the seal was enough to hold it closed) while the levelling holder was unscrewed. Once the holder was removed, the table was manually tilted to the desired angle stop, and the gate was fully opened during the tilt motion. The suspension was allowed to drain into a container for approximately 60 – 120 s. In preliminary work, the weight of the container was measured during the flow by placing the collecting container on a scale, allowing measurements of the fluid mass over time. After the experiment, the collected suspension was transferred back to the table and allowed to rest. Due to the difficult nature of the DST suspensions, some of the fluid was often lost in the transfer, and the table had to be refilled with the previously set aside sample to maintain a constant fluid film height. After refilling, the fluid was allowed to distribute for approximately 5 min in the level (horizontal) position, while a new desired angle was preset.

The experiment was repeated with an angle that varied in increments of  $10^\circ$ . Additional resolution was provided in the transition range for primary roll waves and secondary ridge instabilities by reducing the increment to  $5^\circ$ . The exception here was the angle of  $65^\circ$ , where the frame obscured the screw hole in the metal sheet and an improvised stop had to be used, consisting of a tightly attached clamp. Flow sweep measurements were taken in parallel with the table measurements at  $10^\circ$ ,  $50^\circ$

and  $80^\circ$ , to track potential ageing effects during the experiment. After completing all measurements, the table was cleaned of any suspension, and the angle at each increment was precisely measured with a digital spirit level (Bosch GIM 60).

## 6.4 Free Surface Pattern Formation

The experiment was carried out in two separate runs, both in a similar range of effective volume fractions ( $0.45 - 0.52$ ) but not necessarily at identical volume fractions. The preliminary run used food-grade corn starch obtained from the local store and its main purpose was to sketch out the expected behaviour. In this run, the fluid mass in the container was measured over time, allowing estimation of the flow rate of the suspension mass,  $\dot{M}$ . The mass flowrate was used to calculate the volumetric flowrate using averaged suspension density

$$Q = \bar{\rho} \dot{M} \quad (6.1)$$

$$\bar{\rho} = \frac{1}{\frac{1}{\rho_L}(1 - x_m) + \frac{1}{\rho_{cs}}x_m}, \quad (6.2)$$

where,  $x_m$  is the solid mass fraction,  $\rho_L = 1.17 \text{ g cm}^{-3}$  is the solvent density, and  $\rho_{cs} = 1.62 \text{ g cm}^{-3}$  is the corn starch density. We estimate the average flow velocity

$$\bar{u} = \frac{Q}{h_0 w}, \quad (6.3)$$

where  $h_0$  is the measured base flow film height (film height in absence of any instability) and  $w = 0.30 \text{ m}$  is the internal width of the table. Finally, we estimate Reynold's number [7]

$$Re = \frac{\bar{u}^2}{g h_0 \sin \theta}. \quad (6.4)$$

Across all volume fractions in the preliminary run, the maximum Reynold number was on the order of  $Re \approx 0.01$ , and the vast majority of measurements had  $Re \ll 0.01$ . Based on this, we can exclude any possibility of the inertia-driven Kaptiza instability in the range of parameter values used in this study.



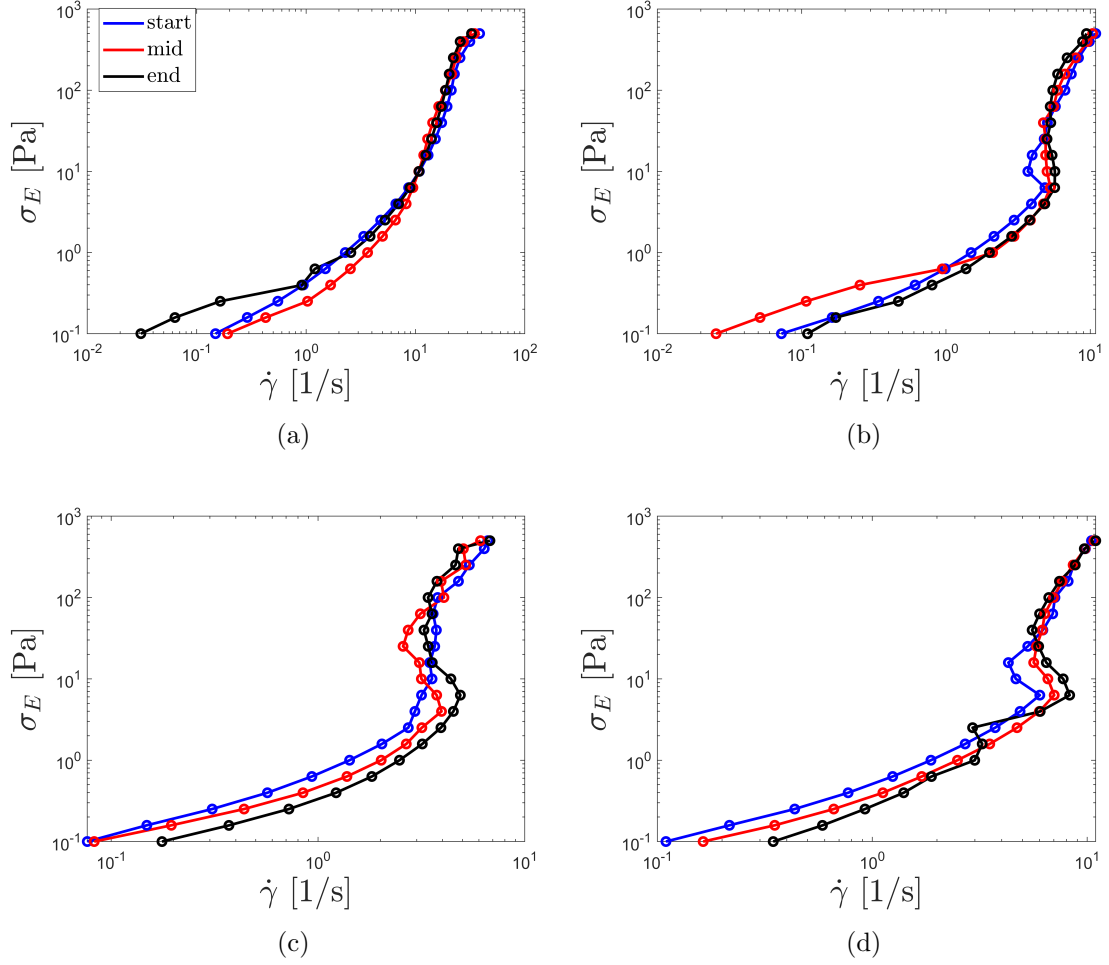


Figure 6.1: Flow sweep results for (a)  $\phi_v = 0.450 \pm 0.007$ , (b)  $\phi_v = 0.480 \pm 0.007$ , (c)  $\phi_v = 0.486 \pm 0.007$ , and  $\phi_v = 0.491 \pm 0.007$ . The blue, red and black lines indicate measurements taken at the start ( $\theta = 10^\circ$ ), in the middle ( $\theta = 50^\circ$ ), and near the end ( $\theta = 80^\circ$ ) of the table experiment, respectively.

The flow sweep measurements were used in both runs; however, due to a peltier plate failure during the main run, only data for the first two volume fractions are available ( $\phi_v = 0.470 \pm 0.007$ , and  $\phi_v = 0.480 \pm 0.007$ ). Fortunately, the data from these two measurements are consistent with the preliminary results. The prelimi-

nary results are plotted in Fig. 6.1. For  $\phi_v = 0.450 \pm 0.007$ , a very weak ageing effect is measured at high applied stress ( $\sigma_E > 10$  Pa) and no clear trend is present below. Note that results at very low applied stress ( $\sigma_E < 1$  Pa) tend to be affected by inertia, resulting in a large variation in measured values. Measurements for the rest of the volume fractions show no clear ageing trend, and end flow curves often have the highest shear rate the onset of negative gradients in the flow curve under moderate stress ( $\sigma_E = 10$  Pa), but the lowest shear rate at high stress ( $\sigma_E > 100$  Pa). For  $\phi_v = 0.486 \pm 0.007$  and  $\phi_v = 0.491 \pm 0.007$ , low stress results would suggest a reverse trend in ageing (reduction in volume fraction), which could indicate an effect of sedimentation. Even if we take these readings at face value and assume that sedimentation is the culprit here, rather than the inherent variability of measurements at low stress, such an ageing mechanism would not affect the table measurements where the suspension is constantly mixed between measurements.

Having ruled out Kapitza instability and accounted for ageing effects, we consider the range of possible patterns (Fig. 6.2) formed across a range of parameters used in the study. Starting at the lowest volume fraction ( $\phi_v = 0.470 \pm 0.007$ ) at all angles, there are no roll waves. Considering that this particular sample did not show the characteristic DST behaviour during mixing and handling, this result is consistent with the idea that the roll waves are unique for the DST regime. However, once an angle above  $70^\circ$  is applied, a different type of pattern is established. The suspension begins to organise itself into long, tall strands (or ridges) which are continuous in the flow direction but break symmetry along the width of the table (Fig. 6.2(d)). These ridges are separated by zones of depletion as the fluid appears to be driven inward into the ridges. The surface of these structures is notable for being absent of any waves, mostly smooth, although in some cases the ridges appear to curve during the flow. This mode of instability is clearly different from the typical roll waves, and given that they appear for a CST volume fraction, their origin likely does not lie in the DST rheology. Currently, we are not aware of any prior literature discussing this pattern. Henceforth, we will refer to this type of pattern formation as a secondary instability (the primary instability being the roll waves) and a detailed discussion of their origin will be presented in the following section.

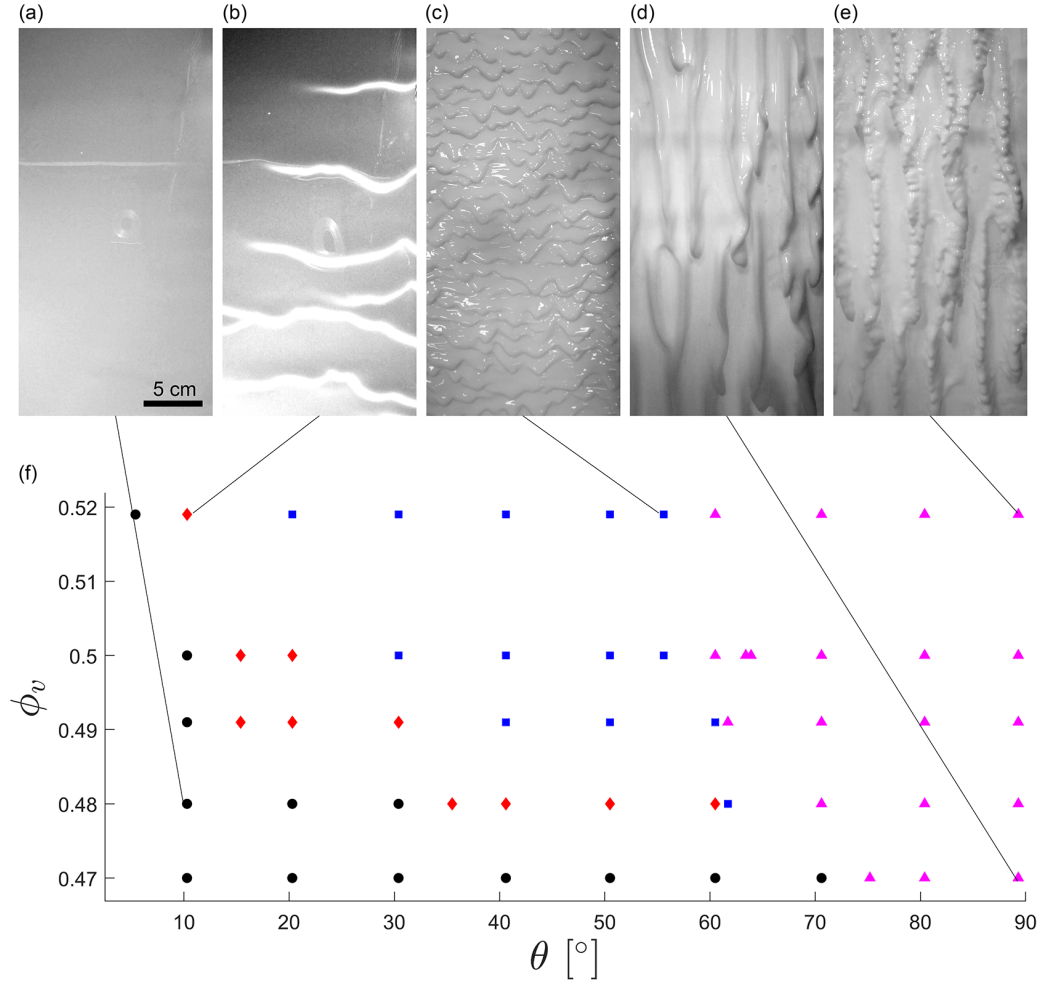


Figure 6.2: Examples of typical flow patterns observed across all parameters. The flow direction ( $x$ ) is vertically downwards in the images, and the spanwise dimension ( $z$ ) is horizontal. The featured patterns include (a) flat surface (no instability), (b) roll waves, (c) teardrops, (d) pure ridges, and (e) ridges with roll waves.

The rest of the volume fractions can be discussed together, as they all show the same type of progression with varying bifurcation points. At sufficiently low angles, all volume fractions have a stable mode of flow, where no surface disturbances are observed (Fig.6.2(a)). Increasing the angle will eventually drive the flow into the typical DST mode of instability with the appearance of roll waves (Fig.6.2(b)). This pattern is characterised by regular waves that generally span the entire width of the table in an unbroken manner. The frequency of waves increases with the angle, and eventually they begin merging into a more complex pattern. Still, with or without merging, this pattern is fairly easy to distinguish, and the main defining features of the roll wave are retained. Further increases in angle drive a continuous transition in the pattern, where the symmetry of roll waves along the width is broken (Fig.6.2(c)). Parts of the wave front begin to race ahead of the front, while other parts are held back, resulting in a teardrop-shaped pattern. Once these teardrops are formed, no single unbroken strand of wavefront along the width can be observed. At even higher angles, another transition occurs, and the flow arranges itself in the previously discussed ridge pattern. The main difference here is that the surface that the ridges are covered in roll waves (Fig.6.2(e)).

Since teardrop and ridge (with or without waves) instabilities are orientated along the vorticity (width) direction, we classify them as secondary instabilities. The final (tertiary) mode instability observed in all volume fractions was the presence of very small amplitude but high frequency waves. Interestingly, these waves are orientated in the flow direction but move against the flow of the suspension. They can be seen very clearly in all the DST volume fractions (although difficult to image) for all angles where the roll waves and teardrops are present. Their presence is less clear in the CST volume fraction - at  $\theta = 60.5^\circ \pm 0.01^\circ$ , in the absence of primary instability and before the onset of secondary instability, the surface was covered in very high-frequency waves. The waves were clearly distinct from typical roll waves and could only be seen by looking at the breaking of the external light reflected on the fluid surface. Whether the observed phenomena are different from the tertiary instabilities observed in the DST samples, or whether the presence of the primary instability simply makes the tertiary effects easier to see is unclear. Of all instabil-

ities discussed in this work, tertiary instabilities are the least well understood. The closest reported phenomenon comes from the work of [60], who reported upstream moving frictional solitons in an inclined pipe flow of corn starch suspensions. They attribute this effect to Reynolds-like dilation in the material. Granular effects are understood to be present in simple shear instabilities, where rheochaotic oscillations are accompanied by the migration of particles along the vorticity direction. It is possible that the tertiary instability is a granular effect, which would explain why it occurs for both CST and DST samples, which is enhanced by increases in volume fraction and DST effects resulting in clearer effect, observable at lower angles for higher volume fractions. Beyond this speculation, the nature of the tertiary instability is not understood in great detail, and further discussion is beyond the scope of this work. In summary, patterns are classified into primary or secondary instabilities based on the axis of symmetry breaking: primary (roll waves) patterns break symmetry along the flow direction, while secondary (ridges) patterns break it along the flow direction. vorticity direction. The tertiary mode of instability is distinguished by the reversed direction of wave motion (counterflow), which distinguishes it from the primary roll waves, and is reminiscent of the counterflow motion effects observed in other geometries [60; 139].

Primary and secondary instabilities have clear trends in their respective bifurcation points. In the case of secondary instabilities, we only refer to the transition between teardrops and ridge-like patterns - the transition from roll waves to teardrops is significantly less clear, and it is difficult to draw a clear bifurcation between the two patterns. The onset angle ( $\theta_c$ ) for the roll waves decrease with the volume fraction, with the maximum angle ( $\theta_c = 33.0^\circ \pm 2.5^\circ$ ) for  $\phi_v = 0.480 \pm 0.007$  and the minimum angle ( $\theta_c = 7.9^\circ \pm 2.5^\circ$ ) at  $\phi_v = 0.519 \pm 0.007$ . The onset angle throughout this work is reported by taking a midpoint between an unstable and stable measurement and reporting the width of the increment between them as the uncertainty. The trend is similar in the case of ridges, with the maximum angle ( $\theta_c = 72.9^\circ \pm 2.3^\circ$ ) for  $\phi_v = 0.480 \pm 0.007$  and the minimum angle ( $\theta_c = 58.1^\circ \pm 2.4^\circ$ ) for  $\phi_v = 0.519 \pm 0.007$ . Since DST materials are particularly sensitive to applied stress, it might be sensible to present the transition points in terms of shear stress rather than angle. We

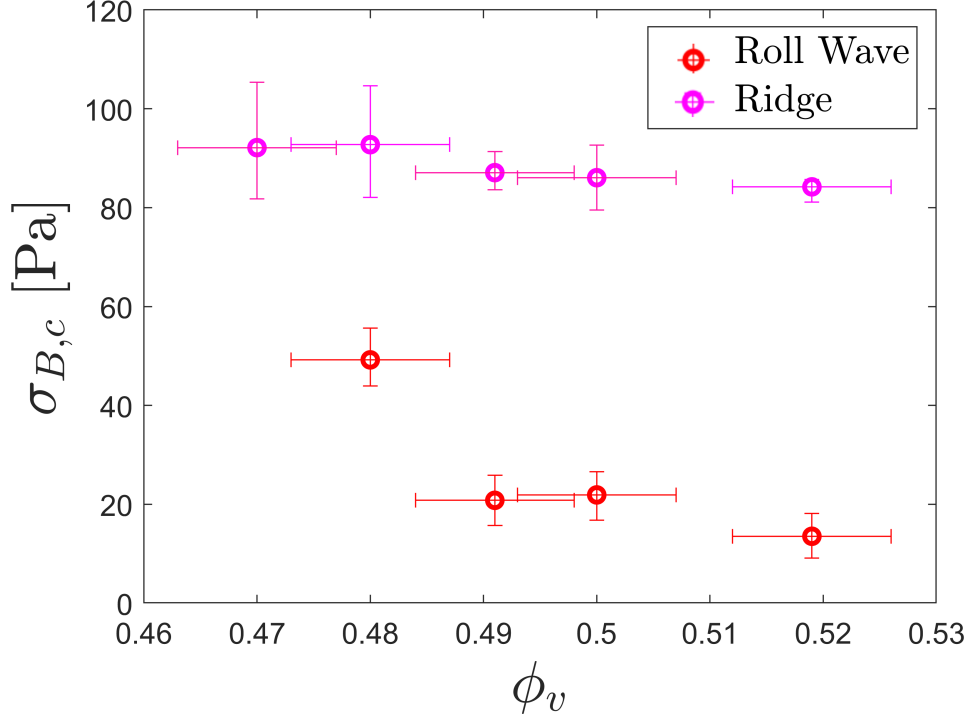


Figure 6.3: Measured critical base stress for onset of roll waves (blue) and ridges (red) at different volume fractions. The error bars in stress encompass the uncertainty in both height measurements and the range of angles in which transition is possible. The dominant element in the uncertainty was the height measurements, leading to decreases in the uncertainty as more practice with the measurements was gained.

calculate the maximum basal shear stress,  $\sigma_B$ ,

$$\sigma_B = \bar{\rho}gh_0 \sin \theta. \quad (6.5)$$

This formulation represents the maximum shear stress for the base flow (in the absence of instabilities) at the table surface. The base flow height,  $h_0$ , is based on the average of the three measurements taken before tilting the table. The results for both instabilities are plotted in Figure 6.3. The critical onset stress for the roll waves appears to decrease with increasing volume fraction, in the range of volume fractions

between  $\phi_v \approx 0.480$  and  $\phi_v \approx 0.520$ . This could point to potential consistency with the model (and the results) of Darbois Texier et al. [57], in which they use a strain delay model (identical to the local microstructure evolution term previously used in this work in Chapter 3) to demonstrate that the critical onset stress for non-inertial roll waves diverges as the CST-DST transition is approached and vanishes with increasing volume fraction, but the present data is far too limited to draw strong conclusions. Due to the nature of the experimental design being aimed at probing a wide range of parameters, we lack the resolution required to map the values of critical onset stress near the CST-DST transition, where its values are expected to sharply diverge. Considering that the sample  $\phi_v = 0.470 \pm 0.007$  is classified as CST, the divergence should occur somewhere in the range of  $\phi_v = 0.470 - 0.480$ . This would explain why the jump in critical stress from  $\phi_v = 0.480 \pm 0.007$  to  $\phi_v = 0.490 \pm 0.007$  is much larger than from  $\phi_v = 0.490 \pm 0.007$  to  $\phi_v = 0.519 \pm 0.007$ . It would also explain why the measured critical stress is very similar for  $\phi_v = 0.480 \pm 0.007$  and  $\phi_v = 0.491 \pm 0.007$  - the variation in this volume fraction range is expected to be relatively small and the resolution used in this study cannot fully capture it in detail.

However, the trend in the onset stress for the formation of the ridges is less clear. The data show a decrease in critical stress with an increase in the volume fraction, but the trend is too weak relative to the experimental uncertainty to draw firm conclusions. In the absence of a clear explanation for the appearance of ridges, further work is needed to understand their origin.

## 6.5 Ridge Instabilities: Theory

To understand the origin of ridge instability, we look to the model of Xiong et al. [147]. The theoretical modelling presented in this chapter was carried out by Zhongqiang Xiong (the lead author), with a limited theoretical discussion on my part. My contribution to the cited work was limited to discussing and carrying out experimental validation. We begin by presenting a condensed form of the derivation in this work to lay out the key assumptions and underlying physics of the model. Starting with

the mass conservation

$$\nabla \cdot \mathbf{v} = 0, \quad (6.6)$$

after integration with free surface and no-slip boundary conditions we obtain

$$\frac{\partial h}{\partial t} + \frac{\partial}{\partial z} \int_0^h v_z dy = 0 \quad (6.7)$$

where  $h$  is the fluid film height, and  $v_z$  the component of velocity along the vorticity direction. Next we use conservation of momentum

$$\nabla \cdot \boldsymbol{\sigma} + \rho \mathbf{g} = 0 \quad (6.8)$$

where total stress tensor is given by  $\boldsymbol{\sigma} = -p\mathbf{I} + \boldsymbol{\tau}$ . Dimensionless parameters are defined

$$\bar{y} = y/H, \quad \bar{h} = h/H, \quad \bar{z} = z/L, \quad \epsilon = H/L \quad (6.9)$$

where  $L$  and  $H$  are system characteristic length scales in vorticity and gradient directions, respectively. To keep this presentation consistent with nomenclature in this work, coordinate system used by Xiong et al. [147] has been altered such that  $y$  represents the gradient direction, and  $z$  represents the vorticity direction. The relevant length scales (Fig.6.4) in this problem are the typical wavelength of the ridges across the width of the table ( $L$ ) and the base film height ( $H$ ), which result in the lubrication parameter  $\epsilon \ll 1$ .

After perturbation analysis using the lubrication parameter we obtain the following expression for the relevant component of the stress tensor

$$\bar{\tau}_{yz} = -\epsilon \left( \frac{\bar{h} - \bar{y}}{\tan \theta} \frac{\partial \bar{h}}{\partial \bar{z}} + \int_{\bar{y}}^{\bar{h}} \frac{\partial \bar{N}_2^{(0)}}{\partial \bar{y}} d\bar{y} \right) + \mathcal{O}(\epsilon), \quad (6.10)$$

where

$$\bar{N}_2^{(0)} = \alpha(\phi)(\bar{h} - \bar{y}) \quad (6.11)$$

is the zero-th order approximation of the second normal stress difference. A key assumption at this stage is that  $N_2$  is proportional to shear stress,  $N_2 = \alpha(\phi)\tau_{xy}$



such that  $\alpha(\phi)$  is a rate-independent constant for a given volume fraction [147]. This means that  $N_2$  has the same rate-dependence property as shear stress.

Substituting Eq.(6.11) into Eq.(6.10) allows for approximation of shear rate in  $z$  direction

$$\frac{\partial \bar{v}_z}{\partial \bar{y}} \approx -\frac{\epsilon}{\bar{\eta}(0)} \left( \frac{1}{\tan \theta} + \alpha(\phi) \right) (\bar{h} - \bar{y}) \frac{\partial \bar{h}}{\partial \bar{z}}, \quad (6.12)$$

which after integration with no-slip boundary condition yields an expression for the vorticity component of velocity

$$\bar{v}_z = -\frac{\epsilon}{\bar{\eta}(0)} \left( \frac{1}{\tan \theta} + \alpha(\phi) \right) \left( \bar{h}\bar{y} - \frac{1}{2}\bar{y}^2 \right) \frac{\partial \bar{h}}{\partial \bar{z}}. \quad (6.13)$$

Note that in Eq.(6.12) and Eq.(6.13),  $\bar{\eta}(0)$  is used, which means that the shear-thickening nature of the viscosity is ignored in this model.

Finally using Eq.(6.13) and Eq.(6.7) together results in the expression

$$\frac{\partial \bar{h}'}{\partial t} = \frac{\epsilon}{3\bar{\eta}(0)} \left( \frac{1}{\tan \theta} + \alpha(\phi) \right) \frac{\partial^2 \bar{h}'}{\partial \bar{z}^2}, \quad (6.14)$$

where  $\bar{h}'$  is the small perturbation on the base flow. Equation Eq.(6.14) is a diffusion-type equation with stable solutions for a positive value of the diffusion coefficient. However, for a negative diffusion coefficient, we obtain an unstable mode in which a small perturbation in the fluid film height will continue to grow. Hence, the flow is expected to be unstable along the vorticity direction for

$$\frac{1}{\tan \theta} + \alpha(\phi) < 0, \quad (6.15)$$

which can only be true if the material has a significant negative value of  $N_2$ . Although many suspensions satisfy this condition, to attribute ridge formation to the outlined model, an experimental investigation into  $N_2$  properties of corn starch suspensions is needed.

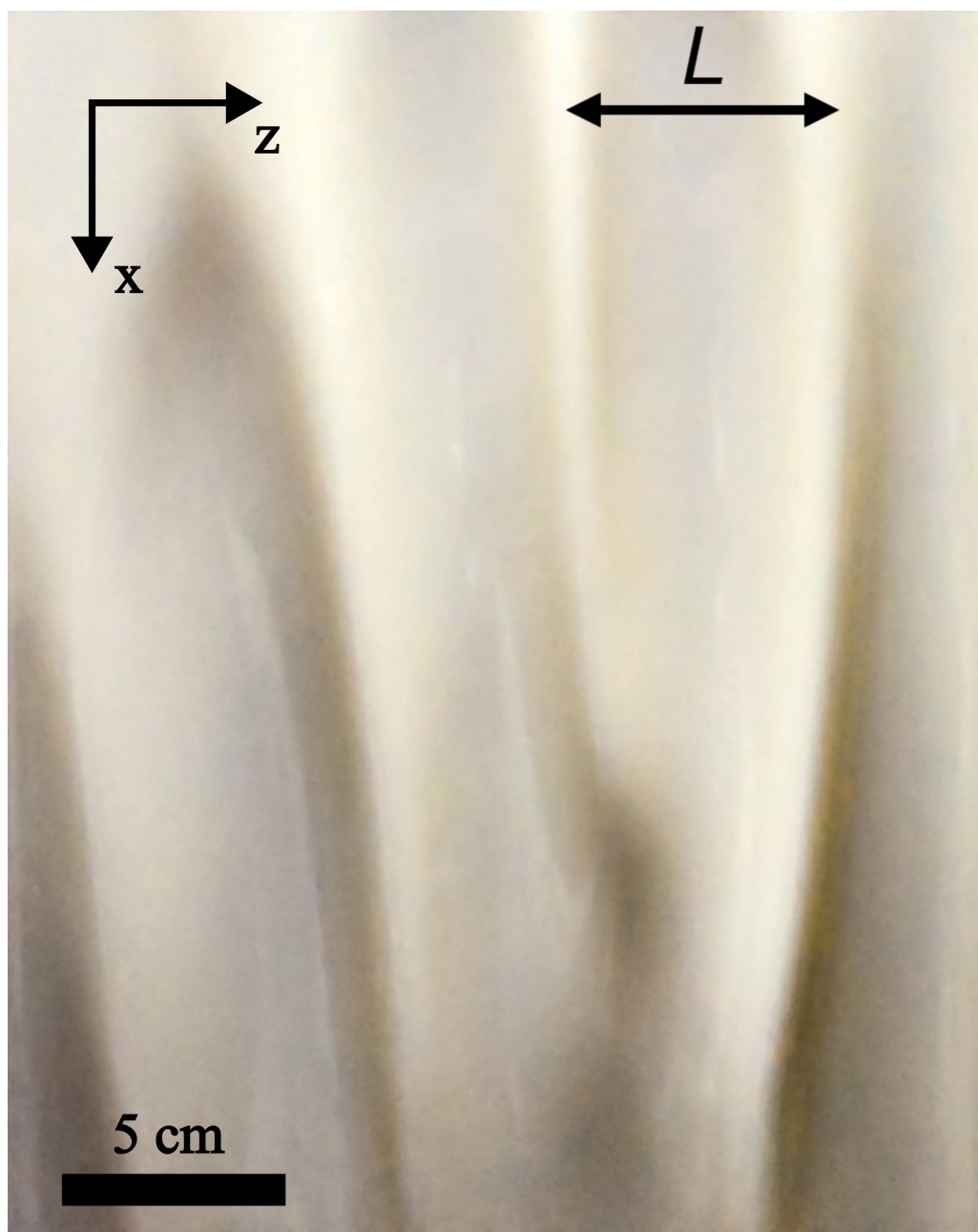


Figure 6.4: Typical ridge pattern.

## 6.6 Experimental Setup: Trough

To measure  $N_2$  we adopt the experimental technique of Keentok et al. [148], which requires the measurement of a surface profile in an inclined trough flow. In theory, irrespective of the pattern formation discussed so far, the presence of  $N_2$  should cause the flat base flow to deform with a convex deflection that indicates a positive value and a concave deflection that indicates a negative value of  $N_2$ . The value of  $N_2$  and its relation to shear stress depend on the exact shape and height of the profile, so a detailed measurement is required.

We modify the tilting table setup by swapping the table attachment for a clear pipe attachment with internal diameter  $d_i = 50.25 \text{ mm} \pm 0.1 \text{ mm}$  and length  $l = 140 \text{ cm} \pm 0.2 \text{ cm}$ . The pipe was held in place by a holding bracket around the pivot point. On both ends of the pipe, imaging windows were cut to allow for a clear view of the fluid surface, with the angle of the cut approximately  $20^\circ$  from the horizontal centreline. The additional height from the centreline produced by this was critical in the experimental process, as it allowed for overfilling of the pipe. Both ends of the pipe were enclosed with sealing caps, which could be easily removed. At the inner end of the front-facing window, a non-metallic ruler was horizontally attached to the pipe. The setup was levelled lengthwise and spanwise by adjusting the backstop screw and rotating the pipe within the holding bracket. An external camera, independent of the setup, was set up on the front end such that the attached ruler was in view with the fluid flow towards the camera. The purpose of the camera is capturing the reflection of the ruler in the fluid surface. To obtain a clear reflection we use a non-metallic ruler and point external light at the ruler from beneath the pipe so that the light does not directly fall on the surface (which would wash out the reflection). A diagram of the basic setup is shown in Fig. 6.5. In this view, we assume that the camera is aligned exactly with the centreline of the pipe (and that the pipe is symmetric across the entire length), so that only a two-dimensional picture is required to describe the placement of the camera and the pipe. The camera lens ( $S$ ) is tilted at an angle  $\mu$  to the horizontal, and a tracing line normal to the lens meets

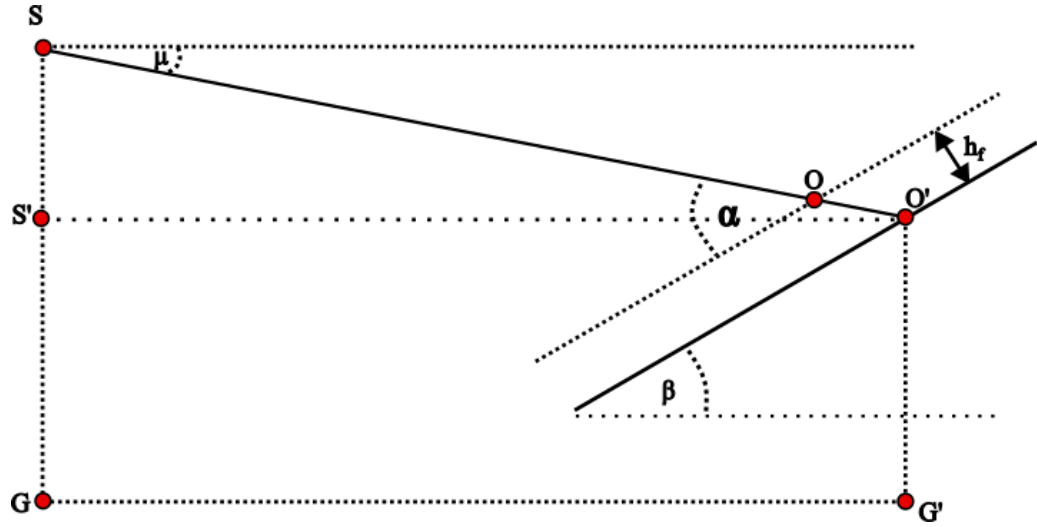


Figure 6.5: Camera (S) position relative to the tilted table.

the tilted pipe wall and the surface of the fluid with height ( $h_f$ ) at points  $O'$  and  $O$ , respectively. The pipe (and thus the fluid surface) are both tilted at an angle  $\beta$  so that the camera tracing line makes an angle  $\alpha = \mu + \beta$  with the plane parallel to the fluid surface. The points  $G$  and  $G'$  are placed on the laboratory floor, directly beneath the camera lens and the point  $O'$ , respectively. The point  $G(0,0)$  is the reference point in the laboratory frame from which all other coordinates are defined. Angle  $\mu$  was measured in two ways. One way involved measuring the tilt of the tripod mount with digital spirit level ( $8.1^\circ \pm 0.1^\circ$ ) with three repeat measurements along the width of the mount. The issue with this approach was that the mount tilt might not be exactly the same as the lens optical axis tilt based on how the camera is attached to the mount. Another method involved pointing the camera at the laboratory floor and marking the midpoint image point on the ground. By measuring the horizontal distance between the point and the lens, and the height of the lens, the tilt angle of the optical axis could be calculated ( $9.52^\circ \pm 0.07^\circ$ ). In this method some uncertainty was present in measuring the height of lens, with where the actual midpoint of the lens was. Since neither method is clearly superior, the

angle was taken as their average  $\mu = 8.8^\circ \pm 0.7^\circ$ .

For the purpose of image analysis, it would be convenient to align the camera such that when the fluid height along the central line of the pipe is at the midpoint of the pipe ( $h_f = d_i/2 = 25.10 \pm 0.05$  mm), the reflection of the ruler is also in the exact centre of the camera image. To achieve this, we further refine the setup as shown in Figure 6.6, by requiring that at the point  $O$  the angle made by the optical axis with the fluid surface be the same as the angle made by  $OR$  with the fluid surface, where  $R$  is the bottom of the ruler. By measuring the height of the ruler above the bottom of the pipe ( $H = 35.70 \pm 0.05$  mm) and using following relationship

$$x_R - x_0 = \frac{H - 2h_f}{\tan \alpha}, \quad (6.16)$$

we can calculate the distance along the pipe tilt plane between the ruler and the point  $O'$ . In practice, this distance is usually negative  $\Delta x = x_R - x_0 = -30.10$  mm. Knowing this distance allows us to mark a target point  $O'$  on the wall of the pipe ( $\Delta x_{measured} = -29.9 \pm 0.2$  mm). Since we already set the camera tilt, we now need to place the camera such that the middle of the image points directly at the marked target point. To do this, we fix the camera height and use the camera focusing user interface (which displays image midpoint along with gridlines) to point it exactly at the marked point by changing the horizontal distance from the pipe.

With some further geometry, the coordinate of the surface point  $O$  can be expressed as

$$O \left( GG' - \frac{h_f \cos \beta}{\tan \alpha} - h_f \cos [90 - \beta], O'G' - \frac{h_f \sin \beta}{\tan \alpha} + h_f \sin [90 - \beta] \right), \quad (6.17)$$

where distances  $GG' = 702 \pm 2$  mm and  $O'G' = 848 \pm 2$  mm can be measured. Hence, for a given fluid height we can calculate the coordinate of the surface fluid point, and the distance  $OS$  between the camera lens and the fluid surface.

The setup of the experiment in this very specific manner was designed to allow a simple measurement of the height of the fluid bump ( $h_m$ ) caused by  $N_2$ . In principle, if the camera was set up as described such that for a flat fluid surface (in the absence of  $N_2$  effects) the bottom of the ruler reflection was exactly in the middle of the image

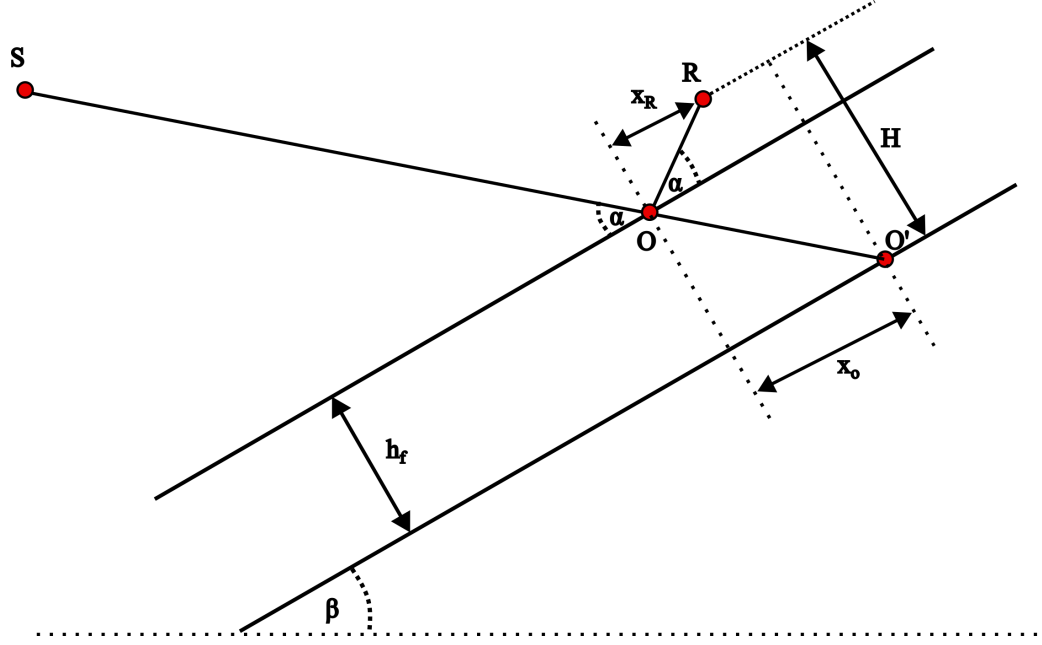


Figure 6.6: Schematic of the camera setup required to obtain reflection in the centre of the image for a given centreline fluid height.

when  $h_f = d_i/2$ , introduction of  $N_2$  effects should cause a deflection in the reflection which would shift the reflection upwards in the image due to the additional fluid height (see Fig. 6.7). By making more detailed measurements of the pipe geometry, the difference in the fluid height induced by  $N_2$  could be calculated

$$h_m = \frac{\frac{SD}{\tan \alpha} + \Delta L (h_f - H - SD) + SD \cdot DF - \frac{SD^2}{\tan \alpha}}{DF - \frac{2SD}{\tan \alpha}}, \quad (6.18)$$

where  $\Delta L$  could be related to the shift image by calibrating the image with a ruler. Unfortunately, this method has a major problem. Typically, measurements of  $N_2$  in trough experiments have been made in steady state mode, with recirculating flow and a reservoir. This allows the user to carefully adjust the flow rate of the suspension until the height of the fluid film at the walls reaches the desired height [148; 45]. In our case, the experiment is transient, and knowing when the fluid level at the wall is exactly at the midpoint would require an independent measurement coor-

dinate with the primary camera. Calling this special point in time is possible but difficult. In practice, it would require setting up and precisely aligning another camera, which would further complicate the experiment, and, as we will show later, camera alignment is already a major issue. Thus, without knowing when to take the measurement, using the reflection shift method does not tell us the additional height induced by  $N_2$ , only the absolute height at a given point in time. Instead, to calculate the height profile of the fluid, we will adopt an alternative measurement method. Fortunately, the setup procedure laid out appears to be very convenient for the alternate method.

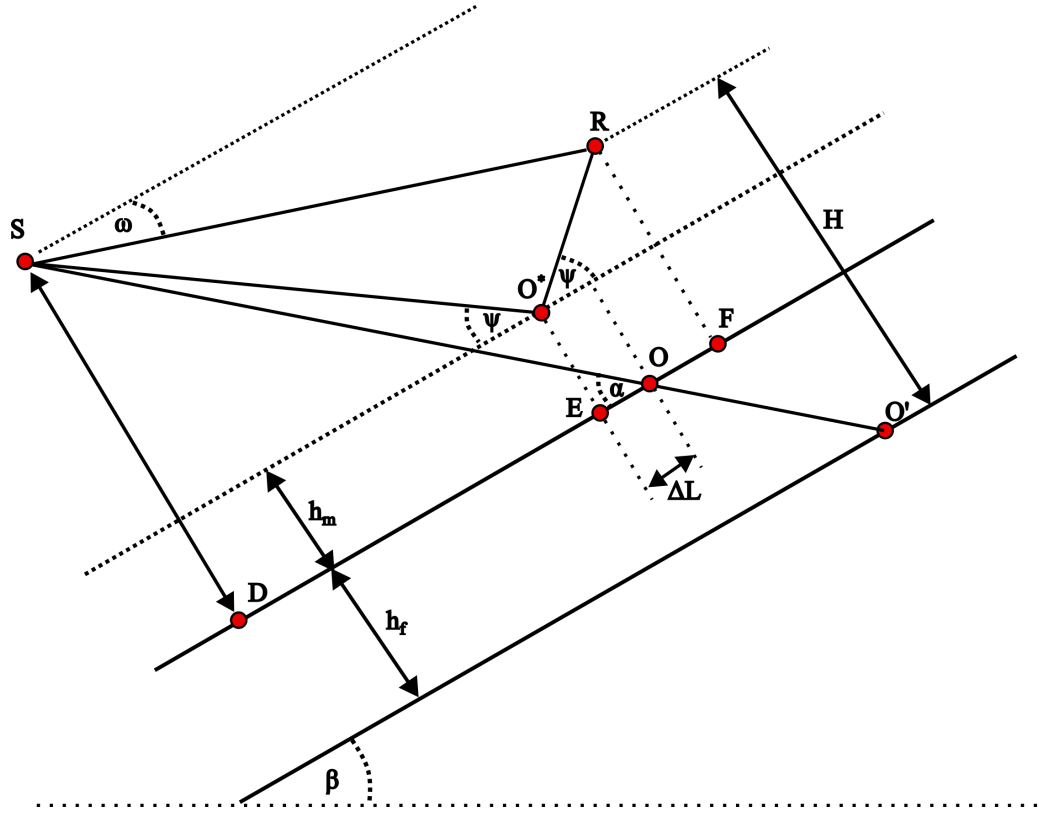


Figure 6.7: Diagram of the impact of disturbed fluid film surface on the acquired image.

## 6.7 Image Analysis

To calculate the fluid surface profile, we use the method of Keentok et al. [148] which infers the actual deflection of the surface from the shape of the reflection of the surface. This method is based on the idea that when a tracing line (i.e. light ray) originating in the middle of the lens impacts a concave fluid surface, by the law of reflections, the line will reflect upward (toward the reflected object - the ruler) but also sideways. If a graduated object is used, one can track the relative 'true' position of a given graduation and its accompanying reflected position. From these positions in the image, one can calculate the true relative positions in the laboratory frame and the slope of the reflecting surface. The required calculation is long and difficult, so we omit the details for the sake of brevity, but the procedure is fully laid out in the appendix of Keentok et al. [148]. Instead we will outline key steps required for such calculation to be possible.

We start by defining three terms: real space, image space, and pixel space. The real space ( $\mathbf{x}$ ) is simply the measurement of a distance in a true laboratory frame. For example, if we look at an image of a ruler, we know that the true distance between two graduations is 1 mm. The image space ( $\mathbf{x}'$ ) is the measurement of an image; for example, the graduation of 1 mm might occupy 3 mm when measured on a printed or displayed image. Finally, pixel space ( $\mathbf{x}''$ ) refers to the measurement of an image in units of pixels. Continuing the previous example, a graduation of  $\mathbf{x} = 1$  mm might occupy 100 pixels in the image. All image measurements were carried out in the pixel space with uncertainty of  $\pm 1$  pixels and converted to the image space by calibrating the image size with resolution. The results of the image space can then be converted to real space using a magnification factor  $M = \mathbf{x}/\mathbf{x}' = 0.37 \pm 0.01$ .

Figure 6.8(b) shows an example of an image analysis process. We define the origin in the pixel space at the midpoint of the ruler  $R(0,0)$ , which should be aligned with the centreline of the pipe. This definition matches exactly the point  $R$  in Fig. 6.7. For the purpose of the calculation we need to know the angle  $OR$  makes with the horizontal,  $\omega = 10.7 \pm 0.3^\circ$ , which can be calculated if the coordinate of  $R$  is known,



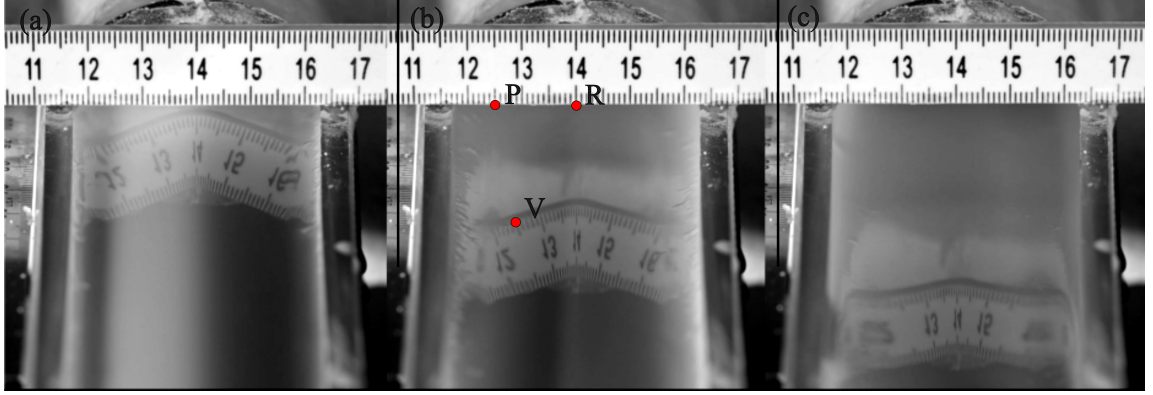


Figure 6.8: Typical progression of the reflection during transient experiment beginning with overfilling (a), fluid height lowering to approximately the midpoint (b) and subsequent underfilling (c). The experiment begins with a level film height ( $\beta = 0$ ). The trough is tilted to a premeasured angle  $\beta$ , such that the point  $O$  falls in the middle of the captured image (here the images are cropped), so that the coordinates of the point  $R$  are known - see Fig. 6.7. Once tilted, fluid begins to drain from the trough resulting in the loss of material and subsequent reduction in the fluid film height. During this process, the concave deflection of the fluid surface is monitored by tracking the surface reflection of the ruler.

which in turn can be calculated from either point  $O$  or  $O'$  using the previously calculated value  $\Delta x$ . Knowing the coordinates of  $S$  and  $R$ , we can calculate the distance  $OR = 670 \pm 3$  mm, which is another key component of the calculation. The next step involves selecting a graduation on the ruler that we will call the object point  $P$ . This point is measured in pixel space by carefully adjusting the mouse in MatLab image viewer app until the meeting point of the increment with the lower edge of the ruler is found. We used a magnified image and a mouse with adjustable DPI (low DPI) to allow for precise measurement in pixel space. The corresponding graduation is found in the reflection, and the measurement of the reflection point  $V$  is taken by finding the intersection of the increment line and the upper reflection edge. With both the object point and the image point defined, the calculation of the fluid surface coordinates  $G' (x'_g, y'_g)$  can be carried out. The coordinates in real

space are found  $\mathbf{G} = M\mathbf{G}'$ . Since we want to know the height of the fluid film (not the distance of the fluid from the ruler), we calculate  $h = H - y_g$ , which gives us the height of the fluid from the reference point of the wall of the centerline of the pipe.

Example height profiles are plotted in Figure 6.9. Profiles were obtained by selecting a frame for which the height of the centreline is equal to the radius of the pipe ( $h(0) \approx r_i$ ) mainly by trial and error. Initially, frames with reflection at the image point were taken, but the height profiles calculated from these were approximately 1.5 mm too low, indicating a systematic error due to uncertainty in the camera positioning and the measurements associated with it. However, these frames were still fairly close and were a good starting point to find the frame that yielded the desired maximum fluid height.

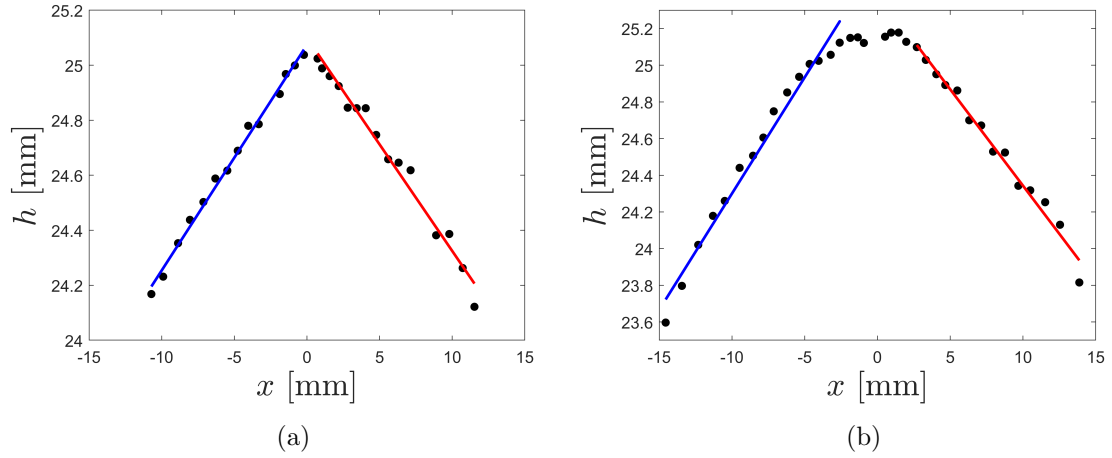


Figure 6.9: Examples of calculated height profiles for (a)  $\phi_v = 0.459 \pm 0.007$  and (b)  $\phi_v = 0.438 \pm 0.007$ . The blue and red lines indicate the linear fits used to calculate  $\alpha_l$  and  $\alpha_r$ , respectively.

## 6.8 $N_2$ Calculation

Having obtained the fluid height profiles, we now need to use them to calculate  $N_2$ . The method used by Keentok et al. [148]; Tanner [36] involved numerical integration of the following expression

$$-N_2 = \frac{1}{x} \int_0^x x \frac{dQ}{dx} dx + O \left( N_2 \left( \frac{h_m}{r_i} \right)^2 \right), \quad (6.19)$$

$$Q(x) = \bar{\rho}gh(x) \cos \beta - \gamma \frac{d^2h(x)}{dx^2}, \quad (6.20)$$

where  $h(x)$  is the measured height profile and  $x$  is the spanwise coordinate from the centreline. The second term in Eq.(6.20) accounts for the effects of surface tension. The surface tension in the inclined trough produces a concave deflection on the fluid surface [149] and, therefore, must be taken into account in the result if we are to isolate the effect of  $N_2$ . The shear stress profile is calculated

$$\sigma_{xy} = \bar{\rho}gx \sin \beta. \quad (6.21)$$

Keentok et al. [148] carries out this calculation by fitting a 4-th order polynomial to the obtained height profile data

$$h(x) = \sum_{i=0}^4 a_i x^i, \quad (6.22)$$

where odd terms measure asymmetry in the profile. This method works when a clear symmetric low-order profile is obtained, but using it without due consideration can introduce spurious relations in the obtained data. Consider Eq.(6.19), ignoring the surface tension effects in Eq.(6.20). If we use  $n$ -th order polynomial term, the obtained relation between  $N_2$  and shear stress will be on the order of  $(n - 1)$

$$\frac{N_2}{\sigma_{xy}} \sim x^{n-1}. \quad (6.23)$$

For example, Kuo and Tanner [150] report parabolic height profiles and use them to retrieve a square power relation between  $N_2$  and shear stress. The height profiles

obtained in the present work are often asymmetric and consist of largely linear slopes with surface tension-induced curvature near the centreline. Fitting a fourth-order polynomial to our data would yield significant odd terms. In addition, if the surface is not accounted for exactly, the 4th-order term will be dominant. Thus, such a parametric fitting would introduce a highly non-linear trend in the relationship between  $N_2$  and shear stress.

To avoid the issues discussed, we adopt the method of Dai et al. [45]. Their work is based on the observation that in suspensions, the shape of the fluid profile is linear with the exception of the centreline, where surface tension introduces a non-linear curvature. Ignoring the curvature induced by surface tension, such profile should result in a zero-th order  $N_2$  dependence on shear stress such that

$$N_2 = \alpha(\phi)\sigma_{xy}, \quad (6.24)$$

where  $\alpha$  is a constant dependent on the volume fraction of the suspension. If we assume that  $h(x)$  is linear based on the measured profiles, the relationship between shear stress and  $N_2$  can be calculated

$$-\alpha = -\frac{N_2}{\sigma_{xy}} = \frac{\pi h_m \cot \beta}{\pi r_i + 2h_m}. \quad (6.25)$$

## 6.9 Ridges and $N_2$

The typical progression in the deflected reflection is shown in Fig. 6.8(a-c). As the pipe is tilted, the fluid level in the pipe decreases, resulting in a downward shift in the reflection during the experiment. Furthermore, the steepness of the reflection decreases during the experiment, due to reducing shear stress, and thus  $N_2$ . Snapshots of the motion that best represented  $h(0) = r_i$  were chosen (Fig. 6.9) for each probed volume fraction to minimise the contributions due to additional stress. We obtained values of  $h_m$  by fitting a linear trend on the left and right sides of the profile (Fig. 6.9 blue and red, respectively) and extrapolated the trends so that  $h_m = h(0) - h(|r_i|)$ . Extrapolating a linear trend has the advantage of removing surface tension effects from the picture, as we ignore the curvature near the centre.

The calculation results in two values for the left ( $\alpha_l$ ) and right ( $\alpha_r$ ) sides of the profile. The results are plotted in Figure 6.10(a), with points indicating the mean value of the right and left sides and error bars indicating the calculated values of the left and right fits.

We report significant negative values of  $N_2$  for all probed volume fractions. We identify a trend of increasing magnitude in  $\alpha$  with increasing volume fraction, with a clear outlier  $\phi_v = 0.459 \pm 0.007$ . In this particular volume fraction, the measured values  $\alpha$  were significantly lower than those measured in any other volume fraction. The calculated fluid surface profile for this concentration is plotted in Fig.6.9(a), where no clear abnormal trend can be seen, with the exception that this is the only volume fraction in which no significant curvature near the centre can be found. Furthermore, repeat measurements with the sample do not alter the result. A hint of what could be causing this spurious result lies in the fact that both left and right fits in this case yield a nearly identical value of  $\alpha$ . In all other measurements, the profiles are asymmetric and  $\alpha_l$  is systematically larger than  $\alpha_r$ . This suggests that the camera alignment changed for this particular measurement. If we also consider that this was the final measurement taken during the investigation, it is highly likely that the camera (or the pipe) was moved from the original position in the setup. This could happen either by the experimental investigator bumping into the tripod, applying too much force to the pipe during loading, or by a third party when the camera was left in the laboratory overnight. In any case, we proceed further by removing this result from any further discussion and highlighting the drawback of a camera setup independently of the trough.

The range of volume fractions ( $0.398 - 0.469$ ) used in this investigation is limited on both ends. Due to the transient nature of our setup, suspensions with a volume fraction lower than  $0.398 \pm 0.007$  have too low a viscosity to perform a measurement due to a low residence time. This could be addressed by modifying the experimental setup, either using a steady-state system, increasing the volume of the trough, or by reducing the angle of inclination. A more fundamental limit occurs for  $\phi_v > 0.469 \pm 0.007$  where DST effects interfere with the measurements. During the course of the experiment, we applied a shear stress of at least 90 Pa, which is significantly higher

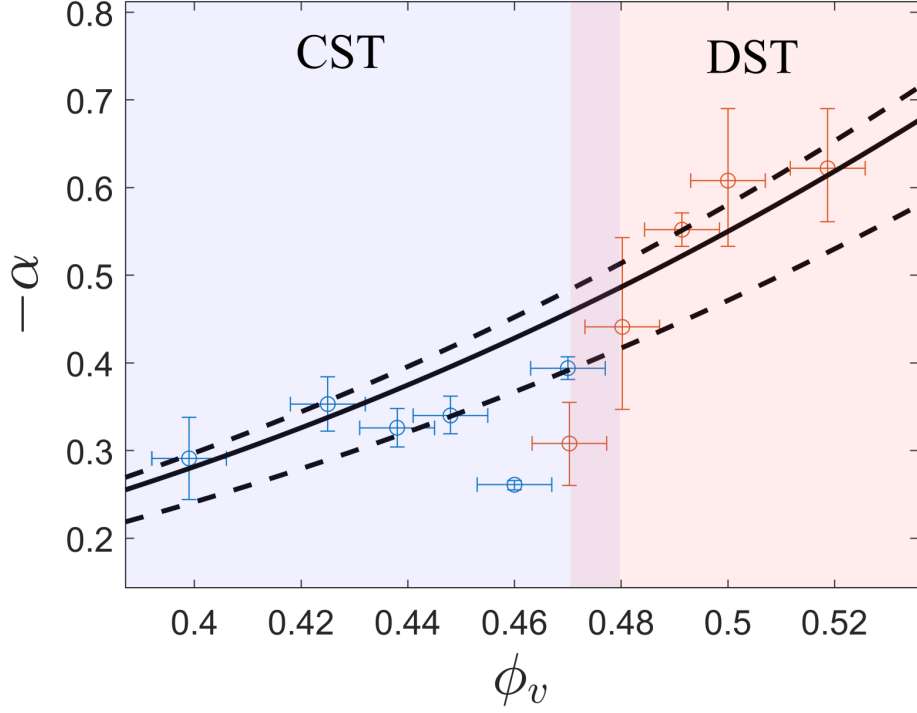


Figure 6.10: Measured values of  $\alpha$  in the cylindrical trough setup (blue) and in the table (red) for a range of volume fractions spanning the CST-DST transition. Solid black line indicates the empirical fit  $\alpha = -4.4\phi_v^3$  with dashed lines indicating upper and lower boundaries of a cubic fit to the present data.

than the measured critical stress for all previously tested DST volume fractions, leading to wave formation in the pipe. In principle, this could be avoided by resorting to measurements at the vanishing angle with increase in volume fraction, but this drastically restricts the range of shear stress over which measurements can be made and completely excludes the range in which DST effects occur.

So far, we have confirmed the presence of significant negative values of  $N_2$  in our corn starch suspensions. This result confirms that corn starch satisfies the key requirement of the previously presented model for the formation of the ridge instability. To test how well the model conforms to the experimental measurements, we use

it to continue measurements of  $\alpha$  in the DST region, using the previously introduced model. Equation(6.15) can be rewritten

$$\alpha = -\frac{1}{\tan(\theta_c)}, \quad (6.26)$$

where  $\theta_c$  indicates the transition from teardrop pattern to the ridge pattern. The results are plotted in Figure 6.10, with data points representing the mean critical angle in the transition range, and error bars indicating the uncertainty associated with the width of the transition region. The results obtained through this method show a clear trend of increasing the magnitude of  $\alpha$  with increasing volume fraction. Interestingly, with the exception of the measurement at  $\phi_v = 0.470 \pm 0.007$ , the data obtained via the model seem to continue the data obtained in the pipe configuration quite well. The table measurements have relatively large uncertainties associated with them. The main source of uncertainty here is the procedure used in the table experiment. At that point, the main goal of the investigation was classifying the patterns across a wide range of conditions, so fairly large increments of angle were needed to probe the entire range of possible angles in a reasonable amount of time. In the future, using smaller increments targeted at the transition boundary would reduce uncertainty. A persistent source of uncertainty would be the classification of patterns as teardrops or ridges. Figure 6.12 shows the transition between teardrops (a) and ridges (b) at  $\phi_v = 0.519 \pm 0.007$ . Classifying patterns near the transition boundaries is difficult, but with some practice key cues in the images can be identified. For example, Fig. 6.12(b) is classified as a ridge pattern due to the formation of teardrop trains separated by depletion zones, a feature missing in Fig.6.12(a). The classification process is also significantly easier when done on the basis of a movie rather than still images.

We compare the results obtained across both experimental setups with the phenomenological relationship for suspensions reported by Dai et al. [45]. Our results appear to generally follow the prediction of Dai et al. [45], however, due to considerable uncertainty and outlier results, only moderate confidence can be ascribed to the correlation. We continue by fitting our data to a third-order power law  $\alpha = -A\phi_v^3$ , with upper and lower bounds (dashed lines in Fig. 6.10) represented by a range of  $A$

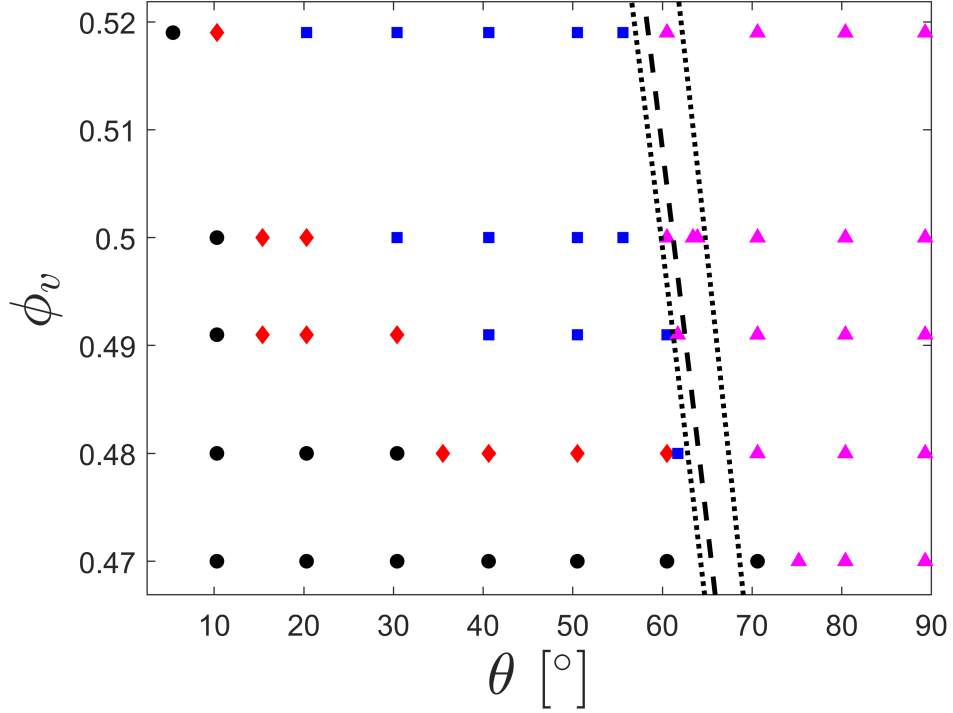


Figure 6.11: Phase diagram of flow patterns observed in the inclined plane experiment. Patterns include: no instabilities (black), roll roll waves (red), teardrops (blue), and ridges (cyan). Major dashed line indicates model prediction for  $A = -4.4$ , with upper and lower boundaries (minor dashed lines) based on the model fit to the data.

between 3.8 and 4.6. Finally, the empirical fit, along with the boundaries obtained by fitting the data, was used to predict the ridge onset critical angle as a function of volume fraction. The resulting transition criterion separates teardrop patterns from ridges remarkably well, with nearly all transitions falling within the region calculated on the basis of the measured  $N_2$  data and the  $N_2$  ridge model (Fig. 6.11). At  $\phi_v = 0.470 \pm 0.007$  the transition in the experiment appears to be higher than the model prediction. This could be due to the fact that we are using a setup with no forcing perturbation, which will naturally lead to overestimation of the the true



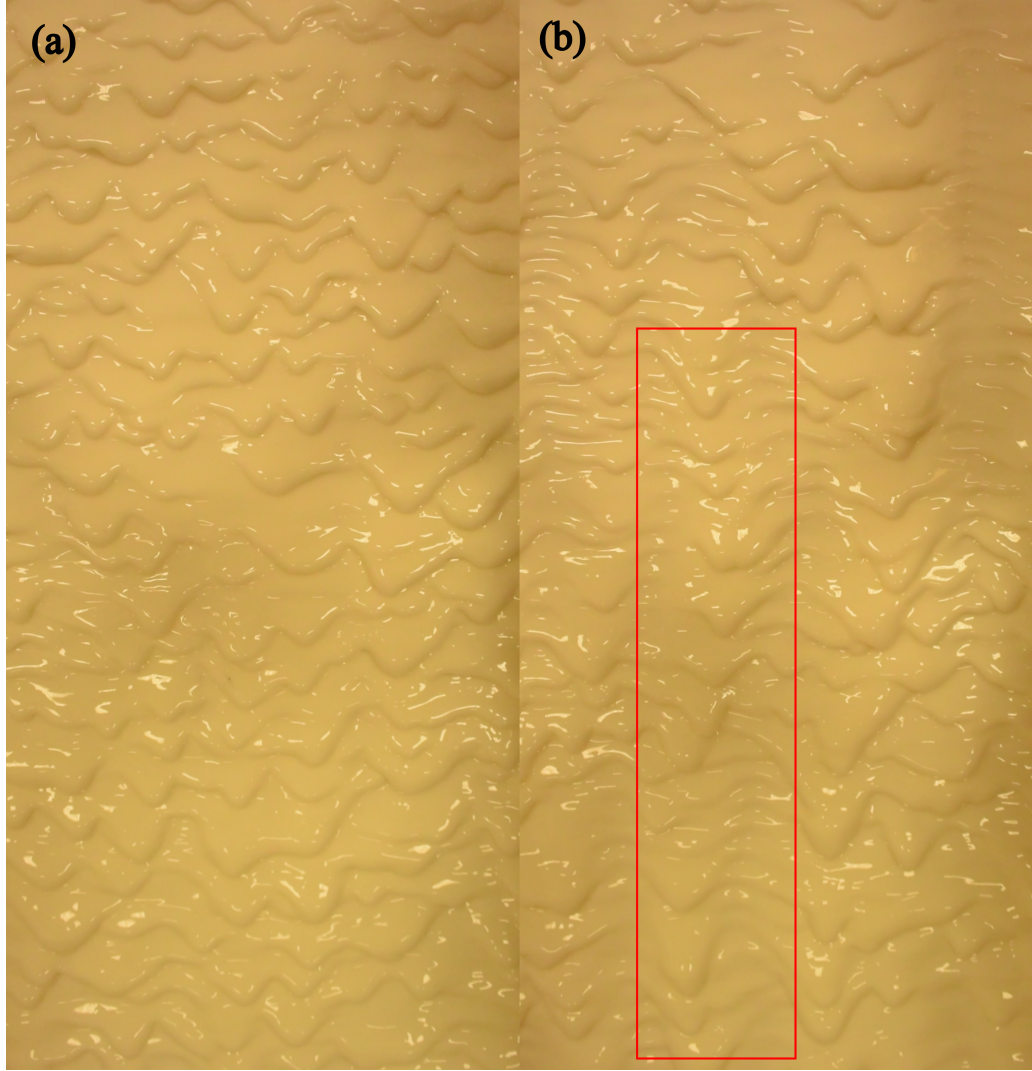


Figure 6.12: An example of teardrop (a) to ridge (b) transition for  $\phi_v = 0.519 \pm 0.007$ . Red guideline (b) highlights formation of a teardrop train, absent in (a).

transition angle. In addition, the imaging technique used in this study is not sensitive enough to measure fine detail of the bifurcation in absence of the primary instability. For all DST volume fraction, the surface is highly disturbed by the roll waves, so that the teardrop-ridge transition can be tracked with ease by tracking the behaviour of the roll waves.

## 6.10 Conclusion

In this chapter, we conducted a thorough investigation of instabilities in inclined free surface flows of DST suspensions. We have designed a transient tilting table setup to study the formation of previously reported roll waves. The onset of roll waves was found to be broadly congruent with the model of Darbois Texier et al. [57], where the increase in the volume fraction corresponded to the decrease in the critical onset basal stress. The presence of roll waves was reported only for DST volume fractions, which is in agreement with the model of diverging onset stress for volume fractions approaching the CST-DST transition volume fraction. Unlike the previous work on the primary instability, we were able to study a wide range of applied inclination angles. This approach revealed rich pattern formation dynamics with properties different from typical DST roll waves. Increases in the angle past the critical onset angle resulted in deformation of the roll wavefront, leading to breaking of spanwise symmetry and formation isolated roll waves elongated in the flow direction (teardrops). An additional increase in the angle produced another distinct pattern, consisting of long ridges of fluid, unbroken in the flow direction, separated by zones of fluid depletion along the vorticity direction. In particular, this ridge pattern formed for both the CST and the DST volume fractions, with a smooth ridge surface in the CST regime and typical roll waves forming on the surface of the DST ridges. This observation was interpreted as plausible evidence of an instability mechanism separate from the primary instability and potentially independent of the phenomenology of DST, the formation of the complex pattern being the result of a linear combination of the two mechanisms.

A possible instability mechanism for the formation of ridges was identified as the effect of the second normal stress difference ( $N_2$ ). In this work, we adopted and sought to test the instability model developed during collaboration with Xiong et al. [147], which related the critical onset angle for the ridges to the ratio of  $N_2$  and the shear stress ( $\alpha = N_2/\sigma_{xy}$ ). The model assumed rate-independence in this ratio and excluded direct shear-thickening effects. To test the proposed model, we developed

a trough setup to directly measure the presence and magnitude of  $N_2$  in corn starch suspensions. Our experimental setup broadly followed the previous literature, with the main difference in our measurements taking place in a transient setup rather than a steady state. To address the unique challenges associated with the transient mode, a specific camera placement was developed and used in conjunction with the optical method of Keentok et al. [148] to track the motion of surface reflection and measure the fluid height profile within the trough.

Across the range of volume fractions tested in the trough, all produced concave deflection in surface reflection, indicating significant negative values of  $N_2$ . The presence of negative values of  $N_2$  satisfied the minimal requirement of the model for predicting the instability of the ridge. The measurement of  $\alpha$  was performed following the work of Dai et al. [45], where the observed linear slopes of the fluid profile were used to estimate the total deflection induced by  $N_2$ . The measured values were compared with the phenomenological fit reported by Dai et al. [45], which revealed moderate agreement. The reported values were in approximate proximity to the empirical fit. The main source of uncertainty was identified in camera positioning and evidence of an outlier measurement caused by the change in camera position was presented. In future work, measurements could be reported with greatly enhanced precision by attaching the camera directly to the trough, thus removing the uncertainty associated with changes in camera alignment.

A fundamental limitation in the trough setup was identified with onset of roll waves spoiling the optical measurements for DST volume fractions. To continue the measurements in the DST regime, the model was used to calculate the value of  $\alpha$  based on the teardrop-ridge transition angle. These results showed a clear trend with an increasing magnitude of  $\alpha$  with increasing volume fraction and a reasonably good agreement with the empirical fit. In particular, the results obtained in the table were generally in congruence with the results obtained in the trough. This suggests that there is no significant transition in the relationship between shear stress and  $N_2$  at the onset of DST effects, although the confidence here is limited by significant uncertainty in the measurements. For all DST volume fractions, the source of uncertainty lies in the experimental procedure. The experimental setup is

well suited for the measurements and uncertainty could be limited by repeating the measurements with lower increments of angle. However, significant changes in the identification of ridge instability in CST volume fractions would be required, as the current optical imaging method is not sufficiently sensitive when applied to nearly flat surfaces found in the CST transition, leading to a significant overestimation of the critical angle (and thus underestimation of  $\alpha$ ).

By combining the empirical fit of Dai et al. [45] with the model for ridge instability, predicted transition line was plotted in the  $\phi_v - \theta$  phase diagram. The prediction yielded an excellent separation between teardrops and ridges. From this we conclude that the dilatancy associated with the granular nature of corn starch suspensions is responsible for the secondary pattern formation reported in this work. Based on the results of the present work, we speculate that inclined free surface flows, either a plane or a conjunction of a plane and a trough, could be used in the future to characterise two out of three viscometric functions for dense suspensions. By tracking the onset properties of primary instabilities, information about rate dependence in viscosity could be acquired, while the secondary instability allows for inference of the second normal stress difference material properties. However, future work on refinement of the experimental setup is required, such as using more advanced optical profilometry techniques [44].

# Chapter 7

## Conclusion

### 7.1 SPH, Flow Curves, and Rheochaos

In Chapter 2, we presented the first microstructural implementation of DST in SPH. In doing so, we observed that in the presence of negative gradients in the WC model, the local microstructure evolution contains an inherent spatial instability mechanism. The so-called 'stress-splitting' was recognised as a potential pathway to formation of spatial heterogeneity, but it alone could not produce continuous spatial patterns. To control the formation of patterns, a non-local term was introduced, which would set the characteristic length scale in the system. The result was the formation of two SLPs at the wall boundaries, similar to the ones observed in the BSM measurements. Although it seemed our work was on the right path, all the solutions were still exactly periodic.

In Chapter 3, we build on the previous results by engaging in a detailed analysis of the relevant time and length scales in the hope of uncovering the conditions required for rheochaos. By including non-local effects, we ended up with three distinct dynamic processes: local microstructure dynamics, global system-inertia dynamics, and the dynamics of spatial pattern formation. The key observation came from considering the BSM measurements of [91] - in stress controlled experiments, the SLPs dissipated in each oscillatory cycle, whereas in our simulations they persisted. How-

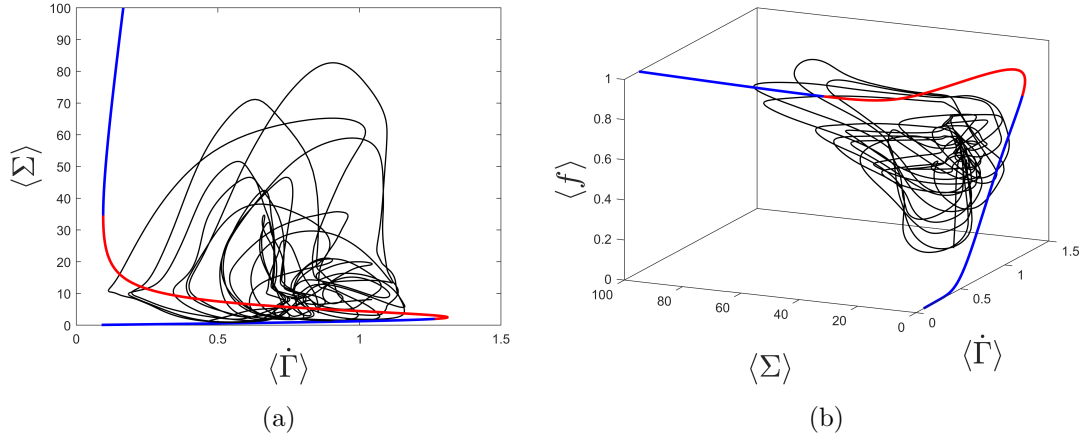


Figure 7.1: Chaotic trajectories in (a) 2D phase space and (b) 3D phase space.

ever, by careful consideration of the balance in the local and non-local elements of the microstructure, it became apparent that our model should be capable of replicating this phenomenology if a sufficiently large difference in the frictional and frictionless viscosity is allowed. Once the viscosity ratio was modified to reflect a more realistic value of typical DST fluids, not only was SLP dissipation achieved, but the measured shear rate signals were found to be in excellent agreement with those of Rathee et al. [90]. Moreover, these signals were no longer strictly periodic; in each cycle the attained values were noticeably different. By adjusting the system-inertia timescales, completely chaotic signals were found (Fig.7.1). In our model, rheochaos arises because the spatial configuration of microstructure in the domain decides the amount of excess stress produced by the presence of microstructure.

In Chapter 4, we tested our model by comparing it with common features of DST fluids observed in experiments. Compared to simple shear rheology, our model reproduced nearly all features of typical flow curves obtained in experiments. The typical challenge of measuring a flow curve that fits the WC model was ascribed to the fact that the rheometer is averaging over a chaotic signal, not a steady state. We then turned to the question of how such difficulties could be practically overcome. Interestingly, when testing for inertial effects, our model predicted a unique effect of

confinement consistent with recent experiments of Hu et al. [139]. When extended to the problem of a channel flow, rheochaos proceeded in a manner very similar to that measured experimentally in a pipe flow by Bougouin et al. [60].

In summary, we formulated a very simple, yet dynamically very rich, model which reproduced the key components of rheochaos. From our work, we can conclude that the key elements required for rheochaos include negative gradients of the flow curve ( $d\dot{\gamma}/d\sigma < 0$ ), rate-dependent local formation of the microstructure, and stress-diffusive nonlocality. In future work, it would be interesting to see how different formulations of microstructure evolution and nonlocality might fit these criteria. The work of Gillissen et al. [27] is an interesting approach to microstructure evolution, and developing a coarse-grained first-principle formulation for the evolution of the tensorial microstructure would be key to fully understanding the dynamics beyond a 2D picture. At the same time, migration of particles is an attractive candidate for the non-local term, as it would satisfy the stress diffusivity condition and potentially allow for reproducing the particle migration effects observed in rheochaotic flows. From a technical standpoint, generalising our implementation into three dimensions would be hugely advantageous even with a scalar model. It would allow for probing of vorticity effects, which are certainly present in the experiments. However, such an implementation is not simple, as it must tackle the challenges associated with the high computational cost of simulating DST fluids. The fact that rheochaos requires large viscosity ratios makes the simulation of realistic DST materials problematic, which could easily compound with the extra computational costs incurred by going to a 3D implementation without appropriate considerations of code optimisation.

## 7.2 Free Surface Flows

In Chapters 6 and 7 we presented an experimental investigation of free surface DST flows. We began by assessing the practical challenges associated with the use of cornstarch; primarily its ageing behaviour and the uncertainty involved in its moisture content. The influence of inertia on the oscillation amplitude resulted in trends

similar to those obtained in our rheochaotic simulations. At the same time, confinement effects were probed, but no strong effects were found. This is likely because the gap height used in our investigation was not small enough to induce the confinement effects seen in the simulations and the work of Hu et al. [139] (our smallest gap height was almost twice as large as the one used in their work).

In Chapter 7, we turned to the inclined-plane flow of cornstarch and found a new mode of instability beyond the typical roll waves. The instability consisted of ridge formation along the vorticity direction. The presence of  $N_2$  was identified as a potential mechanism, based on the model developed in collaboration with Xiong et al. [147]. To verify this, a tilted trough setup was designed and optical measurements of the deflected surface were made. Despite the unique challenges associated with our transient version of the experiment, our measurements revealed significant negative values of  $N_2$ , with moderate agreement with the empirical fit of Dai et al. [45]. To overcome the practical limitations of the through experiment in the context of DST fluids, we extended our measurements into the DST range of volume fractions by applying the  $N_2$  instability model to the critical transition angles measured in the plane flow experiment. In particular, the values calculated in this manner seemed to continue trend measurement in the CST regime, in good agreement with the empirical fit of Dai et al. [45]. This implies that the behaviour of  $N_2$  is not affected by the transition from CST to DST.

Our experimental work suggests that inclined free surface flow could be used as an effective tool to gain insight into the rheology of DST materials in ways conventional techniques cannot. By tracking the emergence of roll waves, information on shear thickening properties can be obtained [57], while monitoring the onset of ridge instability offers information on the second normal stress difference. The main limitation of our work was the large degree of uncertainty. In future work, this could be addressed by simple (but time-consuming) refinements in the experimental setup (i.e., installing the camera on the trough) and experimental procedure (repeating table measurements with higher angle resolution). With respect to roll waves, it would be interesting to repeat the measurements with varying film heights to see if the relationship between wall stress and volume fraction collapses as predicted by



Darbois Texier et al. [57]. In terms of ridges, repeating measurements with different film heights would also be interesting, since the current model predicts no dependence on the wall stress, so while the critical angle for the roll waves should vary with changes in film height, the critical angle for ridge formation should stay the same.

# Appendix A

## Numerical Simulations of Spatiotemporal Instabilities and Pattern Formation: Further Results

### A.1 Fluid Inertia

To investigate effects of fluid inertia we alter the flow curve by reducing  $\phi^0 : 10 \rightarrow 0.90$  and  $\phi^m : 0.562 \rightarrow 0.55$ , effectively increasing both frictionless and frictional viscosities. This results in a reduction of  $H : 583 \rightarrow 483$ , to facilitate higher computational cost while remaining in large viscosity contrast parameter space. Finally, the value of the diffusion coefficient  $\alpha : 2 \times 10^{-7} \rightarrow 10^{-8}$  is reduced to compensate for reduction in shear rate and maintain similar balance of local and non-local effects. The resulting range of  $Re$  here is  $2 \times 10^{-4} < Re < 0.13$ .

The results for high system inertia ( $k_p = 0.01$ ) are presented in Fig. [A.1](#). For both applied stresses, oscillations retain the pattern of high shear rate inducing formation of spatially heterogeneous microstructure, which in turn facilitates spikes in stress and deceleration of the upper plate. The main difference consist of ‘softer’

deceleration phase and less pronounced (but still present) aperiodicity of the signals. For low system inertia ( $k_p = 1$ ) in Fig [A.2](#) significant differences due to reduced inertia include vastly reduced relative amplitude of oscillations. Interestingly, apparent oscillations retain their aperiodic 'noisy' appearance.

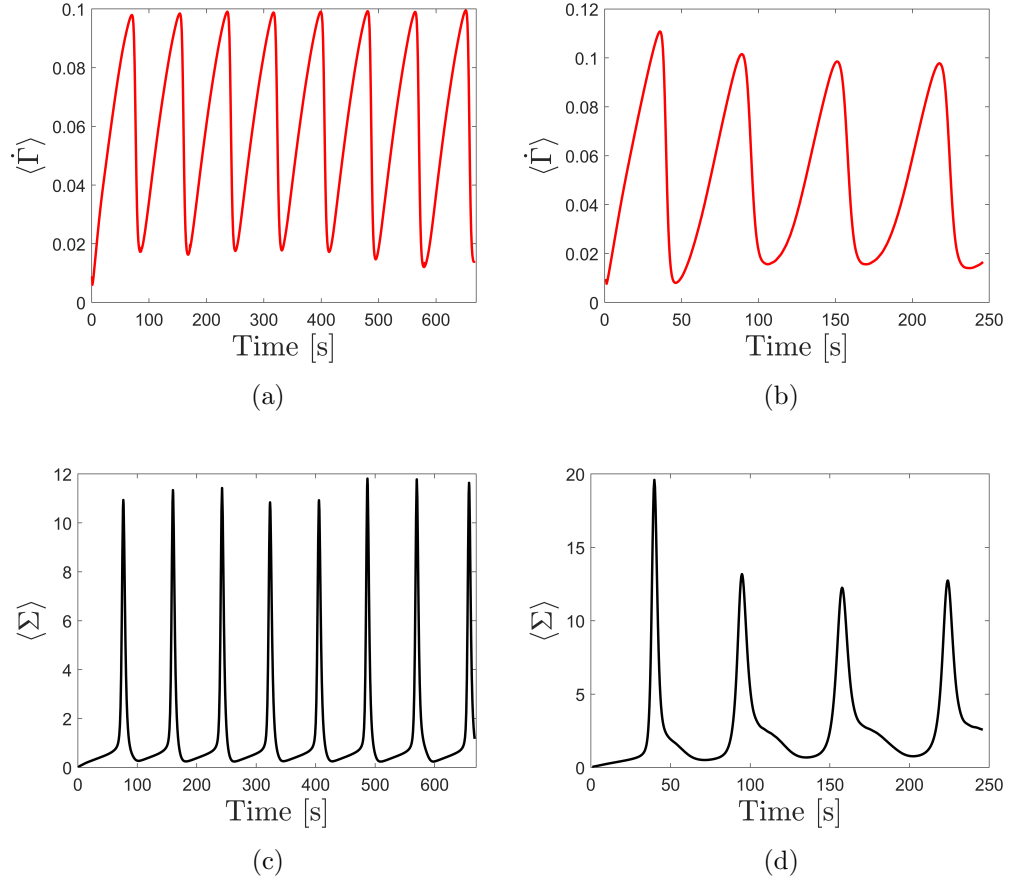


Figure A.1: Dimensionless shear rate (red) and stress (black) for (a,c)  $\Sigma_E = 1.40$  and (b,d)  $\Sigma_E = 2.55$ .  $k_p = 0.01$ .

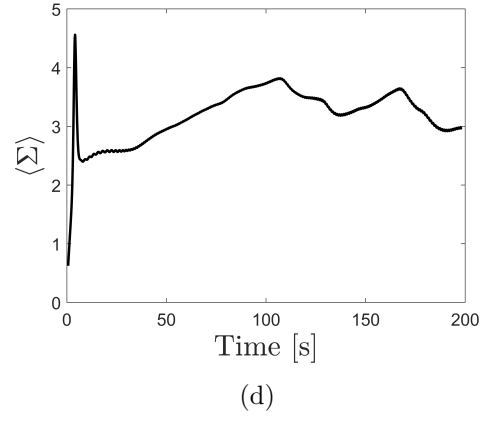
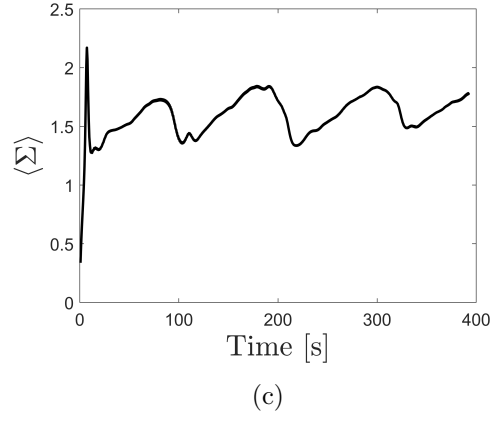
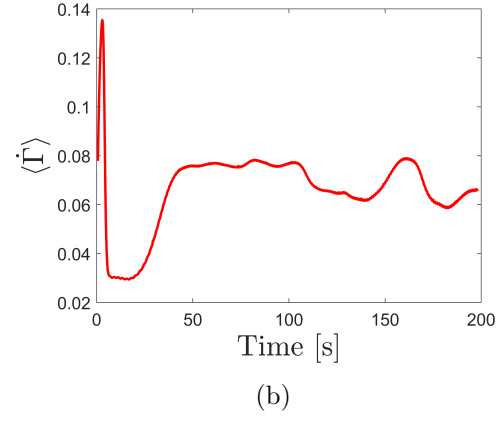
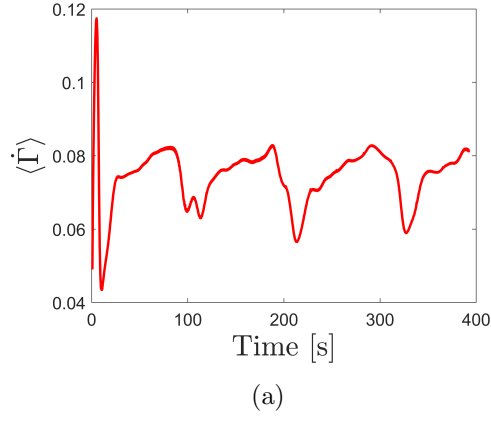


Figure A.2: Dimensionless shear rate (red) and stress (black) for (a,c)  $\Sigma_E = 1.40$  and (b,d)  $\Sigma_E = 2.55$ .  $k_p = 1$ .

Parameter	Value	Units
Particle volume fraction, $\phi$	0.540	-
Frictional divergence volume fraction, $\phi^{\text{m}}$	0.562	-
Frictionless divergence volume fraction, $\phi^0$	0.692	-
Solvent viscosity, $\eta_{\text{s}}$	0.001	Pa s
Characteristic stress scale, $\sigma^*$	0.005	Pa
Microstructural rate parameter, $k_{\text{f}}$	1	-
System inertia parameter, $k_{\text{p}}$	0.01–1	$\text{m s}^{-2} \text{Pa}^{-1}$
Microstructural diffusion parameter, $\alpha$	$10^{-5}$	$\text{m}^2 \text{s}^{-1}$
Gap height, $h$	0.01 or 0.02	m
Domain length, $l$	0.01	m
Fluid density, $\rho$	1000	$\text{kg m}^{-3}$
Stress set-point, $\Sigma_{\text{E}}$	0.0025–0.002875	Pa

Table A.1: Dominant non-locality parameters

Parameter	Value	Units
Particle volume fraction, $\phi$	0.540	-
Frictional divergence volume fraction, $\phi^{\text{m}}$	0.562	-
Frictionless divergence volume fraction, $\phi^0$	0.692	-
Solvent viscosity, $\eta_s$	0.001	Pa s
Characteristic stress scale, $\sigma^*$	0.005	Pa
Microstructural rate parameter, $k_f$	0.1–10	-
System inertia parameter, $k_p$	0	$\text{m s}^{-2} \text{Pa}^{-1}$
Microstructural diffusion parameter, $\alpha$	0	$\text{m}^2 \text{s}^{-1}$
Gap height, $h$	0.01	m
Domain length, $l$	0.01	m
Fluid density, $\rho$	1000	$\text{kg m}^{-3}$
Stress set-point, $\Sigma_E$	0.00625	Pa

Table A.2: Vanishing non-locality parameters

Parameter	Value	Units
Particle volume fraction, $\phi$	0.540	-
Frictional divergence volume fraction, $\phi^{\text{m}}$	0.562	-
Frictionless divergence volume fraction, $\phi^0$	0.692	-
Solvent viscosity, $\eta_{\text{s}}$	0.001	Pa s
Characteristic stress scale, $\sigma^*$	0.005	Pa
Microstructural rate parameter, $k_{\text{f}}$	20	-
System inertia parameter, $k_{\text{p}}$	1	$\text{m s}^{-2} \text{Pa}^{-1}$
Microstructural diffusion parameter, $\alpha$	$10^{-10}$ – $10^{-5}$	$\text{m}^2 \text{s}^{-1}$
Gap height, $h$	0.01	m
Domain length, $l$	0.03	m
Fluid density, $\rho$	1000	$\text{kg m}^{-3}$
Stress set-point, $\Sigma_{\text{E}}$	0.00625	Pa

Table A.3: Moderate non-locality parameters



Parameter	Value	Units
Particle volume fraction, $\phi$	0.540	-
Frictional divergence volume fraction, $\phi^{\text{m}}$	0.562	-
Frictionless divergence volume fraction, $\phi^0$	10	-
Solvent viscosity, $\eta_{\text{s}}$	0.00158	Pa s
Characteristic stress scale, $\sigma^*$	0.0005	Pa
Microstructural rate parameter, $k_{\text{f}}$	20	-
System inertia parameter, $k_{\text{p}}$	0.01 or 1	$\text{m s}^{-2} \text{Pa}^{-1}$
Microstructural diffusion parameter, $\alpha$	$2 \times 10^{-7}$	$\text{m}^2 \text{s}^{-1}$
Gap height, $h$	0.01	m
Domain length, $l$	0.03	m
Fluid density, $\rho$	1000	$\text{kg m}^{-3}$
Stress set-point, $\Sigma_{\text{E}}$	0.0005–0.025	Pa

Table A.4: High viscosity ratio parameters

Parameter	Value	Units
Particle volume fraction, $\phi$	0.54	-
Frictional divergence volume fraction, $\phi^m$	0.55	-
Frictionless divergence volume fraction, $\phi^0$	0.90	-
Solvent viscosity, $\eta_s$	0.00158	Pa s
Characteristic stress scale, $\sigma^*$	0.0005	Pa
Microstructural rate parameter, $k_f$	20	-
System inertia parameter, $k_p$	0.01 or 1	$\text{m s}^{-2} \text{Pa}^{-1}$
Microstructural diffusion parameter, $\alpha$	$2 \times 10^{-7}$	$\text{m}^2 \text{s}^{-1}$
Gap height, $h$	0.01	m
Domain length, $l$	0.03	m
Fluid density, $\rho$	1000	$\text{kg m}^{-3}$
Stress set-point, $\Sigma_E$	0.0007 or 0.001275	Pa

Table A.5: Low fluid inertia parameters

The values of  $\phi$ ,  $\phi^m$ , and  $\phi^0$  were chosen according to the values obtained by Baumgarten and Kamrin [26] by fitting the Wyart-Cates model to the data available in the literature for various experimental samples. The solvent parameters were matched with water, with increases in viscosity in some cases being comparable to using water-glycerol mixtures. The dynamic properties of microstructural formation, diffusion, and system inertia for experimental system are less readily available. These parameters were the subject of this study, with the resulting flow fields being compared to the experimental measurements across a range of the dynamic parameter space.

## Appendix B

### Stress Splitting Diagram

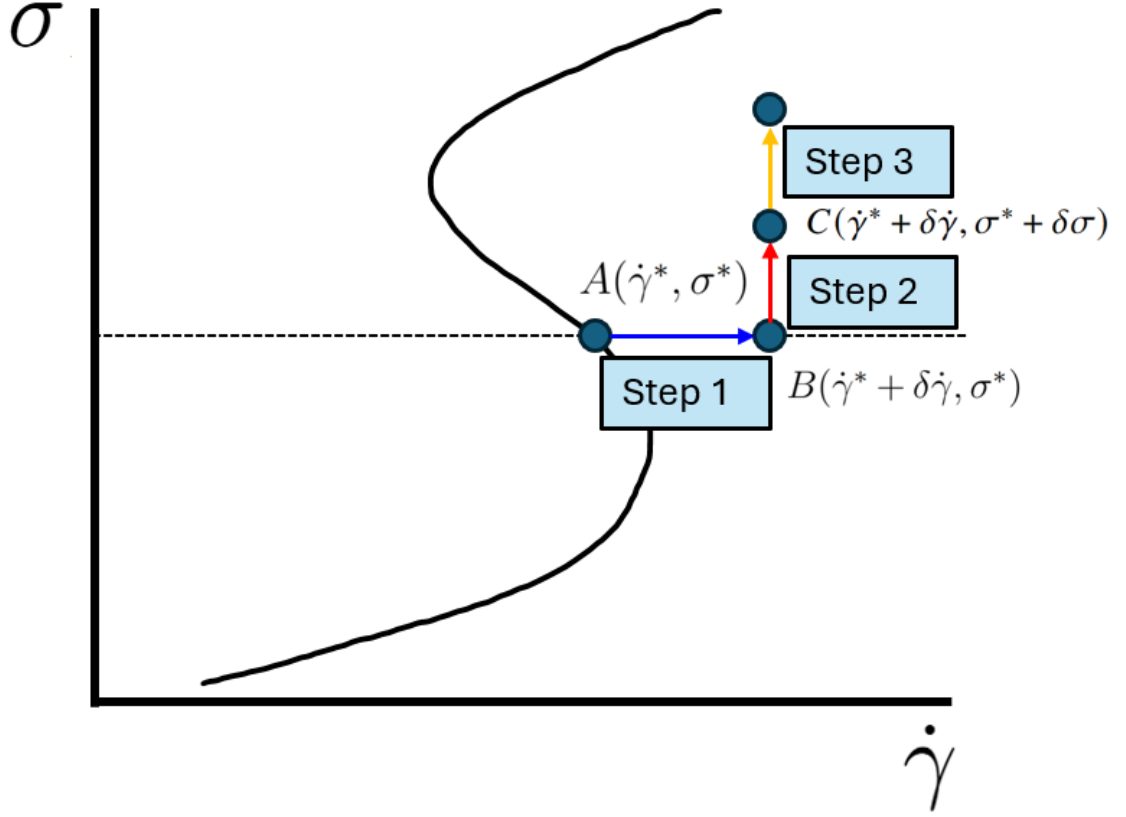


Figure B.1: Schematic diagram of the stress splitting process. All particles begin on point  $A$ , which lies on the steady state for the applied stress (dashed horizontal). In step 1, a particle receives perturbation in shear rate and moves to point  $B$ . At point  $B$ , the particle has the same stress, but higher shear rate. This implies that viscosity, and thus  $f$ , has decreased. Since before the perturbation  $\hat{f} - f = 0$ , we now know that  $\hat{f} - f > 0$  and so  $df/dt > 0$  at point  $B$ . In step 2,  $f$  increases due to the positive gradient  $df/dt$  so the viscosity increases. Since shear rate has not changed, an increase in viscosity is reflected in an increase in stress, moving the particle to point  $C$ . Finally, at point  $C$ , although  $f$  has increased, so has the value of  $\hat{f}(\sigma)$  since the stress increased. This ensures that  $\hat{f} - f$  remains positive, and so the steps 2 and 3 will repeat until we reach the upper branch where  $df/dt = 0$  by definition.

# Bibliography

- [1] Zhiqi Chen, Yunfeng Chao, Weihua Li, Gordon G. Wallace, Tim Bussell, Jie Ding, and Caiyun Wang. Abuse-tolerant electrolytes for lithium-ion batteries. *Advanced Science*, 8(11):2003694, 2021. doi: <https://doi.org/10.1002/advs.202003694>. URL <https://onlinelibrary.wiley.com/doi/abs/10.1002/advs.202003694>.
- [2] Qianqian Huang, Xin Liang, Bing Liu, and Huaxia Deng. Research progress of shear thickening electrolyte based on liquid–solid conversion mechanism. *Batteries*, 9(7), 2023. ISSN 2313-0105. doi: 10.3390/batteries9070384. URL <https://www.mdpi.com/2313-0105/9/7/384>.
- [3] Neil Y.C. Lin, Christopher Ness, Michael E. Cates, Jin Sun, and Itai Cohen. Tunable shear thickening in suspensions. *Proceedings of the National Academy of Sciences*, 113(39):10774–10778, 2016. doi: 10.1073/pnas.1608348113. URL <https://www.pnas.org/doi/abs/10.1073/pnas.1608348113>.
- [4] Michael J. Hertaeg, Suzanne M. Fielding, and Dapeng Bi. Discontinuous shear thickening in biological tissue rheology. *Phys. Rev. X*, 14:011027, Feb 2024. doi: 10.1103/PhysRevX.14.011027. URL <https://link.aps.org/doi/10.1103/PhysRevX.14.011027>.
- [5] Haiqing Liu, Kunkun Fu, Xiaoyu Cui, Huixin Zhu, and Bin Yang. Shear thickening fluid and its application in impact protection: A review. *Polymers (Basel)*, 15(10), May 2023.

- [6] Endao Han, Nicole M. James, and Heinrich M. Jaeger. Stress controlled rheology of dense suspensions using transient flows. *Phys. Rev. Lett.*, 123:248002, 2019.
- [7] N. J. Balmforth, J. W. M. Bush, and R. V. Craster. Roll waves on flowing cornstarch suspensions. *Phys. Lett. A*, 338(6):479–484, 2005. ISSN 0375-9601.
- [8] Michiel Hermes, Ben M. Guy, Wilson C. K. Poon, Guilhem Poy, Michael E. Cates, and Matthieu Wyart. Unsteady flow and particle migration in dense, non-brownian suspensions. *J. Rheol.*, 60(5):905–916, 2016.
- [9] S.H. Strogatz. *Nonlinear Dynamics and Chaos: With Applications to Physics, Biology, Chemistry, and Engineering*. CRC Press, 2018. ISBN 9780429961113. URL <https://books.google.co.uk/books?id=A0paDwAAQBAJ>.
- [10] Vladimir A. Kuznetsov, Iliya A. Makalkin, Mark A. Taylor, and Alan S. Perelson. Nonlinear dynamics of immunogenic tumors: Parameter estimation and global bifurcation analysis. *Bulletin of Mathematical Biology*, 56(2): 295–321, 1994. ISSN 0092-8240. doi: [https://doi.org/10.1016/S0092-8240\(05\)80260-5](https://doi.org/10.1016/S0092-8240(05)80260-5). URL <https://www.sciencedirect.com/science/article/pii/S0092824005802605>.
- [11] Arthur T. Winfree. Spiral waves of chemical activity. *Science*, 175(4022):634–636, 1972. doi: 10.1126/science.175.4022.634. URL <https://www.science.org/doi/abs/10.1126/science.175.4022.634>.
- [12] B. Ermentrout. An adaptive model for synchrony in the firefly *pteroptyx malacca*e. *Journal of Mathematical Biology*, 29(6):571–585, Jun 1991. ISSN 1432-1416. doi: 10.1007/BF00164052. URL <https://doi.org/10.1007/BF00164052>.
- [13] Arthur T. Winfree. *The Firefly Machine*, pages 277–284. Springer Berlin Heidelberg, Berlin, Heidelberg, 1980. ISBN 978-3-662-22492-

2. doi: 10.1007/978-3-662-22492-2\_12. URL [https://doi.org/10.1007/978-3-662-22492-2\\_12](https://doi.org/10.1007/978-3-662-22492-2_12).
- [14] John Buck. Synchronous rhythmic flashing of fireflies. ii. *The Quarterly Review of Biology*, 63(3):265–289, 1988. ISSN 00335770, 15397718. URL <http://www.jstor.org/stable/2830425>.
- [15] V. Fairén and M. G. Velarde. Time-periodic oscillations in a model for the respiratory process of a bacterial culture. *Journal of Mathematical Biology*, 8(2):147–157, Sep 1979. ISSN 1432-1416. doi: 10.1007/BF00279718. URL <https://doi.org/10.1007/BF00279718>.
- [16] J J Tyson. Modeling the cell division cycle: cdc2 and cyclin interactions. *Proc Natl Acad Sci U S A*, 88(16):7328–7332, August 1991.
- [17] William Ogilvy Kermack, A. G. McKendrick, and Gilbert Thomas Walker. A contribution to the mathematical theory of epidemics. *Proceedings of the Royal Society of London. Series A, Containing Papers of a Mathematical and Physical Character*, 115(772):700–721, 1927. doi: 10.1098/rspa.1927.0118. URL <https://royalsocietypublishing.org/doi/abs/10.1098/rspa.1927.0118>.
- [18] Steven H. Strogatz. *Analysis of Models*, pages 148–182. Springer Berlin Heidelberg, Berlin, Heidelberg, 1986. ISBN 978-3-642-46589-5. doi: 10.1007/978-3-642-46589-5\_6. URL [https://doi.org/10.1007/978-3-642-46589-5\\_6](https://doi.org/10.1007/978-3-642-46589-5_6).
- [19] H. A. Stone, Ali Nadim, and Steven H. Strogatz. Chaotic streamlines inside drops immersed in steady stokes flows. *Journal of Fluid Mechanics*, 232: 629–646, 1991. doi: 10.1017/S002211209100383X.
- [20] P. Gray and S. K. Scott. Sustained oscillations and other exotic patterns of behavior in isothermal reactions. *The Journal of Physical Chemistry*, 89(1): 22–32, Jan 1985. ISSN 0022-3654. doi: 10.1021/j100247a009. URL <https://doi.org/10.1021/j100247a009>.



- [21] D. Ludwig, D. D. Jones, and C. S. Holling. Qualitative analysis of insect outbreak systems: The spruce budworm and forest. *Journal of Animal Ecology*, 47(1):315–332, 1978. ISSN 00218790, 13652656. URL <http://www.jstor.org/stable/3939>.
- [22] A.T. Winfree. *When Time Breaks Down: The Three-dimensional Dynamics of Electrochemical Waves and Cardiac Arrhythmias*. Princeton University Press, 1987. ISBN 9780691024028. URL <https://books.google.co.uk/books?id=zpuFQgAACAAJ>.
- [23] Julia Slingo and Tim Palmer. Uncertainty in weather and climate prediction. *Philos Trans A Math Phys Eng Sci*, 369(1956):4751–4767, December 2011.
- [24] Mitchell J. Feigenbaum. Quantitative universality for a class of nonlinear transformations. *Journal of Statistical Physics*, 19(1):25–52, Jul 1978. ISSN 1572-9613. doi: 10.1007/BF01020332. URL <https://doi.org/10.1007/BF01020332>.
- [25] Irving R. Epstein. Predicting complex biology with simple chemistry. *Proceedings of the National Academy of Sciences*, 103(43):15727–15728, 2006. doi: 10.1073/pnas.0608026103. URL <https://www.pnas.org/doi/abs/10.1073/pnas.0608026103>.
- [26] Aaron S. Baumgarten and Ken Kamrin. A general constitutive model for dense, fine-particle suspensions validated in many geometries. *Proc. Natl. Acad. Sci. USA*, 116(42):20828–20836, 2019.
- [27] J. J. J. Gillissen, C. Ness, J. D. Peterson, H. J. Wilson, and M. E. Cates. Constitutive model for shear-thickening suspensions: Predictions for steady shear with superposed transverse oscillations. *J. Rheol.*, 64(2):353–365, 2020.
- [28] G. K. Batchelor. *The Physical Properties of Fluids*, page 1–70. Cambridge Mathematical Library. Cambridge University Press, 2000.

- [29] G. K. Batchelor. *Kinematics of the Flow Field*, page 71–130. Cambridge Mathematical Library. Cambridge University Press, 2000.
- [30] G. K. Batchelor. *Equations Governing the Motion of a Fluid*, page 131–173. Cambridge Mathematical Library. Cambridge University Press, 2000.
- [31] Morton M. Denn and Jeffrey F. Morris. Rheology of non-brownian suspensions. *Annu. Rev. Chem. Biomol. Eng.*, 5(1):203–228, 2014.
- [32] Élisabeth Guazzelli and Olivier Pouliquen. Rheology of dense granular suspensions. *Journal of Fluid Mechanics*, 852:P1, 2018. doi: 10.1017/jfm.2018.548.
- [33] A.C. Pipkin. *Lectures on Viscoelasticity Theory*. Applied Mathematical Sciences. Springer New York, 2012. ISBN 9781461599708. URL <https://books.google.co.uk/books?id=1BcDCAAQBAJ>.
- [34] O. Maklad and R.J. Poole. A review of the second normal-stress difference; its importance in various flows, measurement techniques, results for various complex fluids and theoretical predictions. *Journal of Non-Newtonian Fluid Mechanics*, 292:104522, 2021. ISSN 0377-0257. doi: <https://doi.org/10.1016/j.jnnfm.2021.104522>. URL <https://www.sciencedirect.com/science/article/pii/S0377025721000458>.
- [35] K. WEISSENBERG. A continuum theory of rheological phenomena. *Nature*, 159(4035):310–311, Mar 1947. ISSN 1476-4687. doi: 10.1038/159310a0. URL <https://doi.org/10.1038/159310a0>.
- [36] R. I. Tanner. Some Methods for Estimating the Normal Stress Functions in Viscometric Flows. *Transactions of The Society of Rheology*, 14(4):483–507, 12 1970. ISSN 0038-0032. doi: 10.1122/1.549175. URL <https://doi.org/10.1122/1.549175>.
- [37] A. Einstein. Berichtigung zu meiner arbeit: eine neue bestimmung der moleküldimensionen”. *Annalen der Physik*, 339(3):591–592, 1911. doi: <https://doi.org/10.1002/andp.19113390301>.

//doi.org/10.1002/andp.19113390313. URL <https://onlinelibrary.wiley.com/doi/abs/10.1002/andp.19113390313>.

- [38] G. K. Batchelor and J. T. Green. The determination of the bulk stress in a suspension of spherical particles to order  $c^2$ . *Journal of Fluid Mechanics*, 56(3):401–427, 1972. doi: 10.1017/S0022112072002435.
- [39] G. K. Batchelor and J. T. Green. The hydrodynamic interaction of two small freely-moving spheres in a linear flow field. *Journal of Fluid Mechanics*, 56(2): 375–400, 1972. doi: 10.1017/S0022112072002927.
- [40] Romain Mari, Ryohei Seto, Jeffrey F. Morris, and Morton M. Denn. Shear thickening, frictionless and frictional rheologies in non-Brownian suspensions. *J. Rheol.*, 58(6):1693–1724, 2014.
- [41] Samuel H. Maron and Percy E. Pierce. Application of ree-eyring generalized flow theory to suspensions of spherical particles. *J. Colloid Sci.*, 11(1):80–95, 1956.
- [42] G D Scott and D M Kilgour. The density of random close packing of spheres. *Journal of Physics D: Applied Physics*, 2(6):863, jun 1969. doi: 10.1088/0022-3727/2/6/311. URL <https://dx.doi.org/10.1088/0022-3727/2/6/311>.
- [43] Stany Gallier, Elisabeth Lemaire, François Peters, and Laurent Lobry. Rheology of sheared suspensions of rough frictional particles. *Journal of Fluid Mechanics*, 757:514–549, 2014. doi: 10.1017/jfm.2014.507.
- [44] Étienne Couturier, François Boyer, Olivier Pouliquen, and Elisabeth Guazzelli. Suspensions in a tilted trough: second normal stress difference. *Journal of Fluid Mechanics*, 686:26–39, 2011. doi: 10.1017/jfm.2011.315.
- [45] Shao-Cong Dai, Erwan Bertevas, Fuzhong Qi, and Roger I. Tanner. Viscometric functions for noncolloidal sphere suspensions with Newtonian ma-

- trices. *Journal of Rheology*, 57(2):493–510, 03 2013. ISSN 0148-6055. doi: 10.1122/1.4774325. URL <https://doi.org/10.1122/1.4774325>.
- [46] Colin D. Cwalina and Norman J. Wagner. Material properties of the shear-thickened state in concentrated near hard-sphere colloidal dispersions. *Journal of Rheology*, 58(4):949–967, 07 2014. ISSN 0148-6055. doi: 10.1122/1.4876935. URL <https://doi.org/10.1122/1.4876935>.
- [47] Dariel Hernández-Delfin, Ander García, and Marco Ellero. Rheology of a crowd: from faster-is-slower to shear thickening. *Communications Physics*, 7(1):152, May 2024. ISSN 2399-3650. doi: 10.1038/s42005-024-01646-1. URL <https://doi.org/10.1038/s42005-024-01646-1>.
- [48] Abdoulaye Fall, François Bertrand, Guillaume Ovarlez, and Daniel Bonn. Shear thickening of cornstarch suspensions. *Journal of Rheology*, 56(3):575–591, 05 2012. ISSN 0148-6055. doi: 10.1122/1.3696875. URL <https://doi.org/10.1122/1.3696875>.
- [49] Eric Brown and Heinrich M Jaeger. Shear thickening in concentrated suspensions: phenomenology, mechanisms and relations to jamming. *Rep. Prog. Phys.*, 77(4):046602, 2014.
- [50] Norman J. Wagner and John F. Brady. Shear thickening in colloidal dispersions. *Physics Today*, 62(10):27–32, 10 2009. ISSN 0031-9228. doi: 10.1063/1.3248476. URL <https://doi.org/10.1063/1.3248476>.
- [51] M. Wyart and M. E. Cates. Discontinuous shear thickening without inertia in dense non-brownian suspensions. *Phys. Rev. Lett.*, 112:098302, 2014.
- [52] Ryohei Seto, Romain Mari, Jeffrey F. Morris, and Morton M. Denn. Discontinuous shear thickening of frictional hard-sphere suspensions. *Phys. Rev. Lett.*, 111:218301, 2013.

- [53] Omer Sedes, Hernan A. Makse, Bulbul Chakraborty, and Jeffrey F. Morris.  $k$ -core analysis of shear-thickening suspensions. *Phys. Rev. Fluids*, 7:024304, 2022.
- [54] Romain Mari, Ryohei Seto, Jeffrey F. Morris, and Morton M. Denn. Shear thickening, frictionless and frictional rheologies in non-Brownian suspensions. *Journal of Rheology*, 58(6):1693–1724, 11 2014. ISSN 0148-6055. doi: 10.1122/1.4890747. URL <https://doi.org/10.1122/1.4890747>.
- [55] F. Gadala-Maria and Andreas Acrivos. Shear-Induced Structure in a Concentrated Suspension of Solid Spheres. *Journal of Rheology*, 24(6):799–814, 12 1980. ISSN 0148-6055. doi: 10.1122/1.549584. URL <https://doi.org/10.1122/1.549584>.
- [56] J. J. J. Gillissen, C. Ness, J. D. Peterson, H. J. Wilson, and M. E. Cates. Constitutive model for time-dependent flows of shear-thickening suspensions. *Phys. Rev. Lett.*, 123:214504, 2019.
- [57] Baptiste Darbois Texier, Henri Lhuissier, Bloen Metzger, and Yoël Forterre. Shear-thickening suspensions down inclines: from kapitza to oobleck waves. *J. Fluid Mech.*, 959:A27, 2023.
- [58] Rahul Chacko, Romain Mari, Michael Cates, and Suzanne Fielding. Dynamic vorticity banding in discontinuously shear thickening suspensions. *Phys. Rev. Lett.*, 121, 2018.
- [59] Osborne Reynolds. Lvii. on the dilatancy of media composed of rigid particles in contact. with experimental illustrations. *The London, Edinburgh, and Dublin Philosophical Magazine and Journal of Science*, 20(127):469–481, 1885. doi: 10.1080/14786448508627791. URL <https://doi.org/10.1080/14786448508627791>.
- [60] Alexis Bougouin, Bloen Metzger, Yoël Forterre, Pascal Boustingorry, and Henri Lhuissier. A frictional soliton controls the resistance law of shear-thickening

- suspensions in pipes. *Proceedings of the National Academy of Sciences*, 121(17):e2321581121, 2024. doi: 10.1073/pnas.2321581121. URL <https://www.pnas.org/doi/abs/10.1073/pnas.2321581121>.
- [61] P. L. Kapitza. Wave flow of thin layers of viscous liquid. Part I. Free flow. *Zhurnal Eksperimentalnoi i Teoreticheskoi Fiziki*, 18:3–18, February 1948.
- [62] T. Brooke Benjamin. Wave formation in laminar flow down an inclined plane. *Journal of Fluid Mechanics*, 2:554 – 573, 1957. URL <https://api.semanticscholar.org/CorpusID:123718628>.
- [63] D. J. Benney. Long waves on liquid films. *Journal of Mathematics and Physics*, 45(1-4):150–155, 1966. doi: <https://doi.org/10.1002/sapm1966451150>. URL <https://onlinelibrary.wiley.com/doi/abs/10.1002/sapm1966451150>.
- [64] Jun Liu and J. P. Gollub. Solitary wave dynamics of film flows. *Physics of Fluids*, 6(5):1702–1712, 05 1994. ISSN 1070-6631. doi: 10.1063/1.868232. URL <https://doi.org/10.1063/1.868232>.
- [65] Jun Liu, J. B. Schneider, and J. P. Gollub. Three-dimensional instabilities of film flows. *Physics of Fluids*, 7(1):55–67, 01 1995. ISSN 1070-6631. doi: 10.1063/1.868782. URL <https://doi.org/10.1063/1.868782>.
- [66] R. Usha and B. Uma. Modeling of stationary waves on a thin viscous film down an inclined plane at high Reynolds numbers and moderate Weber numbers using energy integral method. *Physics of Fluids*, 16(7):2679–2696, 07 2004. ISSN 1070-6631. doi: 10.1063/1.1755704. URL <https://doi.org/10.1063/1.1755704>.
- [67] R. A. Gingold and J. J. Monaghan. Smoothed particle hydrodynamics: theory and application to non-spherical stars. *Mon. Notices Royal Astron. Soc.*, 181(3):375–389, 1977.
- [68] J. J. Monaghan. Smoothed particle hydrodynamics. *Rep. Prog. Phys.*, 68(8):1703, 2005.

- [69] Steven J. Lind, Benedict D. Rogers, and Peter K. Stansby. Review of smoothed particle hydrodynamics: towards converged lagrangian flow modelling. *Proc. R. Soc. Lond. A*, 476(2241):20190801, 2020.
- [70] Javier Bonet and Tmh Lok. Variational and momentum preservation aspects of smooth particle hydrodynamic formulations. *Computer Methods in Applied Mechanics and Engineering*, 180:97–115, 1999. URL <https://api.semanticscholar.org/CorpusID:120725483>.
- [71] M. B. Liu and G. R. Liu. Smoothed particle hydrodynamics (sph): an overview and recent developments. *Archives of Computational Methods in Engineering*, 17(1):25–76, Mar 2010. ISSN 1886-1784. doi: 10.1007/s11831-010-9040-7. URL <https://doi.org/10.1007/s11831-010-9040-7>.
- [72] Joseph P. Morris, Patrick J. Fox, and Yi Zhu. Modeling low reynolds number incompressible flows using sph. *Journal of Computational Physics*, 136(1): 214–226, 1997.
- [73] Andrea Colagrossi and Maurizio Landrini. Numerical simulation of interfacial flows by smoothed particle hydrodynamics. *J. Comput. Phys.*, 191(2):448–475, November 2003. ISSN 0021-9991. doi: 10.1016/S0021-9991(03)00324-3. URL [https://doi.org/10.1016/S0021-9991\(03\)00324-3](https://doi.org/10.1016/S0021-9991(03)00324-3).
- [74] R.L. Borrelli and C.S. Coleman. *Differential Equations: A Modeling Approach*. Modeling Approach. Prentice-Hall, 1987. ISBN 9780132115339. URL <https://books.google.co.uk/books?id=f2sPAQAAMAJ>.
- [75] Ivar Bendixson. Sur les courbes définies par des équations différentielles, November 2018. URL <https://doi.org/10.1007/bf02403068>.
- [76] James Richards, John Royer, B. Liebchen, Ben Guy, and Wilson Poon. Competing timescales lead to oscillations in shear-thickening suspensions. *Phys. Rev. Lett.*, 123, 2019.

- [77] J. Mewis and N.J. Wagner. *Colloidal Suspension Rheology*. Cambridge Series in Chemical Engineering. Cambridge University Press, 2011. ISBN 9781107376137.
- [78] Roger I. Tanner. Review Article: Aspects of non-colloidal suspension rheology. *Phys. Fluids*, 30(10):101301, 2018.
- [79] Roger I. Tanner. *Engineering Rheology*. Oxford Engineering Science Series. OUP Oxford, 2000. ISBN 9780191590160.
- [80] Jeffrey F. Morris. Shear thickening of concentrated suspensions: Recent developments and relation to other phenomena. *Annu. Rev. Fluid Mech.*, 52(1): 121–144, 2020.
- [81] Ryohei Seto, Romain Mari, Jeffrey F. Morris, and Morton M. Denn. Discontinuous shear thickening of frictional hard-sphere suspensions. *Phys. Rev. Lett.*, 111:218301, 2013.
- [82] Jetin E. Thomas, Abhay Goyal, Deshpreet Singh Bedi, Abhinendra Singh, Emanuela Del Gado, and Bulbul Chakraborty. Investigating the nature of discontinuous shear thickening: Beyond a mean-field description. *J. Rheol.*, 64 (2):329–341, 2020.
- [83] Ryohei Seto, Abhinendra Singh, Bulbul Chakraborty, Morton Denn, and Jeffrey Morris. Shear jamming and fragility in dense suspensions. *Granul. Matter*, 21, 2019.
- [84] Marcio Gameiro, Abhinendra Singh, Lou Kondic, Konstantin Mischaikow, and Jeffrey F. Morris. Interaction network analysis in shear thickening suspensions. *Phys. Rev. Fluids*, 5:034307, 2020.
- [85] Mohammad Nabizadeh, Abhinendra Singh, and Safa Jamali. Structure and dynamics of force clusters and networks in shear thickening suspensions. *Phys. Rev. Lett.*, 129:068001, 2022.



- [86] Vishweshwara Herle, Peter Fischer, and Erich J. Windhab. Stress driven shear bands and the effect of confinement on their structuresa rheological, flow visualization, and rheo-sals study. *Langmuir*, 21(20):9051–9057, 2005.
- [87] Baptiste Darbois Texier, Henri Lhuissier, Yoël Forterre, and Bloen Metzger. Surface-wave instability without inertia in shear- thickening suspensions. *Commun. Phys.*, 3:1234567890, 2020.
- [88] Jae Hyung Cho, Andrew H. Griese, Ivo R. Peters, and Irmgard Bischofberger. Lasting effects of discontinuous shear thickening in cornstarch suspensions upon flow cessation. *Phys. Rev. Fluids*, 7:063302, 2022.
- [89] Vikram Rathee, Daniel L. Blair, and Jeffrey S. Urbach. Dynamics and memory of boundary stresses in discontinuous shear thickening suspensions during oscillatory shear. *Soft Matter*, 17:1337–1345, 2021.
- [90] Vikram Rathee, Daniel L. Blair, and Jeffrey S. Urbach. Localized transient jamming in discontinuous shear thickening. *J. Rheol.*, 64(2):299–308, 2020.
- [91] Vikram Rathee, Joia Miller, Daniel L. Blair, and Jeffrey S. Urbach. Structure of propagating high-stress fronts in a shear-thickening suspension. *Proc. Natl. Acad. Sci. USA*, 119(32):e2203795119, 2022.
- [92] Hiizu Nakanishi, Shin-ichiro Nagahiro, and Namiko Mitarai. Fluid dynamics of dilatant fluids. *Phys. Rev. E*, 85:011401, 2012.
- [93] Marco Ellero, Mar Serrano, and Pep Español. Incompressible smoothed particle hydrodynamics. *J. Comput. Phys.*, 226(2):1731–1752, 2007.
- [94] L. B. Lucy. A numerical approach to the testing of the fission hypothesis. *Astron. J.*, 82:1013–1024, 1977.
- [95] Ahmed M. Abdelrazek, Ichiro Kimura, and Yasuyuki Shimizu. Simulation of three-dimensional rapid free-surface granular flow past different types of obstructions using the SPH method. *J. Glaciol.*, 62(232):335–347, 2016.

- [96] Georgina Reece, Benedict D. Rogers, Steven Lind, and Georgios Fourtakas. New instability and mixing simulations using SPH and a novel mixing measure. *J. Hydrodynam.*, 32(4):684–698, 2020.
- [97] Farhoud Kalateh and Ali Koosheh. Simulation of cavitating fluid–structure interaction using SPH–FE method. *Math. Comput. Simul.*, 173:51–70, 2020. ISSN 0378-4754.
- [98] Nicolas Moreno and Marco Ellero. Generalized lagrangian heterogeneous multiscale modelling of complex fluids. *J. Fluid Mech.*, 969:A2, 2023.
- [99] Nicolas Moreno, Suzana Nunes, and Victor Calo. Morphological transitions of block copolymer micelles: implications for isoporous membrane ordering. 2023.
- [100] Luca Santelli, Adolfo Vázquez-Quesada, and Marco Ellero. SPH simulations of integral multimode and fractional viscoelastic models. *J. Non. Newt. Fluid Mech.*, 2023 (Under Review).
- [101] Marco Ellero, Martin Kröger, and Siegfried Hess. Viscoelastic flows studied by smoothed particle dynamics. *J. Non-Newtonian Fluid Mech.*, 105(1):35–51, 2002. ISSN 0377-0257.
- [102] Marco Ellero and Roger I. Tanner. SPH simulations of transient viscoelastic flows at low reynolds number. *J. Non-Newtonian Fluid Mech.*, 132(1):61–72, 2005. ISSN 0377-0257.
- [103] Jiannong Fang, Robert G. Owens, Laurent Tacher, and Aurèle Parriaux. A numerical study of the SPH method for simulating transient viscoelastic free surface flows. *J. Non-Newtonian Fluid Mech.*, 139:68–84, 2006.
- [104] Jiannong Fang, Aurèle Parriaux, Martin Rentschler, and Christophe Ancey. Improved sph methods for simulating free surface flows of viscous fluids. *Appl. Numer. Math.*, 59(2):251–271, 2009.

- [105] A. Rafiee, M. T. Manzari, and M. Hosseini. An incompressible sph method for simulation of unsteady viscoelastic free-surface flows. *Int. J. Non Linear Mech.*, 42(10):1210–1223, 2007. ISSN 0020-7462.
- [106] Xiaoyang Xu, Jie Ouyang, Bin-Xin Yang, and Zhijun Liu. SPH simulations of three-dimensional non-newtonian free surface flows. *Comput. Methods Appl. Mech. Eng.*, 256:101–116, 2013.
- [107] A. Vázquez-Quesada and M. Ellero. SPH simulations of a viscoelastic flow around a periodic array of cylinders confined in a channel. *J. Non-Newtonian Fluid Mech.*, 167-168:1–8, 2012. ISSN 0377-0257.
- [108] Muzio Grilli, Adolfo Vázquez-Quesada, and Marco Ellero. Transition to turbulence and mixing in a viscoelastic fluid flowing inside a channel with a periodic array of cylindrical obstacles. *Phys. Rev. Lett.*, 110:174501, 2013.
- [109] Xiaoyang Xu and Xiao-Long Deng. An improved weakly compressible SPH method for simulating free surface flows of viscous and viscoelastic fluids. *Computer Physics Communications*, 201:43–62, 2016. ISSN 0010-4655.
- [110] M. X. Rodriguez-Paz and J. Bonet. A corrected smooth particle hydrodynamics method for the simulation of debris flows. *Numer. Methods Partial Differ. Equ.*, 20(1):140–163, 2004.
- [111] Lorenzo Minatti and Enio Paris. A SPH model for the simulation of free surface granular flows in a dense regime. *Appl. Math. Model.*, 39(1):363–382, 2015.
- [112] O. Pouliquen, C. Cassar, P. Jop, Y. Forterre, and M. Nicolas. Flow of dense granular material: towards simple constitutive laws. *J. Stat. Mech.*, 2006(07):P07020, 2006.
- [113] Pierre Jop, Yoël Forterre, and Olivier Pouliquen. A constitutive law for dense granular flows. *Nature*, 441(7094):727–730, 2006.

- [114] G. Fourtakas and B.D. Rogers. Modelling multi-phase liquid-sediment scour and resuspension induced by rapid flows using smoothed particle hydrodynamics (SPH) accelerated with a graphics processing unit (GPU). *Adv. Water Resour.*, 92:186–199, 2016.
- [115] M. Khanpour, A.R. Zarrati, M. Kolahdoozan, A. Shakibaeinia, and S.M. Amirshahi. Mesh-free SPH modeling of sediment scouring and flushing. *Computers & Fluids*, 129:67–78, 2016.
- [116] Huaning Zhu, Nicos S. Martys, Chiara Ferraris, and Daniel De Kee. A numerical study of the flow of bingham-like fluids in two-dimensional vane and cylinder rheometers using a smoothed particle hydrodynamics (SPH) based method. *J. Non-Newtonian Fluid Mech.*, 165(7):362–375, 2010.
- [117] Afonso Paiva, Fabiano Petronetto, Thomas Lewiner, and Geovan Tavares. Particle-based viscoplastic fluid/solid simulation. *Computer-Aided Design*, 41(4):306–314, 2009.
- [118] Chongqiang Zhu, Yu Huang, and Liang-tong Zhan. SPH-based simulation of flow process of a landslide at hongao landfill in china. *Natural Hazards*, 93(3):1113–1126, 2018.
- [119] E. Rossi, I. Garcia de Beristain, A. Vazquez-Quesada, J.E. López-Aguilar, and M. Ellero. SPH simulations of thixo-viscoplastic fluid flow past a cylinder. *J. Non-Newtonian Fluid Mech.*, 308:104891, 2022. ISSN 0377-0257.
- [120] A. Vázquez-Quesada, N. J. Wagner, and M. Ellero. Planar channel flow of a discontinuous shear-thickening model fluid: Theory and simulation. *Phys. Fluids*, 29(10):103104, 2017.
- [121] Marcio Gameiro, Abhinendra Singh, Lou Kondic, Konstantin Mischaikow, and Jeffrey F. Morris. Interaction network analysis in shear thickening suspensions. *Phys. Rev. Fluids*, 5:034307, 2020.

- [122] Georges Bossis, Pascal Boustingorry, Yan Grasselli, Alain Meunier, Romain Morini, Audrey Zubarev, and Olga Volkova. Discontinuous shear thickening in the presence of polymers adsorbed on the surface of calcium carbonate particles. *Rheol. Acta*, 56(5):415–430, 2017.
- [123] Ken Kamrin and David L. Henann. Nonlocal modeling of granular flows down inclines. *Soft Matter*, 11:179–185, 2015.
- [124] S. Adami, X. Y. Hu, and N. A. Adams. A generalized wall boundary condition for smoothed particle hydrodynamics. *J. Comput. Phys.*, 231(21):7057–7075, 2012. ISSN 0021-9991.
- [125] R. Courant, K. Friedrichs, and H. Lewy. Über die partiellen differenzengleichungen der mathematischen physik. *Mathematische Annalen*, 100(1):32–74, 1928.
- [126] S. J. Lind, R. Xu, P.K. Stansby, and B. D. Rogers. Incompressible smoothed particle hydrodynamics for free-surface flows: A generalised diffusion-based algorithm for stability and validations for impulsive flows and propagating waves. *J. Comput. Phys.*, 231(4):1499–1523, 2012. ISSN 0021-9991.
- [127] Adolfo Vázquez-Quesada, Pep Español, Roger I. Tanner, and Marco Ellero. Shear thickening of a non-colloidal suspension with a viscoelastic matrix. *J. Fluid Mech.*, 880:1070–1094, 2019.
- [128] Ivo R Peters, Sayantan Majumdar, and Heinrich M Jaeger. Direct observation of dynamic shear jamming in dense suspensions. *Nature*, 532(7598):214–217, 2016. ISSN 0028-0836.
- [129] Deren Ozturk, Miles L. Morgan, and Bjørnar Sandnes. Flow-to-fracture transition and pattern formation in a discontinuous shear thickening fluid. *Commun. Phys.*, 3:1–9, 2020.

- [130] Jean Comtet, Guillaume Chatté, Antoine Niguès, Lydéric Bocquet, Alessandro Siria, and Annie Colin. Pairwise frictional profile between particles determines discontinuous shear thickening transition in non-colloidal suspensions. *Nature Communications*, 8(1):15633, May 2017. ISSN 2041-1723. doi: 10.1038/ncomms15633. URL <https://doi.org/10.1038/ncomms15633>.
- [131] Omer Sedes, Abhinendra Singh, and Jeffrey F. Morris. Fluctuations at the onset of discontinuous shear thickening in a suspension. *Journal of Rheology*, 64(2):309–319, 03 2020. ISSN 0148-6055. doi: 10.1122/1.5131740. URL <https://doi.org/10.1122/1.5131740>.
- [132] Peter D. Olmsted. Perspectives on shear banding in complex fluids. *Rheologica Acta*, 47(3):283–300, Apr 2008. ISSN 1435-1528. doi: 10.1007/s00397-008-0260-9. URL <https://doi.org/10.1007/s00397-008-0260-9>.
- [133] Shin-ichiro Nagahiro and Hiizu Nakanishi. Negative pressure in shear thickening band of a dilatant fluid. *Phys. Rev. E*, 94:062614, Dec 2016. doi: 10.1103/PhysRevE.94.062614. URL <https://link.aps.org/doi/10.1103/PhysRevE.94.062614>.
- [134] Brice Saint-Michel, Thomas Gibaud, and Sébastien Manneville. Uncovering instabilities in the spatiotemporal dynamics of a shear-thickening cornstarch suspension. *Phys. Rev. X*, 8:031006, Jul 2018. doi: 10.1103/PhysRevX.8.031006. URL <https://link.aps.org/doi/10.1103/PhysRevX.8.031006>.
- [135] Vikram Rathee, Daniel L. Blair, and Jeffrey S. Urbach. Localized stress fluctuations drive shear thickening in dense suspensions. *Proceedings of the National Academy of Sciences*, 114(33):8740–8745, 2017. doi: 10.1073/pnas.1703871114. URL <https://www.pnas.org/doi/abs/10.1073/pnas.1703871114>.
- [136] Peter Angerman, Sagaya S. Prasanna Kumar, Ryohei Seto, Bjornar Sandnes, and Marco Ellero. Microstructural smoothed particle hydrodynamics model and simulations of discontinuous shear-thickening fluids. *Physics of Fluids*, 36

- (3):033103, 03 2024. ISSN 1070-6631. doi: 10.1063/5.0188444. URL <https://doi.org/10.1063/5.0188444>.
- [137] J. J. J. Gillissen, C. Ness, J. D. Peterson, H. J. Wilson, and M. E. Cates. Constitutive model for time-dependent flows of shear-thickening suspensions. *Phys. Rev. Lett.*, 123:214504, Nov 2019. doi: 10.1103/PhysRevLett.123.214504. URL <https://link.aps.org/doi/10.1103/PhysRevLett.123.214504>.
- [138] Endao Han, Matthieu Wyart, Ivo R. Peters, and Heinrich M. Jaeger. Shear fronts in shear-thickening suspensions. *Phys. Rev. Fluids*, 3:073301, Jul 2018. doi: 10.1103/PhysRevFluids.3.073301. URL <https://link.aps.org/doi/10.1103/PhysRevFluids.3.073301>.
- [139] Haitao Hu, Yiqiu Zhao, Weiwei Zhao, Ligen Qiao, and Qin Xu. Non-monotonic rheology and stress heterogeneity in confined granular suspensions, 2024. URL <https://arxiv.org/abs/2211.12272>.
- [140] Eric Brown and Heinrich M. Jaeger. Dynamic jamming point for shear thickening suspensions. *Phys. Rev. Lett.*, 103:086001, Aug 2009. doi: 10.1103/PhysRevLett.103.086001. URL <https://link.aps.org/doi/10.1103/PhysRevLett.103.086001>.
- [141] J.F. Richardson and W.N. Zaki. The sedimentation of a suspension of uniform spheres under conditions of viscous flow. *Chemical Engineering Science*, 3(2): 65–73, 1954. ISSN 0009-2509. doi: [https://doi.org/10.1016/0009-2509\(54\)85015-9](https://doi.org/10.1016/0009-2509(54)85015-9). URL <https://www.sciencedirect.com/science/article/pii/0009250954850159>.
- [142] Koichi Takamura, Herbert Fischer, and Norman R. Morrow. Physical properties of aqueous glycerol solutions. *Journal of Petroleum Science and Engineering*, 98-99:50–60, 2012. ISSN 0920-4105. doi: <https://doi.org/10.1016/j.petrol.2012.09.003>. URL <https://www.sciencedirect.com/science/article/pii/S0920410512002185>.

- [143] Endao Han, Nigel Van Ha, and Heinrich M. Jaeger. Measuring the porosity and compressibility of liquid-suspended porous particles using ultrasound. *Soft Matter*, 13:3506–3513, 2017. doi: 10.1039/C7SM00182G. URL <http://dx.doi.org/10.1039/C7SM00182G>.
- [144] Richard Lucas. Ueber das zeitgesetz des kapillaren aufstiegs von flüssigkeiten. *Kolloid-Zeitschrift*, 23(1):15–22, Jul 1918. ISSN 1435-1536. doi: 10.1007/BF01461107. URL <https://doi.org/10.1007/BF01461107>.
- [145] Chia shun Yih. Stability of liquid flow down an inclined plane. *Physics of Fluids*, 6:321–334, 1963. URL <https://api.semanticscholar.org/CorpusID:121765503>.
- [146] P. L. Kapitza and S. P. Kapitza. Wave flow of thin layers of viscous liquids. Part III. Experimental research of a wave flow regime. *Zhurnal Eksperimentalnoi i Teoreticheskoi Fiziki*, 19:105–120, December 1949.
- [147] Zhongqiang () Xiong, Peter Angerman, Marco Ellero, Bjornar Sandnes, and Ryohei () Seto. Ridge instability in dense suspensions caused by the second normal stress difference. *Physics of Fluids*, 36(2):024111, 02 2024. ISSN 1070-6631. doi: 10.1063/5.0188004. URL <https://doi.org/10.1063/5.0188004>.
- [148] M. Keentok, A.G. Georgescu, A.A. Sherwood, and R.I. Tanner. The measurement of the second normal stress difference for some polymer solutions. *Journal of Non-Newtonian Fluid Mechanics*, 6(3):303–324, 1980. ISSN 0377-0257. doi: [https://doi.org/10.1016/0377-0257\(80\)80008-5](https://doi.org/10.1016/0377-0257(80)80008-5). URL <https://www.sciencedirect.com/science/article/pii/0377025780800085>.
- [149] Y. Kuo and R.I. Tanner. Laminar newtonian flow in open channels with surface tension. *International Journal of Mechanical Sciences*, 14(12):861–873, 1972. ISSN 0020-7403. doi: [https://doi.org/10.1016/0020-7403\(72\)90045-8](https://doi.org/10.1016/0020-7403(72)90045-8). URL <https://www.sciencedirect.com/science/article/pii/0020740372900458>.



- [150] Y. Kuo and R. I. Tanner. On the use of open-channel flows to measure the second normal stress difference. *Rheologica Acta*, 13(3):443–456, Jun 1974. ISSN 1435-1528. doi: 10.1007/BF01521740. URL <https://doi.org/10.1007/BF01521740>.